

---

Theses and Dissertations

---

Spring 2010

# Mechanical and optical methods for breast cancer imaging

Zhiguo Wang  
*University of Iowa*

Copyright 2010 Zhiguo Wang

This dissertation is available at Iowa Research Online: <http://ir.uiowa.edu/etd/618>

---

## Recommended Citation

Wang, Zhiguo. "Mechanical and optical methods for breast cancer imaging." PhD (Doctor of Philosophy) thesis, University of Iowa, 2010.  
<http://ir.uiowa.edu/etd/618>.

---

Follow this and additional works at: <http://ir.uiowa.edu/etd>



Part of the [Civil and Environmental Engineering Commons](#)

MECHANICAL AND OPTICAL METHODS FOR BREAST CANCER IMAGING

by  
Zhiguo Wang

An Abstract

Of a thesis submitted in partial fulfillment  
of the requirements for the Doctor of  
Philosophy degree in Civil and Environmental Engineering  
in the Graduate College of  
The University of Iowa

May 2010

Thesis Supervisors: Adjunct Associate Professor Lizhi Sun  
Professor Ge Wang

## ABSTRACT

It has been recognized that mechanical and optical properties of tissues can be the indicators to identify and characterize breast tumors. The objective of this study is to develop new mechanical and optical modalities for qualification of the elastic and optical properties of normal and cancerous breast tissues.

First, a mammography-based elastography (called elasto-mammography) is proposed to generate the elastogram of breast tissues based on conventional X-ray mammography. The displacement information is extracted from mammography projections before and after breast compression. With the incorporation of the displacement measurements, an elastography reconstruction algorithm is specially developed to estimate the elastic moduli of heterogeneous breast tissues. Case studies with numerical breast phantoms are conducted to demonstrate the capability of the proposed elasto-mammography. It is shown that the proposed methodology is stable and robust for characterization of the elastic moduli of breast tissues from the projective displacement measurement.

Second, a nonlinear elastography is proposed to extend breast material model to nonlinear cases. A three-dimensional (3D) model is developed for heterogeneous breast tissues extracting from real images including fatty tissue, glandular tissue, and tumors. An exponential-form of nonlinear material model is applied. Based on the finite-deformation constitutive law, discretized nonlinear equations are solved for displacement, strain, and stress fields in breast tissues with given tumors under external compression at breast boundaries. We develop a 3D inverse-problem algorithm to reconstruct the material parameters for nonlinear elastic constitutive relation of breast phantoms with tumors. For the first time, a nonlinear adjoint gradient method is introduced to improve the numerical efficiency and enhance the stability of elastography reconstruction.

Third, encouraged by the success of linear elasto-mammography and nonlinear elastography, a nonlinear elasto-mammography method is proposed. Mammography projections are taken before and after breast compression and displacement information is extracted for reconstruction of nonlinear breast tissue properties. Numerical phantom study is conducted and results show the proposed nonlinear elasto-mammography is potential to identify and characterize breast tumors in clinic.

Finally, we switch from mechanical to optical method for breast cancer imaging. We develop a finite-element-based algorithm to solve the inverse problem of frequent-domain diffusion equation. With the analytical form of gradients, the adjoint method is expanded to complex domain for the reconstruction of optical parameters in diffuse optical tomography. Specific numerical simulation is carried out and compared with phantom experiment. The results show that the adjoint-based algorithm is efficient and robust for reconstructing the optical parameters.

Abstract Approved: \_\_\_\_\_  
 Thesis Supervisor

\_\_\_\_\_

Title and Department

\_\_\_\_\_

Date

\_\_\_\_\_

Thesis Supervisor

\_\_\_\_\_

Title and Department

\_\_\_\_\_

Date

MECHANICAL AND OPTICAL METHODS FOR BREAST CANCER IMAGING

by  
Zhiguo Wang

A thesis submitted in partial fulfillment  
of the requirements for the Doctor of  
Philosophy degree in Civil and Environmental Engineering  
in the Graduate College of  
The University of Iowa

May 2010

Thesis Supervisors: Adjunct Associate Professor Lizhi Sun  
Professor Ge Wang

Copyright by  
ZHIGUO WANG  
2010  
All Rights Reserved

Graduate College  
The University of Iowa  
Iowa City, Iowa

CERTIFICATE OF APPROVAL

---

PH.D. THESIS

---

This is to certify that the Ph.D. thesis of

Zhiguo Wang

has been approved by the Examining Committee  
for the thesis requirement for the Doctor of Philosophy  
degree in Civil and Environmental Engineering at the May 2010 graduation.

Thesis Committee: \_\_\_\_\_  
Lizhi Sun, Thesis Supervisor

\_\_\_\_\_  
Ge Wang, Thesis Supervisor

\_\_\_\_\_  
Colby Swan

\_\_\_\_\_  
M. Asghar Bhatti

\_\_\_\_\_  
Shaoping Xiao

\_\_\_\_\_  
Laurie L. Fajardo

To My Parents



## ACKNOWLEDGMENTS

No man is an island, and I am no exception; there are a thousand people I need to thank for their help and support during this research.

First and foremost I would like to express my deepest gratitude to my supervisor, Professor Lizhi Sun, for his guidance, support and encouragement throughout my thesis. His support, knowledge, and experience were essential for the completion of this work. I appreciate his excellent advice and encouragement in academic and professional aspects. I can never thank him enough for his great help in my life.

I gratefully acknowledge my co-supervisor, Professor Ge Wang, for his advice, supervision, and crucial contribution, which made him a backbone of this research and so to this thesis. His involvement with his originality has triggered and nourished my intellectual maturity that I will benefit from, for a long time to come.

In my daily work I have been blessed to have Dr. Yi Liu in the group. I am much indebted to him for his valuable advice, supervision, using his precious times to review my work and give his critical comments. Without him this thesis would not have been completed.

Furthermore, I would also like to thank Professor Colby Swan, Professor M. Asghar Bhatti, Professor Shaoping Xiao and Professor Laurie L. Fajardo, for their willingness to review my research, offer valuable comments and serve on my thesis committee. I really appreciate it.

Words fail me to express my appreciation to my family for their patience, support and love throughout my life. My father is the person who put my learning character, showing the joy of intellectual pursuit ever since I was a child. My mother is the one who sincerely raised me with her caring and the gently love. They also taught me to dream and to work to make my dreams come true.

## ABSTRACT

It has been recognized that mechanical and optical properties of tissues can be the indicators to identify and characterize breast tumors. The objective of this study is to develop new mechanical and optical modalities for qualification of the elastic and optical properties of normal and cancerous breast tissues.

First, a mammography-based elastography (called elasto-mammography) is proposed to generate the elastogram of breast tissues based on conventional X-ray mammography. The displacement information is extracted from mammography projections before and after breast compression. With the incorporation of the displacement measurements, an elastography reconstruction algorithm is specially developed to estimate the elastic moduli of heterogeneous breast tissues. Case studies with numerical breast phantoms are conducted to demonstrate the capability of the proposed elasto-mammography. It is shown that the proposed methodology is stable and robust for characterization of the elastic moduli of breast tissues from the projective displacement measurement.

Second, a nonlinear elastography is proposed to extend breast material model to nonlinear cases. A three-dimensional (3D) model is developed for heterogeneous breast tissues extracting from real images including fatty tissue, glandular tissue, and tumors. An exponential-form of nonlinear material model is applied. Based on the finite-deformation constitutive law, discretized nonlinear equations are solved for displacement, strain, and stress fields in breast tissues with given tumors under external compression at breast boundaries. We develop a 3D inverse-problem algorithm to reconstruct the material parameters for nonlinear elastic constitutive relation of breast phantoms with tumors. For the first time, a nonlinear adjoint gradient method is introduced to improve the numerical efficiency and enhance the stability of elastography reconstruction.

Third, encouraged by the success of linear elasto-mammography and nonlinear elastography, a nonlinear elasto-mammography method is proposed. Mammography projections are taken before and after breast compression and displacement information is extracted for reconstruction of nonlinear breast tissue properties. Numerical phantom study is conducted and results show the proposed nonlinear elasto-mammography is potential to identify and characterize breast tumors in clinic.

Finally, we switch from mechanical to optical method for breast cancer imaging. We develop a finite-element-based algorithm to solve the inverse problem of frequent-domain diffusion equation. With the analytical form of gradients, the adjoint method is expanded to complex domain for the reconstruction of optical parameters in diffuse optical tomography. Specific numerical simulation is carried out and compared with phantom experiment. The results show that the adjoint-based algorithm is efficient and robust for reconstructing the optical parameters.

## TABLE OF CONTENTS

LIST OF TABLES .....	ix
LIST OF FIGURES .....	x
CHAPTER 1 INTRODUCTION.....	1
1.1 Background.....	1
1.2 Elastography .....	2
1.3 Diffuse Optical Tomography.....	6
1.4 Scope of the Thesis.....	9
CHAPTER 2 LITERATURE REVIEW.....	11
2.1 Breast Cancer.....	11
2.2 Mammography.....	12
2.3 Elastography .....	15
2.3.1 Introduction .....	15
2.3.2 Ultrasound Elastography (USE).....	16
2.3.3 Magnetic Resonance Elastography (MRE).....	20
2.4 Diffuse Optical Tomography.....	30
2.4.1 Introduction .....	30
2.4.2 Models of Photon Transport in Tissue .....	33
2.4.3 Forward Problem.....	36
2.4.3.1 Analytical Modeling Techniques .....	36
2.4.3.2 Statistical Modeling Techniques .....	36
2.4.3.3 Numerical Modeling Techniques .....	37
2.4.4 Inverse Problem.....	38
2.4.4.1 Linear Image Reconstruction .....	38
2.4.4.2 Non-linear Image Reconstruction .....	39
2.4.5 Recent Advances in Diffuse Optical Imaging.....	41
2.4.5.1 Use of Prior Information .....	41
2.4.5.2 Effect of Pressure .....	42
CHAPTER 3 LINEAR ELASTO-MAMMOGRAPHY.....	46
3.1 Introduction.....	46
3.2 Methodology of Elastography Reconstruction .....	47
3.2.1 Governing Equations and Finite Element Method .....	47
3.2.2 Objective Function .....	48
3.2.3 Adjoint Method .....	49
3.2.4 Optimization-based Reconstruction Procedure .....	54
3.3 Numerical Simulations .....	54
3.3.1 Forward Computations .....	56
3.3.2 Data Acquisition.....	60
3.3.3 Inverse Problem.....	64
3.4 Discussion.....	67
3.4.1 Effect of Noise.....	67
3.4.2 Effect of Geometry Mismatch.....	69
3.4.3 Effect of Contrast Ratio.....	71
3.4.4 Uniqueness and Multiple Measurements.....	72

3.5 Conclusions.....	73
CHAPTER 4 NONLINEAR ELASTOGRAPHY.....	75
4.1 Introduction.....	75
4.2 Methodology of Nonlinear Elastography .....	76
4.2.1 Finite-Strain Deformation Equations .....	76
4.2.2 Objective Function .....	77
4.2.3 Nonlinear Adjoint Method .....	78
4.2.4 Optimization-based Reconstruction Procedure .....	80
4.3 Numerical Simulations .....	82
4.3.1 Breast Phantom.....	82
4.3.2 Forward Problem.....	87
4.3.3 Inverse Problem.....	92
4.4 Results and Discussion .....	93
4.4.1 Effect of Noise.....	93
4.4.2 Linear v.s. Nonlinear .....	96
4.4.3 Nonlinear Adjoit Method .....	98
4.4.4 Uniquenes and Multiple Measurements .....	100
4.5 Conclusions.....	100
CHAPTER 5 NONLINEAR ELASTO-MAMMOGRAPHY.....	102
5.1 Introduction.....	102
5.2 Methodology of Nonlinear Elastography .....	103
5.2.1 Finite-Strain Deformation Equations .....	103
5.2.2 Objective Function .....	104
5.2.3 Global projection Matrix .....	106
5.2.4 Nonlinear Adjoint Method .....	108
5.2.5 Optimization-based Reconstruction Procedure .....	111
5.3 Numerical Simulations .....	113
5.3.1 Breast Phantom and Forward Problem.....	113
5.3.2 Acquisition Projection Data. ....	113
5.3.3 Inverse Problem.....	119
5.4 Results and Discussion .....	119
5.4.1 Ideal Input.....	119
5.4.2 Multiple Sets of Measurements .....	123
5.4.3 Iteration Steps.....	124
5.4.4 Adjoint Method .....	126
5.4.5 Input with Noise .....	126
5.5 Conclusions.....	128
CHAPTER 6 DIFFUSE OPTICAL TOMOGRAPHY.....	129
6.1 Introduction.....	129
6.2 Methodology.....	130
6.2.1 Diffuse Eqaution.....	130
6.2.2 Objective Function .....	133
6.2.3 Adjoint Method .....	134
6.2.4 Optimization-based Reconstruction Procedure .....	136
6.3 Experiment.....	137
6.4 Numerical Simulation.....	138
6.4.1 Finite Element Model .....	138
6.4.2 Inverse Problem.....	140

6.5 Discussion.....	142
6.5.1 Regularization.....	142
6.5.2 Prior Knowledge.....	145
6.5.3 Adjoint Method in Complex Domain.....	146
6.5.4 Frequent Domain and Wavelength.....	148
6.6 Conclusions.....	149
CHAPTER 7 CONCLUSIONS AND RECOMMENDATIONS.....	150
7.1 Conclusions.....	150
7.1.1 Elasto-mammography.....	150
7.1.2 Diffuse Optical Tomography.....	152
7.2 Recommendations for Future Work .....	153
7.2.1 Multi-modalities .....	153
7.2.2 Effect of Pressure .....	154
REFERENCES.....	155

## LIST OF TABLES

Table 1-1	Comparison among the three types of elastographic imaging modalities .....	4
Table 2-1	Average elastic modulus and the standard deviation of the modulus for each of eight different types of breast tissues tested .....	17
Table 2-2	The ratio of elastic modulus of each tissue to fat at 4 different strain levels .....	18
Table 2-3	Different malignant and benign breast tumors and their potential optically detectable features.....	32
Table 3-1	Estimate of leading-order computational costs per iteration for various iterative method, where $N$ is the number of unknown material parameters .....	53
Table 3-2	Initial estimate and reconstructed results for linear elasto-mammography .....	65
Table 3-3	Elasto-mammography simulation using phantoms with different stiffness contract ratios .....	72
Table 4-1	Initial estimate and reconstructed results for nonlinear elastogrphahy.....	93
Table 5-1	Initial estimate and reconstructed results for nonlinear elasto-mammography. ....	121
Table 6-1	Real and reconstructed optical parameters .....	141

## LIST OF FIGURES

Figure 2-1	Normal and tumor cells.....	11
Figure 2-2	Results of a 20-year follow-up of 2468 breast cancer cases from the Swedish Two-County .....	13
Figure 2-3	A typical mammography imaging, a tumor could be seen easily .....	14
Figure 2-4	The sonogram (a) and elastogram (b) of an invasive ductal carcinoma in vivo at 5 MHz.....	19
Figure 2-5	The image of displacement and reconstructed elastogram for an object with diameter comparable to wavelength .....	22
Figure 2-6	MR elastogram of the breast of a patient with a 4 cm diameter, biopsy-proven breast cancer .....	23
Figure 2-7	Flow chart of the iterative method for reconstructing elastic modulus .....	26
Figure 2-8	Finite element model of the breast.....	27
Figure 2-9	Modulus reconstruction results.....	28
Figure 2-10	The absorption spectra of oxy- and deoxy-haemoglobin in the near infrared wavelength range.....	31
Figure 2-11	Photons travel in tissue .....	34
Figure 2-12	Diffuse light transports .....	35
Figure 2-13	Schematic flow of iterative nonlinear reconstruction procedure .....	40
Figure 2-14	Use of prior information. ....	44
Figure 2-15	Typical absorption coefficient (a) and scattering coefficient (b) changes with applied pressure from a human subject and elastic phantom.....	45
Figure 3-1	Overall flowchart for elasto-mammography reconstruction of Lamé parameters $\lambda$ and $\mu$ of breast tissues .....	55
Figure 3-2	Three-dimensional phantoms mimicking the normal breast tissue and embedded tumor(s) .....	57
Figure 3-3	Loading 1, compression nodal force applied on the surface.....	58
Figure 3-4	Loading 2, compression nodal force applied on the surface.....	59
Figure 3-5	Mammography projections with Phantom II under loading 1 .....	62
Figure 3-6	Mammography projections with Phantom II under loading 2 .....	63



Figure 3-7	Convergent loci of elasto-mammography reconstruction for Lamé parameters $(\lambda, \mu)$ of normal breast tissue and tumor, normalized with the exact values correspondingly .....	66
Figure 3-8	Convergent loci of elasto-mammography reconstruction for Lamé parameters $(\lambda, \mu)$ of normal breast tissue and tumor, normalized with real values correspondingly. Noise is considered .....	68
Figure 3-9	Geometry mismatch. ....	70
Figure 4-1	Overall flowchart for reconstruction of material parameters $\lambda, \mu$ and $\gamma$ of breast tissues in nonlinear elastography .....	81
Figure 4-2	A 3-D heterogeneous breast phantom extracted from real CT images, containing fatty tissue, glandular tissue and a tumor.....	84
Figure 4-3	FE model for nonlinear elastography.....	85
Figure 4-4	Nonlinear stress-strain curves for six breast tissues: fatty tissue, glandular tissue, lobular carcinoma, fibroadenoma, infiltrating ductal carcinoma, and ductal carcinoma in situ.....	86
Figure 4-5	Titled compression is given on breast surface by two paddles.....	88
Figure 4-6	Four types of compression loading by paddles.....	89
Figure 4-7	Comparison of paddle locations in four loadings .....	91
Figure 5-1	Illustration of global coordinate and eye coordinate.....	109
Figure 5-2	Overall flowchart for reconstruction of material parameters $\lambda, \mu$ and $\gamma$ of breast tissues in nonlinear elasto-mammography.....	112
Figure 5-3	Mammography projections for 3-D heterogeneous breast phantom before deformation.....	115
Figure 5-4	Mammography projections for 3-D heterogeneous breast phantom after deformation.....	116
Figure 5-5	Deformed projections overlaps on undeformed projection (only fatty tissue and the tumor are shown).....	117
Figure 5-6	Deformed projections overlaps on undeformed projection (only glandular tissue is shown).....	118
Figure 5-7	Convergent loci of nonlinear elasto-mammography reconstruction for elastic parameters $(\lambda, \mu, \gamma)$ of fatty tissue, glandular tissue and tumor, normalized with the exact values correspondingly .....	122
Figure 5-8	Nonlinear stress-strain curves for the tumor in different iteration steps. The lowest curve is for fatty tissue .....	125
Figure 5-9	Nonlinear stress-strain curves for the tumor with 5% and 10% noise. The lowest curve is for fatty tissue .....	127

Figure 6-1	Flow chart of diffuse optical tomography reconstruction of optical coefficients $\{\mu_a, \mu'_s\}$ in frequent domain.....	137
Figure 6-2	FE model with 3264 elements and 1761 nodes to simulate the phantom.....	139
Figure 6-3	Convergent curves of DOT reconstruction for optical parameters $\{\mu_a, \mu'_s\}$ of the matrix and inclusion.....	143

## CHAPTER 1 INTRODUCTION

### 1.1 Background

Breast cancer is one of major threats to public health in the world. Approximately 10% of women will develop breast cancer during the course of their lives in USA and Europe. In the USA, there are approximately 2.6 million people living with breast cancer (NIH-NCI, 2004). American Cancer Society estimated that there were 184,450 new breast cancer cases in US in 2008, and 194,280 in 2009, which is about 27% of all new cancer cases for women. And deaths of breast cancer were estimated 40,480 in 2008 and 40,170 in 2009, which is about 15% of all deaths of cancers (American Cancer Society, 2008, 2009). The specific causes of breast cancer are yet unknown. Therefore the early detection of the breast tumor is the key to successful treatment.

Currently, X-ray mammography is the primary method for early detection and characterization of breast tumors (Muller, 1999; Nass et al., 2001). Mammography is a specific type of imaging that uses a low-dose X-ray system for the examination of breasts. According to the reports of US Food and Drug Administration, mammography can find 85 to 90 percent of breast cancers in women over 50, and can detect a lump up to two years before it can be sensed by manual palpation.

While it is more effective in detecting tumors as age increases and the breast becomes fatty, mammography fails to detect small cancers (less than 8 mm) in dense breasts. On the other hand, mammography is not quite specific in terms of tumor benignity and malignancy. Approximate 80% of suspicious masses referred by mammography for surgical breast biopsy are in fact not malignant (Bone et al., 1997; Giger et al., 2000; Kornguth et al., 2001; Plewes et al., 2000). The number of unnecessary benign biopsies that are performed annually approaches 1 million. Using an average reimbursement for an open breast biopsy of \$2400 (Burkhardt and Sunshine, 1999), the financial cost of benign breast tumors to healthcare system is on the order of \$2 billion

annually (Thitaikumar et al., 2008). Meanwhile, these false-positive mammograms may create patients' anxiety, distress and intrusive thoughts.

A number of techniques are currently being explored to solve these problems associated with mammography. Elastography and optical tomography are two of them.

### 1.2 Elastography

It has been well recognized that tissue stiffness plays an important role for diagnosis of breast cancers, as tumors are stiffer than the surrounding breast tissues (Sarvazyan et al., 1995; Wellman et al., 1999), and malignant tumors are much stiffer than benign ones (Skovoroda, 1995).

Therefore elastic properties are good indicator of histological diagnosis, in other words, in vivo identification of elastic modulus of normal and abnormal tissues should improve the accuracy of cancer diagnosis.

Elastography is proposed as a method to imaging tissue elastic modulus in quantitative manner. The general basis of elastography is to induce motion within the tissue by mechanical stimulation. Conventional medical imaging modalities measure the spatial deformation in tissue, by which elastic properties distribution is reconstructed. Based on the imaging modalities used, two major kinds of elastography are ultrasound elastography (USE) and magnetic resonance elastography (MRE).

Developed in the 1990s by Ophir's group (Ophir et al., 1991 & 1999; Garra et al., 1997; Righetti et al., 2002) at University of Texas Medical School, USE is the first modulus-imaging modality. They computed the lap between the pre- and post-compression radio frequency ultrasound signals to estimate the axial tissue displacement and associated axial strain under quasi-static loading. If certain tissue regions have different stiffness than others, the level of strain in those regions will generally be higher or lower than those in the surrounding material. Recently a few researches were carried out to develop 3D ultrasound elastography (Lindop et al, 2006; Treece et al., 2008;

Richards et al., 2009). In contrast with quasi-static compression, other researchers (e.g., Alam et al., 1994; Gao et al., 1997; Fatemi et al., 1998 & 2002; Doyley et al. 2001; Hiltawsky et al., 2001) applied low-frequency vibration. Besides the numerical simulation, recent years some researchers have carried out clinical experiments based on ultrasound elastography (Barcoff et al., 2003; Regner et al., 2006; Barr, 2006; Itoh et al., 2006; Zhu et al., 2008)

While providing new information to detect pathological tumors, USE suffers from stiffness range limitations imposed by the minimum resolvable wavelength. In addition, the computed image is restricted by the angular resolution of the transducer and its ability to separate signals from artifacts and noise. Most of USE elastograms are referred to as the strain imaging which may not always provide useful information on locations and characterizations of the heterogeneous lesions. For example, the phenomenon called “butterfly wings” (Ophir et al., 1999) is frequently observed in USE strain elastograms, which can be misleading with respect to tumor detection.

Magnetic resonance elastography (MRE), the second-generation elastography modality, was developed by several research groups including Ehman and co-workers (Muthupillai et al., 1995; McKnight et al., 2002) at Mayo Clinic, Plewes et al. (2000 and 2002) and Samani et al. (2001, 2004, and 2007) at University of Toronto, Sinkus et al. (2000) in Germany, and Van Houten et al. (1999, 2001, and 2003) at Dartmouth College.

MRE provides higher resolution imaging and is capable of producing sufficient 3-D spatial and contrast resolution. MRE is, however, significantly more costly as a result of the MR imaging procedure, and hence is not generally applicable for all patients. Further, MRE tumor detection may encounter a penetration problem when applied to breast cancer diagnosis *in vivo*. The penetration depth of shear waves within organic tissue is limited to only a few centimeters. Due to a large frequency-dependent attenuation, only low-frequency waves of about 50-100 Hz are feasible. This limits the spatial resolution and the achievable detectability of small lesions.

Moreover, from a mathematical point of view, the current USE and MRE algorithm are all based on infinitesimal-strain linear elastic deformation theory, and only very few have considered anisotropic tissue properties. The large deformation, nonlinear and anisotropic behaviors of breast tissues (such as glandular tissue) and tumors have not yet been taken into consideration. Therefore, outcomes of USE and MRE are in fact not sufficiently accurate for diagnostic purpose.

Motivated by the important of detecting breast tumors and the current limitations of mammography and elastography modalities, we have developed the nonlinear elasto-mammography that utilizes the novel nonlinearly elastic breast model combined with mammography visualizations. The nonlinear elasto-mamography can quantitatively detect breast tumors in their early stage and provides high contrast resolution of modulus elastograms without additional cost. A comparison of US elastography (USE), MR elastography (MRE) and nonlinear elasto-mammography is given in Table 1-1.

Table 1-1 Comparison among three types of elastographic imaging modalities

	<b>USE</b>	<b>MRE</b>	<b>Elasto-mammography</b>
Modality Base	Ultrasound	MR Imaging	Mammography
Compression	Static/dynamics	Static/dynamic	Static
Deformation	Linear, small	Linear, small	Nonlinear, large
Elastograms	Strain	Modulus	Modulus
Tissue Anisotropy	Most isotropic	Most isotropic	Anisotropy
Resolution	Low	High	High
Cost	Medium	Expensive	Low

There are three steps to develop nonlinear elasto-mammography. First, we have developed a linear elasto-mammography method which generates the elastograms of breast tissue by combining the conventional low-dose X-ray mammography with elastography framework (Wang et al., 2006). Instead of using ultrasound and magnetic resonance like in previous elastography, the displacement information is extracted from mammography projections before and after breast compression. Incorporating the displacement measurement, an elastography reconstruction algorithm is specifically developed to estimate the elastic moduli of heterogeneous breast tissue. Case studies with numerical breast phantoms show that the displacement measurement obtained from mammography is sufficient to identify the material parameters of breast tissues and tumors. More details about this linear elasto-mammography are introduced in Chapter 3.

The second step is to develop elastography method for reconstruction of nonlinear breast tissue properties. As mentioned before, current elastography (USE and MRE) reconstruction framework is based on the assumption of linear elasticity theory. It is shown, however, that the deformation of most biological soft tissue is not linear elastic (Wellman, 1999; Khaled, 2007). Consideration of nonlinear model is essential for elastography in clinical application. So in this thesis, an elastography model for nonlinear breast tissue is developed and for the first time, a nonlinear adjoint gradient method is introduced. The nonlinear adjoint gradient method significantly improves the numerical efficiency and enhances the stability of elastography reconstructions. In fact, without this method, nonlinear biomedical elastography can only be discussed in concept (Pathmanathan et al., 2004 & 2007) or applied on simple objects using super computer power (Kauer, 2001). Oberai et al., (2003) adopted an adjoint method and proposed a numerical scheme for reconstructing the non-uniform shear modulus field for incompressible isotropic materials using one component of displacement field. Liu et al. (2005) applied this method for anisotropic materials. The advantage of adjoint method is to solve two adjoint displacements during each of iteration, instead of the whole stiffness

matrix, that increases the numerical efficiency significantly. In this work the elastic parameters are estimated by optimally minimizing the difference between the computed forces and experimental measurements. A nonlinear adjoint method is derived to calculate the gradient of the objective function. Simulations are conducted on a three-dimensional heterogeneous breast phantom extracting from real imaging including fatty tissue, glandular tissue and tumors. The results demonstrate that the method is efficient and stable to detect tumors in nonlinear biological tissue by reconstruction of complex breast tissue properties. More details about the elastography method for reconstruction of nonlinear breast tissue properties are introduced in Chapter 4.

Finally, encouraged by the accomplishment of linear elasto-mammography and nonlinear elastography, a nonlinear elasto-mammography method is developed to reconstruct nonlinear breast tissue properties. It utilizes the novel nonlinear elastic breast model combined with mammography visualizations. Like linear elasto-mammography, the displacement information is extracted from mammography projections before and after breast compression. The elastic parameters are estimated by optimally minimizing the difference between the computed displacements and experimental measurements. The nonlinear adjoint method, developed in nonlinear elastography, is applied to calculate the gradient of the objective function. It is shown that nonlinear elasto-mammography is stable and robust for characterization of the elastic modulus of breast tissues and tumors from the projective displacement measurement. More details are introduced in Chapter 5.

### 1.3 Diffuse Optical Tomography

Besides elastic properties differences between normal tissues and tumors, it is known that optical properties of tissue also change related with physiological change. Diffuse Optical Tomography (DOT) emerged as a tool to identify and characterize breast tumors by imaging optical properties.



“Diffuse optical tomography is a medical imaging modality in which tissue is illuminated by near-infrared light from an array of sources, the multiply-scattered light which emerges is observed with an array of detectors, and then a model of the propagation is used to infer the localized optical properties of the illuminated tissue” (Boas et al., 2001).

The DOT work can be divided as forward and inverse problem. *Forward problem* can be stated as: given a distribution of light sources on the boundary of a tissue, and a distribution of tissue optical parameters, find the resulting measurements on boundary. *Inverse problem* can be stated as: given distributions of light source and measurements on boundary, derive the tissue optical parameters distribution within the tissue.

For the forward problem, a model should be established to describe the light propagations in tissue. Unlike the radiation in CT, which generally travels in straight lines through the body, infrared light is strongly scattered by tissue (Schweiger, 2003). Arridge (1993) presented a diffusion equation to reflect that light propagations highly diffusively in biological tissues. Some researchers (Arridge et al., 1992; Boas, 1996; Feng et al., 1995) developed analytical solutions, like Greens function solutions, of the diffusion equation. However these models are far too simplistic to model propagation of light through complex tissue. Then statistical modeling techniques based on Monte Carlo method is develop to track individual photons (Boas et al., 2002; Okada and Delpy, 2003; Hayashi et al., 2003). This method offers great flexibility in modeling complex geometries and parameter distributions and the individual photon histories can be derived, but it requires very lengthy computational time (Arridge, 1997). Arridge (1995, 1999, and 2000) introduced a numerical technique based on finite element method (FEM) to solve the diffusion equation. The advantage of the FEM approach is its flexibility to handle complex geometries and its fast speed, which make this numerical technique widely used in DOT. In this thesis, the FEM approach is applied to develop a new algorithm to derive optical properties of breast tissues.

For the inverse problem, the optical properties are reconstructed from the surface measurements of transmitted light intensities. Since the inverse problem is non-unique, ill-posed underdetermined, the major challenge in DOT is to develop efficient and stable algorithm to solve the inverse problem.

Boas (1994), O’Leary (1995), Chang (1995), and Gaudette (2000) developed a linear algorithm to provide an approximate solution to nonlinear inverse problem. However, this method is limited in use since it can only account for small changes in optical properties. If the real values are far from initial guess, the linear algorithm fails to search the real values.

To solve problems related to linear algorithm, nonlinear image reconstruction algorithm is developed (Klose et al., 1999; Saquib et al., 1997; Arridge et al., 1998; Hielscher et al., 1999; Roy et al., 1999). Like in elastography, an objective function is established to compare calculated and measured data. Starting with an initial guesses, the optical parameters are updated to minimize the objective functions. The challenge remains to find efficient ways of updating the initial guesses such that the differences between calculated and measured data become smaller and the value of the objective function decreases. An increasing interest is using gradient-based iterative image reconstruction algorithm (Hielscher et al., 2000). In the gradient approach the image reconstruction problem is interpreted as a nonlinear optimization problem, in which the gradient of optical parameters is applied to minimize the objective function. However, because the large number of measurements and the presence of noise, the commonly used gradient method is time-consuming and causes low spatial resolution. Developing a stable and efficient reconstruction algorithm is still essential in DOT (Arridge et al., 2008).

As we have successfully developed nonlinear adjoint method to provide gradient of the objective function in nonlinear elasto-mammography, we have expanded this method to diffuse optical tomography. We have developed a finite-element-based

algorithm to solve the inverse problem of frequent-domain diffusion equation. The nonlinear adjoint method is expanded to complex domains for the reconstruction of optical parameters. Numerical simulation is carried out and compared with phantom experiments. The results show our adjoint-based algorithm is efficient and robust for reconstructing the optical properties.

#### 1.4 Scope of the Thesis

The major objective of this thesis is to develop new mechanical and optical methods for breast cancer imaging, which include new-generation nonlinear elasto-mammography and diffusion optical tomography.

In Chapter 2 we have introduced the background of breast tumors and reviewed previous research about mammography, elastography and diffusion optical tomography,

In Chapter 3, we have developed a linear elasto-mammography method which generates the elastograms of breast tissue by combining the conventional X-ray mammography and elastography. The 3-D breast phantoms containing one and two tumors are established. Displacement measured from deformed and undeformed mammography projections are applied as input data to reconstruct the isotropic material parameters for normal breast tissues and tumors. Our numerical simulations demonstrate that unique and accurate results can be obtained using information extracted from only two sets of projections. The effect of displacement noise, geometry mismatch, and material contrast ratio are investigated. The results show that our method is stable and robust.

In Chapter 4, we developed elastography method for reconstruction of nonlinear breast tissue properties. A 3-D model is developed for heterogeneous breast tissues extracting from real images including fatty tissue, glandular tissue, and tumors. An exponential-form of nonlinear material model is applied. Based on the large-deformation constitutive law, discretized nonlinear equations are solved for displacement, strain, and

stress fields in breast tissues with given tumors under external compression at breast boundaries. We develop a 3-D inverse-problem algorithm to reconstruct the material parameters for nonlinear elastic constitutive relation of breast phantoms with tumors. The nonlinear adjoint gradient method is introduced to improve the numerical efficiency and enhance the stability of elastography reconstruction.

Encouraged by the success of linear elasto-mammography and nonlinear elastography, a nonlinear elasto-mammography method was developed to reconstruct nonlinear breast tissue properties in Chapter 5. A 3-D model is used for heterogeneous breast tissues extracting from real images including fatty tissue, glandular tissue, and tumors. Mammography projections are taken in before and after breast compression and displacement information is extracted by comparing the projections. The nonlinear adjoint method is applied to calculate the gradient of the objective function which is based on the difference between the computed displacements and experimental measures. The effect of displacement noise and iterative steps are investigated. It is shown that new-generation nonlinear elasto-mammography is stable and efficient for characterization of the elastic modulus of breast tissues and tumors from the projective displacement measurements.

In Chapter 6, we switch from mechanical to optical methods for breast cancer imaging. We develop a finite-element algorithm based on adjoint method to solve the inverse problem of frequent-domain diffusion equation for soft tissues. With the analytical form of gradients, the adjoint method is expanded to complex domain for the reconstruction of optical parameters in diffuse optical tomography. Specific numerical simulation is carried out and compared with phantom experiment. The results show that the adjoint-based algorithm is efficient and robust for reconstructing the optical parameters.

Chapter 7 provides the conclusions from our current research work and some recommendations for future work.

## CHAPTER 2 LITERATURE REVIEW

### 2.1 Breast Cancer

Cancer is a major threat to public health in the world. Cancer occurs when cells in a part of the body begin to grow out of control. Normal cells divide and grow in an orderly fashion, but cancer cells do not. They continue to grow and crowd out normal cells. Usually, the multiplying cancer cells form a lump called a tumor. Not all tumors are cancerous. Tumors that are not cancerous are called benign tumors. Cells from benign tumors do not spread to other parts of the body, while cancerous tumors, called malignant tumors, can break away from the original, primary tumor and travel through the blood stream to other parts of the body (Figure 2-1).

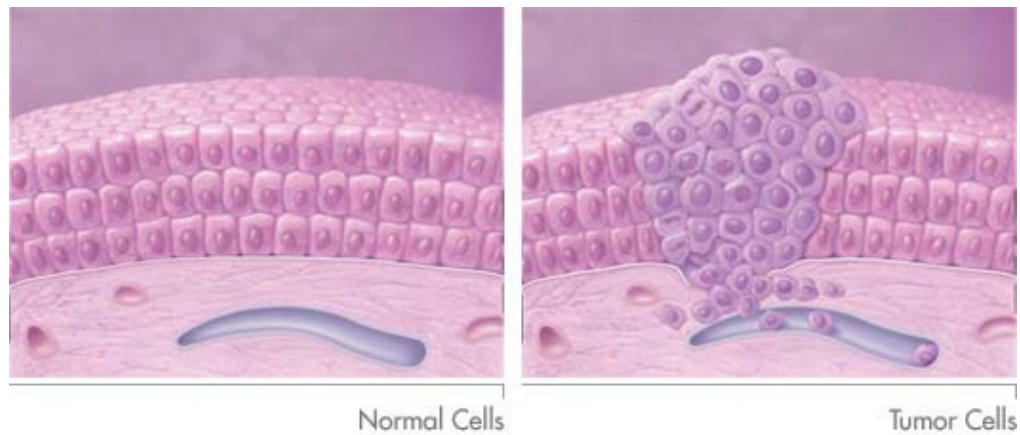


Figure 2-1 Normal and tumor cells

Breast cancer is a malignant tumor that starts from cells of the breast. Breast cancer is one of the most common cancers in western. Approximately 10% of women

will develop breast cancer during the course of their lives in USA and Europe. In the USA, there are approximately 2.6 million people living with breast cancer (NIH-NCI, 2004). American Cancer Society estimated that there were 184,450 new breast cancer cases in US in 2008, and 194,280 in 2009, which is about 27% of all new cancer cases for women. And deaths of breast cancer were estimated 40,480 in 2008 and 40,170 in 2009, which is about 15% of all deaths of cancers (American Cancer Society, 2008, 2009).

The specific causes of breast cancer are yet unknown. Some research has shown the early detection of the breast tumor is the key to successful treatment. For example, a 20-year follow of 2468 breast cancer cases from the Swedish Two-County has been done by Tabár and Dean (2003). After 20 years since operation, more than 90% women with tumor size less than 10 mm survive, but survival of the women with tumor larger than 50 mm is less than 20% (Figure 2-2). These data clearly show that detecting breast cancer in the smaller size is a substantial improvement in outcome.

## 2.2 Mammography

Currently, X-ray mammography is the primary method for early detection and characterization of breast tumors (Muller, 1999; Nass et al., 2001; Fletcher and Elmore, 2003). Mammography is a specific type of imaging that uses a low-dose X-ray system for the examination of breasts. A mammography exam, called a mammogram, is used to aid in the early detection and diagnosis of breast diseases in women. An X-ray, the oldest and most frequently used form of medical imaging, is a noninvasive medical test that helps physicians diagnose and treat medical conditions. Imaging with X-rays involves exposing a part of the body to a small dose of ionizing radiation to produce pictures of the inside of the body. According to the reports of US Food and Drug Administration, mammography can find 85 to 90 percent of breast cancers in women over 50, and can detect a lump up to two years before it can be sensed by manual palpation. Figure 2-3 is a typical mammography imaging, by which a tumor could be seen easily.

### Cumulative survival of women 40-74 years with invasive breast cancer by tumor size

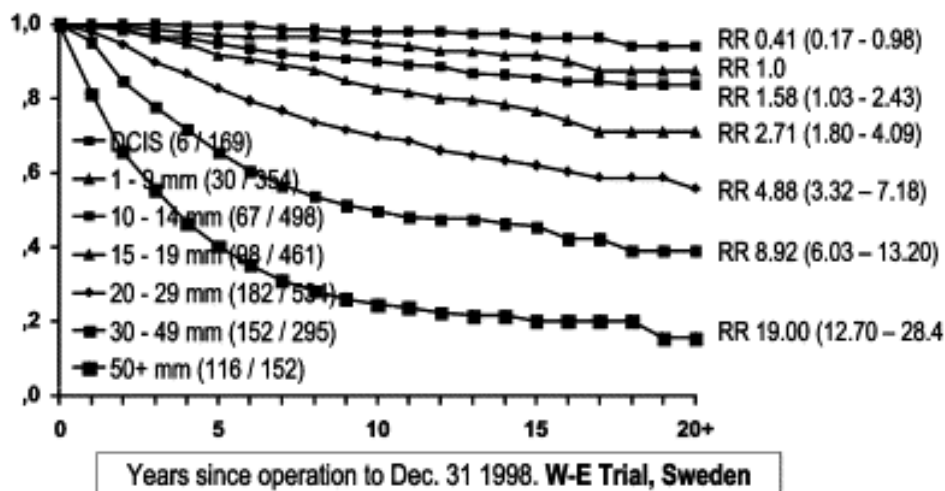


Figure 2-2 Results of a 20-year follow-up of 2468 breast cancer cases from the Swedish Two-County

Source: Tabár, L., and Dean, P.B., 2003, "Mammography and breast cancer: the new era", *International Journal of Gynecology & Obstetrics*, **82** (3), 319-326.

While it is more effective in detecting tumors as age increases and the breast becomes fatty, mammography fails to detect small cancers (less than 8 mm) in dense breasts. On the other hand, mammography is not quite specific in terms of tumor benignity and malignancy. Approximate 80% of suspicious masses referred by mammography for surgical breast biopsy are in fact not malignant (Bone et al., 1997; Giger et al., 2000; Kornguth et al., 2001; Plewes et al. 2000). The number of unnecessary benign biopsies that are performed annually approaches 1 million. Using an average reimbursement for an open breast biopsy of \$2400 (Burkhardt and Sunshine, 1999), the financial cost of benign breast tumors to healthcare system is on the order of \$2 billion

annually (Thitaikumar et al., 2008). Meanwhile, these false-positive mammograms may create patients' anxiety, distress and intrusive thoughts.

A number of techniques are currently being explored to overcome these difficulties associated with mammography. Elastography and diffusion optical tomography are two of them. The methods of elastography and diffusion optical tomography are reviewed in Section 2.3 and 2.4.

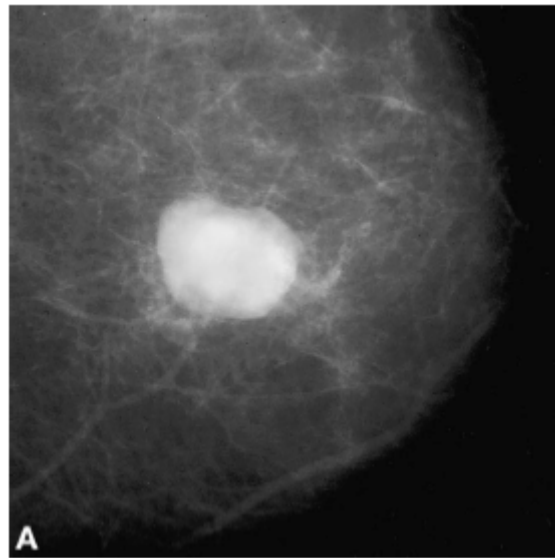


Figure 2-3 A typical mammography imaging, a tumor could be seen easily

---

Source: Kornguth, P.J., Bentley, R.C., 2001, "Mammography-pathologic correlation: Part I. Benign breast lesions", *Journal of women's imaging*, **3**(1), 29-37.



## 2.3 Elastography

### 2.3.1 Introduction

Elastography is a method to imaging of the elastic properties of tissues to provide useful clinical information (Gao et al., 1996).

The breast is a many layered, inhomogeneous structure composed of many different kinds of tissue. The two predominant types of tissue within the breast are fat tissue and glandular tissue which support lactation (Wellman et al., 1999). It is widely known that there is difference of elastic modulus (stiffness) among normal breast tissues and tumors. More than 90% of breast cancers arise in the cells lining the ductal systems of the breast and are correspondingly called ductal carcinomas (Kopans 1998, Giger et al., 2000). Tumors confined to the ducts themselves are designated ductal carcinomas in situ (DCIS), which are the initial stage of malignant tumors. Pathological changes of these DCIS are known to be correlated with changes in tissue stiffness, resulting in extremely hard modulus. Studies suggest a 15-fold increase in the Young's modulus of breast cancer compared with normal breast tissue while benign tumors are only a 5-fold stiffer than normal tissue. Therefore, the tissue stiffness plays an important role for diagnosis of breast cancers, as tumors are stiffer than the surrounding breast tissues and malignant tumors are much stiffer than benign ones (Sarvazyan, 1995; Skovoroda, 1995).

Here we introduce an experiment about the difference of breast tissue stiffness. Wellman et al. (1999) measured stiffness of different breast tissues in compression. The tissue samples tested were obtained during surgery and were tested immediately after removal from the body. Eight breast tissues (Fat, Gland, Phyllodes tumors, Papilloma, Lobular Carcinoma, Fibroadenoma, Infiltrating Ductal Carcinoma, Ductal Carcinoma in Situ) were tests, where Papilloma, Lobular Carcinoma and Fibroadenoma are benign tumors and Phyllodes tumor, Infiltrating Ductal Carcinom and Ductal Carcinoma in Situ are malignant tumors.

The results are shown in Table 2-1 and Table 2-2. The conclusion can be made that there is a significant correlation between tissue histology and stiffness. The stiffness ratio of fat to infiltrating ductal cancer is 10:1 at 1% strain and approximately 80:1 at 15% strain. And it is proved that there is a significant difference in the stiffness between cancerous and benign breast tissues. Infiltrating Ductal Cancer is more than 10 times as stiff as normal fat tissue at 1% strain, and more than 70 times as stiff at 15% strain. While Papilloma is about 5 times as stiff as normal fat tissue at 1% strain and about 30 times as stiff as 15% strain.

Therefore elastic properties are good indicator of histological diagnosis, in other words, *in vivo* identification of elastic moduli of normal and abnormal tissues should improve the accuracy of cancer diagnosis.

Elastography is proposed as a method to imaging tissue elastic modulus in quantitative manner. The general basis of elastography is to induce motion within the tissue under investigation by either an external or internal mechanical stimulation. Conventional medical imaging modalities are then used to measure the spatial deformation, from which the elastic properties can subsequently be reconstructed. The major medical imaging modalities in elastography are ultrasound and magnetic resonance (MR) techniques.

### 2.3.2 Ultrasound Elastography (USE)

Ultrasound elastography was first developed in the 1990s by Ophir's group (Ophir et al., 1991 & 1999; Garra et al., 1997; Righetti et al., 2002). Ultrasound elastography is an imaging modality that is able to map the local strains that a tissue experiences due to the application of the compression. An ultrasound transducer is used to apply a small axial compression to tissue. Sonograms obtained without and with compression are correlated to determine the displacement at each location, thereby revealing the longitudinal strain distribution. The local strain is a relative measure of

elasticity since it depends on the magnitude of compression and on the elastic modulus of the materials. If certain tissue regions have different stiffness than others, the level of strain in those regions will generally be higher or lower than those in the surrounding material. The calculation requires an estimate of local stress distribution, which in turn depends on the spatial composition of the object and knowledge of the applied stress distribution.

Table 2-1 Average elastic modulus and the standard deviation of the modulus for each of eight different types of breast tissues tested

Tissue Type	Elastic Modulus in Strain 0.01	SD	Elastic Modulus in Strain 0.05	SD	Elastic Modulus in Strain 0.10	SD	Elastic Modulus in Strain 0.15	SD
Fat	4.8	2.5	6.6	7	10.4	7.9	17.4	8.4
Gland	17.5	8.6	33	12.0	88.1	66.7	271.8	167.7
Phyllodes Tumor	56.6	0.0	90.8	8.6	164.3	0.0	297.7	0.0
Papilloma	22.2	5.8	54.4	19.7	169.7	80.6	537.8	209.1
Lobular Carcinoma	34.7	0.0	78.9	0.0	221.8	0.0	628.4	0.0
Fibroadenom	45.5	20.1	100.5	39.6	288.4	110.9	889.2	205
Infiltrative Ductal Carcinoma	47.1	19.8	115.7	42.9	384.5	126.9	1366.5	348.2
Ductal Carcinoma in Situ	71.2	0.0	188.7	0.0	638.7	0.0	2162.1	0.0

Source: Wellman, P., 1999, "Tactile imaging", Ph.D. dissertation, Harvard University, Cambridge, Mass, USA.

Table 2-2 The ratio of elastic modulus of each tissue to fat at 4 different strain levels

Tissue Type	Ratio to Fat at			
	Strain= 0.01	Strain= 0.05	Strain= 0.10	Strain= 0.15
Gland	4	5	8	16
Phyllodes Tumor	12	14	16	17
Papilloma	5	8	16	31
Lobular Carcinoma	7	12	21	36
Fibroadenoma	9	15	28	51
Infiltrating Ductal Carcinoma	10	18	37	79
Ductal Carcinoma in Situ	15	29	61	124

Source: Wellman, P., 1999, "Tactile imaging", Ph.D. dissertation, Harvard University, Cambridge, Mass, USA.

Ophir et al. (1991) compressed the soft tissue by the transducer and measured the displacement along the direction of compression. The strain profile along the transducer axis is computed. By assuming the stresses applied by the compressing device, the strain profile is converted to an elastic modulus profile. Then, Ophir et al. (1999) present the basic stiffness measurements, and describe four types of elastograms, including axial strain, lateral strain, modulus and Poisson's ratio elastograms. A review of such work is given by Ophir et al. (2002). Figure 2-4 shows the *in vivo* elastogram of an invasive ductal carcinoma. The lesion is clearly visible as a dark area on the elastogram. While these studies use 2D ultrasound imaging, a few researches were carried out to develop 3D ultrasound elastography (Lindop et al, 2006; Treece et al., 2008; Richards et al., 2009)

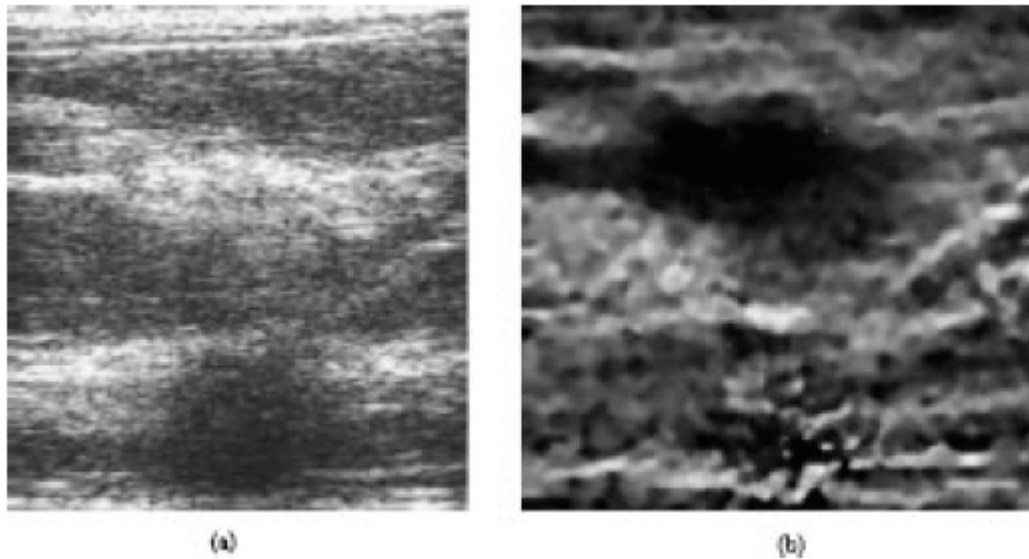


Figure 2-4 The sonogram (a) and elastogram (b) of an invasive ductal carcinoma in vivo at 5 MHz. The lesion is clearly visible as a dark (hard) area on the elastogram

---

Source: Ophir, J., Alam, S.K., Garra, B., Kallel, F., Konogagou, E., Krouskop, I., Varghese, I., 1999, “Elastography: Ultrasonic estimation and imaging of the elastic properties of tissues”, *Proc. Instn. Mech. Engr. Part H*, **213**, 203-233.

In contrast with quasi-static compression, other researchers (e.g., Alam et al., 1994; Gao et al., 1997; Fatemi et al., 1998 & 2002; Doyley et al., 2001; Hiltawsky et al., 2001) applied low-frequency vibration as mechanical stimulation.

Recently, beside strain field and elastic modulus, additional features are studies aiming to improve the tumor classification. Thitaikumar et al. (2008) reported the research about bonding at an inclusion boundary using axial-shear strain elastography. It is known that malignant tumors are generally more firmly bonded to their surroundings than are benign tumors (Konogagou et al., 2000). By investigating the relationship between the bonding at an inclusion-background boundary and the distribution of axial-

shear strain patterns around an inclusion boundary, Thitaikumar et al. (2009) provided a new feature for tumor classifications.

Recent years some clinical experiments were also carried out based on ultrasound elastography (Barcoff et al., 2003; Regner et al., 2006; Barr, 2006; Itoh et al., 2006; Zhu et al., 2008). For example, Barcoff et al. (2003) used 60 Hz shear waves to stimulate the soft phantom and performed shear wave imaging by ultrasound. Local shear Young's modulus is reconstructed by shear wave field. Then *in vivo* experiments were first conducted on 11 women who had palpable breast lesions. The result is that, among 11 examined patients, 6 of them presented a clear visible tumor in reconstructed elasticity imaging, percentage of successful diagnosis reach 55%. A reason for failing of detection some of tumors is a penetration problem. The penetration depth of shear waves within organic tissue is only a few centimeters, which limit the application for tumors deeply located.

While providing new information to detect pathological tumors, USE suffers from low resolution imposed by the minimum resolvable wavelength. In addition, most of USE elastogram are referred to as the strain imaging which may not always provide useful information on locations and characterizations of heterogeneous lesions (Plews et al., 2000). For example, the phenomenon called "butterfly wings" (Ophir et al., 1999) is frequently observed in USE strain elastograms, which can be misleading with respect to tumor detection.

### 2.3.3 Magnetic Resonance Elastography (MRE)

Magnetic resonance elastography was developed by Ehman and co-workers (Muthupillai et al., 1995; McKnight et al., 2002), Plewes et al. (2000), Samani et al. (2001), Sinkus et al., (2000), and Van Houten et al., (1999, 2001) as new-generation elastography modality.

The general basis of MRE is to induce motion within the tissue by mechanical stimulation, measure the resulting deformation using MRI techniques, and finally, calculate elasticity modulus distribution using an inversion technique. Like in USE, the choice of mechanical stimulation used for elastography generally falls into two categories: harmonic and quasistatic.

Harmonic deformation perturbs tissues at frequencies of 50-100 Hz, generating longitudinal or shear waves throughout the tissue. Modulus is estimated from measurements of wavelength (Manduca et al., 1996 and 2001) or velocity (Bishop et al., 1998). For example, Manduca et al. (2001) directly visualize and quantitatively measure propagating acoustic strain waves in tissue subjected to harmonic mechanical excitation. In a tissue-like phantom experiment, propagating mechanical waves are applied and a phase-contrast MRI technique is used to provide spatially map and measure displacement patterns corresponding to harmonic shear waves. Figure 2-5 (a) shows the image of displacement due to acoustic strain wave propagation in a tissue-simulating phantom. Then the elastic field is reconstructed based on an assumption that the material is isotropic, homogeneous and incompressible. Figure 2-5 (b) shows the reconstructed elastogram and the object is clearly depicted. Figure 2-6 shows the result of an experiment on a patient with known breast tumor. The elastogram indicates that the shear stiffness of the tumor is substantially higher than surrounding tissues.

Alternatively, quasistatic elastography uses very low deformation frequencies of 0–1 Hz to reconstruct elastic field. The tissue is in an approximate state of static stress and displacements could be measured (Plewes et al., 2000; Samani et al., 2001). The key point in this quasistatic elastography is how to reconstruct elastic modulus distribution by displacement measurements. Three methods have been developed, including strain imaging, direct linear method and iterated inversion method.

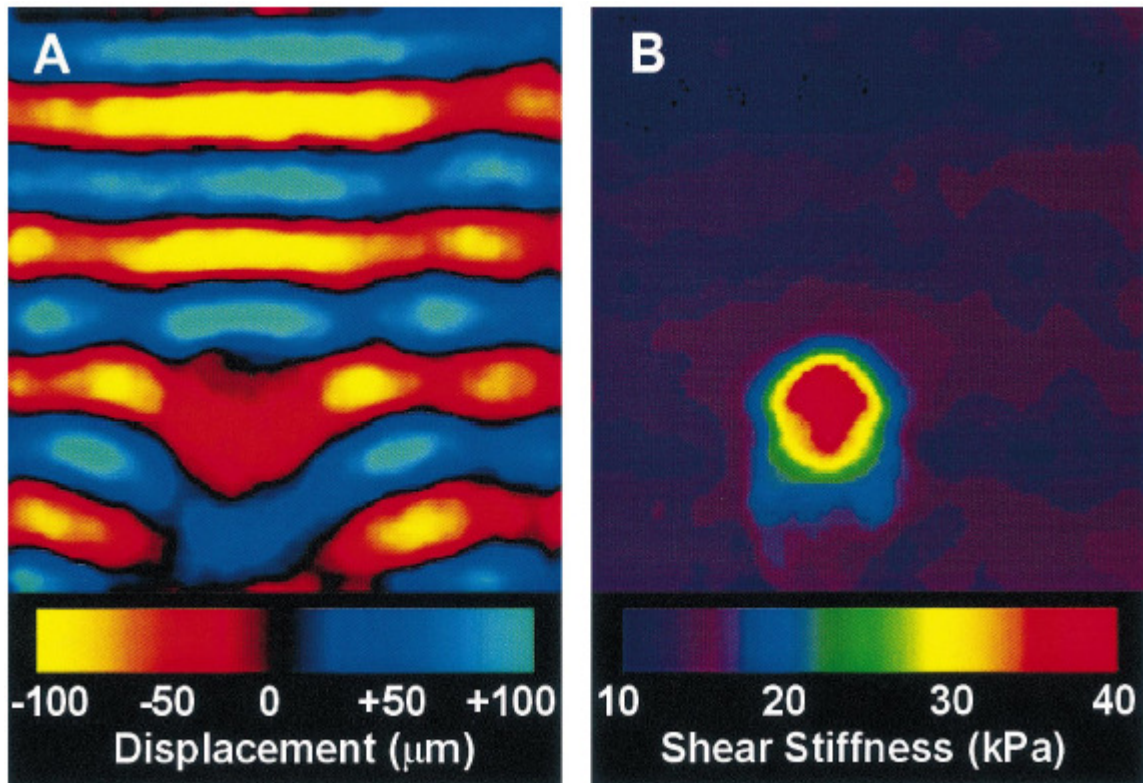


Figure 2-5. The image of displacement and reconstructed elastogram for an object with diameter comparable to wavelength.

Source: Manduca, A., Oliphant, T.E., Dresner, M.A., Mahowald, J.L., Kruse, S.A., Amromin, E., Felmlee, J.P., Greenleaf, J.F., Ehman, R.L., 2001, "Magnetic resonance elastography: Non-invasive mapping of tissue elasticity", *Medical Image Analysis*, **5**, 237-254.

Note: (a) Shear waves propagating in a phantom with an embedded 1.5 cm diameter cylinder of stiffer gel. Shear waves at 300 Hz were applied at the top margin of the gel block, with transverse motion oriented orthogonal to the plane of the image. (b) The elastogram based on local frequency estimation reconstruction algorithm clearly depicts the objects, even though it is relatively small in comparison to the wavelength.



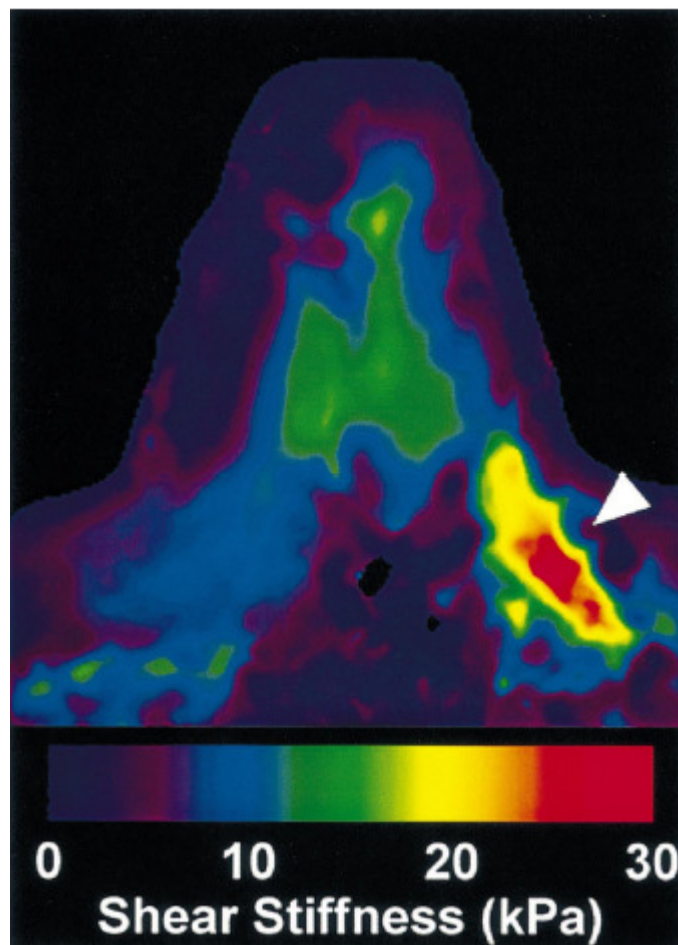


Figure 2-6. MR elastogram of the breast of a patient with a 4 cm diameter, biopsy-proven breast cancer.

---

Source: Manduca, A., Oliphant, T.E., Dresner, M.A., Mahowald, J.L., Kruse, S.A., Amromin, E., Felmlee, J.P., Greenleaf, J.F., Ehman, R.L., 2001, "Magnetic resonance elastography: Non-invasive mapping of tissue elasticity", *Medical Image Analysis*, **5**, 237-254.

Note: The image was obtained with shear waves at 100 Hz, applied to the skin of the medial and lateral aspects of the breast. The field of view is approximately 16 cm and the section thickness is 5 mm. The MR elastogram indicates that the shear stiffness of the tumor in the posterolateral aspect of the breast (arrowhead) is substantially higher than that of normal fibroglandular and adipose tissue in the breast.

Strain imaging method is based on an assumption that the stress field is approximately constant over the local region of the lesion of concern. So the tissue modulus would be related to strain measurement (Ponnekanti et al., 1995; Kallel and Bertrand 1996; Skovoroda et al., 1994). The strain field is measured as an approximate of modulus distribution.

Strain imaging provides a simple approximate of modulus, but in situation where more accurate quantitative measures of tissue elasticity are required, a calculation method must be performed. Under static loading, the deformation of tissues is governed by equations of equilibrium, strain-displacement, and a material constitutive law. If we assume that the deformation is linear and material is isotropic elastic, we can derive the governing equation, known as Navier equation:

$$\nabla(\lambda \nabla \cdot u) + \mu(\nabla^2 u + \nabla \nabla \cdot u) + \nabla \mu(\nabla u + \nabla u^T) = \gamma \frac{\partial u}{\partial t} + \rho \frac{\partial^2 u}{\partial t^2} \quad (2.1)$$

where  $\lambda$  and  $\mu$  are the Lamé constants and  $u$  is the displacement vector field. On the right hand side,  $\gamma$  and  $\rho$  are the material viscous damping constants and density respectively. In the case of quasi-static elastography,  $\gamma$  and  $\rho$  vanish.

In the direct linear method for quasistatic elastography, Equation (2.1) is discretized with modulus as the unknown and may be solved with standard linear algorithms (Hansen, 1998). This requires boundary conditions in terms of the unknown elastic modulus, but it is sufficient to assume a constant boundary modulus to achieve a relative modulus reconstruction. Skovoroda et al. (1995) were the first to describe a direct linear inversion of Equation (2.1) in 2-D plane strain geometry.

In order to handle 3-D complex models and get results less sensitive to noise, an iterated inversion method has been developed by Bishop et al. (1998), Plewes et al. (2000) and Samani et al. (2001). In this method, the nonuniform stress distribution throughout the tissue is used to reconstruct the elasticity modulus from measured displacements. An initial guess of modulus is given, and then strain distribution could be

obtained based on measured displacements. After stress calculation, the procedure is followed by modulus updating. Iterative continues until modulus convergent (Figure 2-7).

Based on this iterative method, a modulus reconstruction for breast cancer assessment is carried out by Samani et al. (2001). A FE model of breast is established and a typical sagittal image of the breast is shown in Figure 2-8 (a) where regions of adipose tissue (bright) and fibroglandular tissue (dark) are easily resolved with high SNR (signal-to-noise ratio). FE mesh illustrated in Figure 2-8 (b) and (c) was created. Figure 2-8 (d) show a compression on model. It is assumed that geometry of normal and suspicious tissues is available from a contrast-enhanced magnetic resonance image and the modulus is constant throughout each tissue volume. Reconstruction results are shown in Figure 2-9. The results indicate that reconstruction error does not exceed 12%. It is indicated that this iterative method is efficient to reconstruct elastic modulus in 3-D complex model.

Recently, some efforts are made to improve iterative reconstruction algorithm. Kwon et al. (2009) designed a shear modulus decomposition algorithm to reduce the degree of noise amplification in the reconstructed shear modulus images without the assumption of local homogeneity. Kolipaka et al. (2009) developed and tested mathematical inversion algorithms capable of resolving shear stiffness in bounded media in stead of a uniform, infinite medium.

From above summary, MRE provides higher resolution imaging and is capable of producing sufficient 3-D spatial and contrast resolution. However MRE tumor detection may encounter a penetration problem when applied to breast cancer diagnosis *in vivo*. The penetration depth of shear waves within organic tissue is only a few centimeters, which limit the application of MRE for tumors deeply located. Meanwhile magnetic resonance is too expensive to be applicable for all patients.

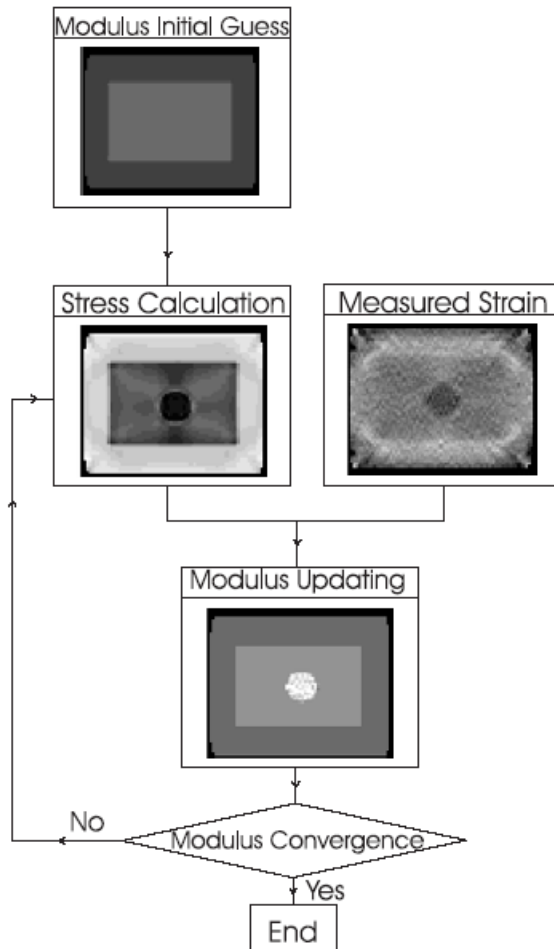


Figure 2-7. Flow chart of the iterative method for reconstructing elastic modulus.

---

Source: Plewes, D.B., Bishop, J., Samani, A., Sciarrenta, J., 2000, "Visualization and quantification of breast cancer biomechanical properties with magnetic resonance elastography", *Phys. Med. Biol.*, **45**, 1591-1610.

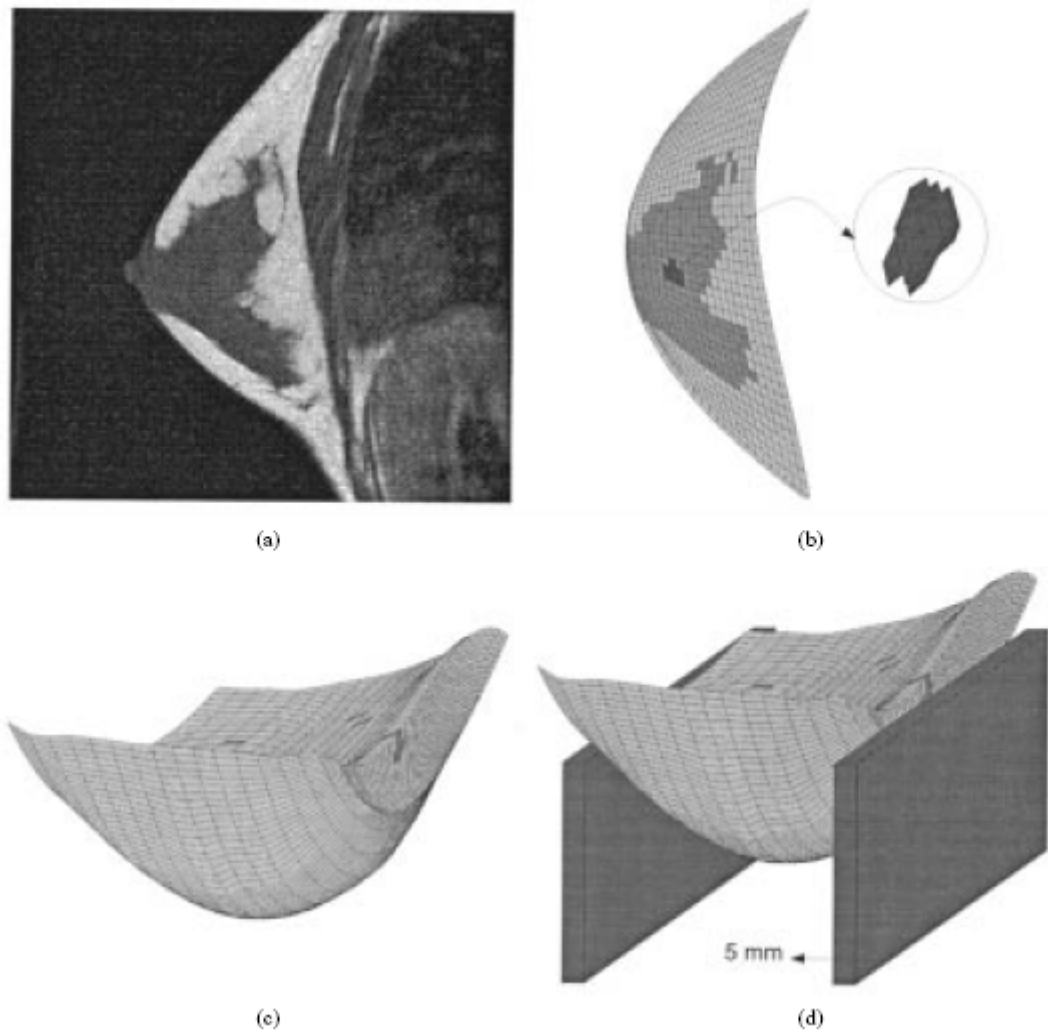


Figure 2-8 Finite element model of the breast.

Source: Plewes, D.B., Bishop, J., Samani, A., Sciarrenta, J., 2000, “Visualization and quantification of breast cancer biomechanical properties with magnetic resonance elastography”, *Phys. Med. Biol.*, **45**, 1591-1610.

Note: (a) Magnitude image of a central slice through the breast. (b) FE mesh corresponding to the slice shown in (a) where the tumor shown in the circle is added. (c) FE mesh of the breast. (d) FE contact problem model for compression simulation.

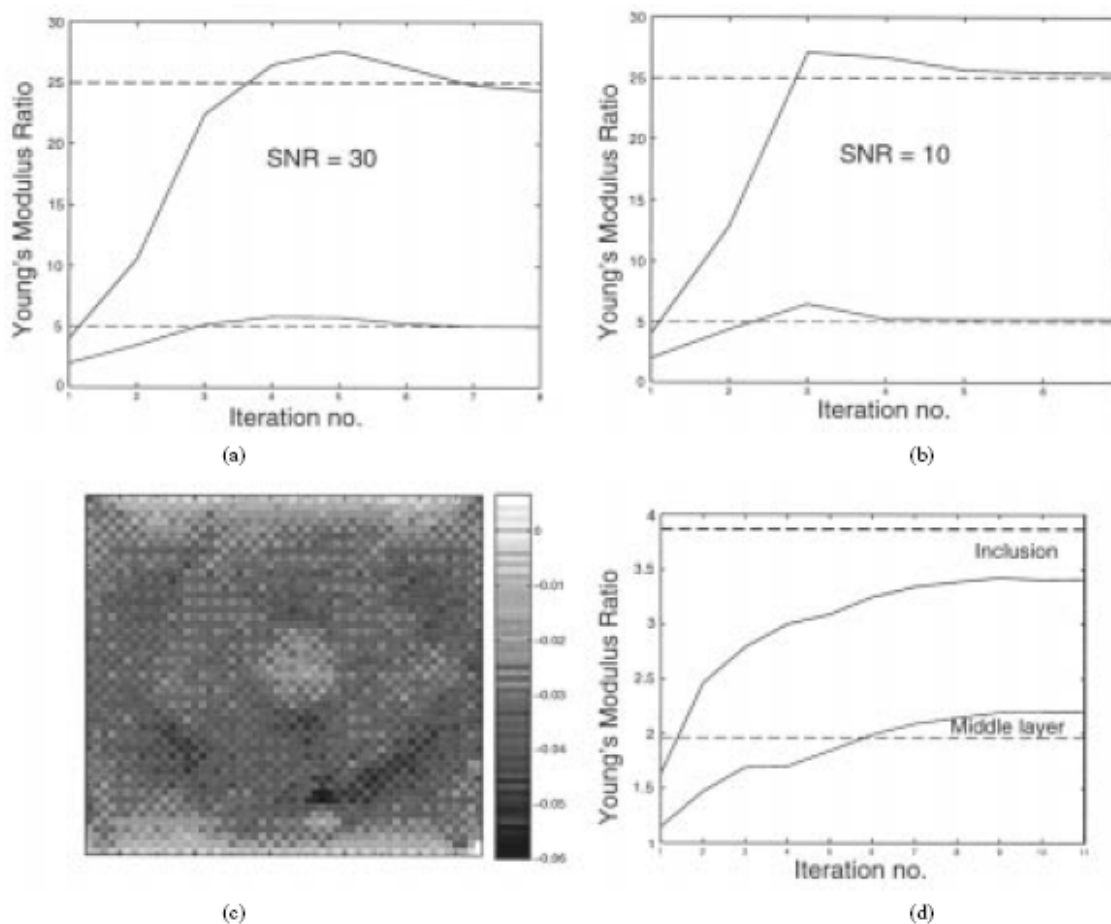


Figure 2-9 Modulus reconstruction results.

Source: Plewes, D.B., Bishop, J., Samani, A., Sciarrenta, J., 2000, "Visualization and quantification of breast cancer biomechanical properties with magnetic resonance elastography", *Phys. Med. Biol.*, **45**, 1591-1610.

Note: (a) and (b) Convergence of  $E_{fib}/E_{fat}$  and  $E_{tum}/E_{fat}$  of the breast to the true values (dashed lines) for SNRs (signal-to-noise ratio) of 30 and 10 where  $E_{fat}$ ,  $E_{fib}$  and  $E_{tum}$  are the Young's modulus of fat, fibroglandular tissue, and tumor, respectively. (c) Measured strain in the phantom's middle slice. (d) Convergence of  $E_{fib}/E_{fat}$  and  $E_{tum}/E_{fat}$  where  $E_{fat}$ ,  $E_{fib}$  and  $E_{tum}$  are the Young's modulus of the outer layer, middle layer, and the inclusion, respectively. The reconstruction results indicate that reconstruction error for both the middle layer and the inclusion does not exceed 12%.

In summary, the general idea of elastography is to induce motion within the tissue by mechanical stimulation, measure the resulting deformation using suitable imaging techniques, and finally, calculate elasticity modulus distribution using an inversion technique. By reviewing the elastography methods, it is shown that three major challenges: imaging techniques, deformation theory and inversion techniques, are essential for elastography in clinical application.

(1) Imaging techniques: an imaging technique should be selected to measure deformation in elastography. Currently ultrasound and magnetic resonance are widely used. But ultrasound has a low resolution, magnetic resonance suffers penetration problem and is too expensive for the general population. In this thesis, we develop new-generation elasto-mammography, in which traditional X-ray is used to measure displacements. More details are introduced in chapter 3 and 5.

(2) Deformation theory: both USE and MRE are based on infinitesimal-strain linear elastic deformation theory, and only very few have considered anisotropic tissue properties. The large deformation, nonlinear and anisotropic behaviors of breast tissues and tumor have yet to be taken into consideration. In this thesis, we develop new algorithm to simulate the large deformation, nonlinear and anisotropic behaviors of breast tissues. More details are introduced in chapter 4 and 5.

(3) Inversion techniques: once displacements are measured, an inversion technique is applied to reconstruct elastic properties. Strain imaging, direct linear and iterated inversion methods have been developed in current USE and MRE, but an efficient and robust algorithm is still a challenge for elastography in clinical application. In this thesis an adjoint gradient method is introduced to improve the numerical efficiency and enhance the stability of elastography reconstruction. More details are introduced in chapter 3~5.

## 2.4 Diffuse Optical Tomography (DOT)

### 2.4.1 Introduction

Because the mammography is not quite specific in terms of tumor benignity and malignancy, elastography has been developed to detect breast tumors by recognizing elastic stiffness differences between normal soft tissues and tumors in breast. Two kinds of elastography, ultrasound elastography (USE) and magnetic resonance elastography (MRE) have been introduced in Section 2.3.

Besides of elastic properties differences between normal tissues and tumors, it is known that optical properties of tissue also play important role in clinical diagnostic. All healthy tissues need an adequate blood supply, delivering sufficient oxygen. Red blood cells deliver oxygen to tissues by attaching to oxygen in the lungs and becoming oxy-haemoglobin. At the tissue, the oxygen dissociates to leave deoxy-haemoglobin. The relative concentrations of oxy- and deoxy- haemoglobin in the blood tells us how well oxygenated the blood is. If malignant tumors exist in breast tissue, they are often associated with anomalous vasculature and different oxygenation to the surrounding tissue. Meanwhile it is found that the optical properties of oxy- and deoxy- haemoglobin are different (Hillman, 2002; Leff et al., 2007). The absorptions of oxy- and deoxy-haemoglobin are shown in Figure 2-10. In addition, malignant and benign tumors have distinctive optical characteristics, which are summarized in Table 2-3. Therefore, optical properties could be a good indicator to identify and characterize the breast tumors. Diffuse optical tomography (DOT) emerged as a tool to image optical properties related with physiological change.

“Diffuse optical tomography (DOT) is an medical imaging modality in which tissue is illuminated by near-infrared light from an array of sources, the multiply-scattered light which emerges is observed with an array of detectors, and then a model of



the propagation is used to infer the localized optical properties of the illuminated tissue” (Boas et al., 2001).

In mammography and elastography, X-ray and MRI are usually used to measure breast tissue internal structure. But X-ray is potentially harmful to patients and MRI requires a large and expensive instrument with considerable maintenance costs. DOT overcomes these drawbacks. DOT operates at wavelengths at the red end of the visible spectrum and in the near- infrared range, around 650 to 900 nanometers. This spectral range is called a window of transparency because it lets light propagate relatively deeply into the tissue before being absorbed.

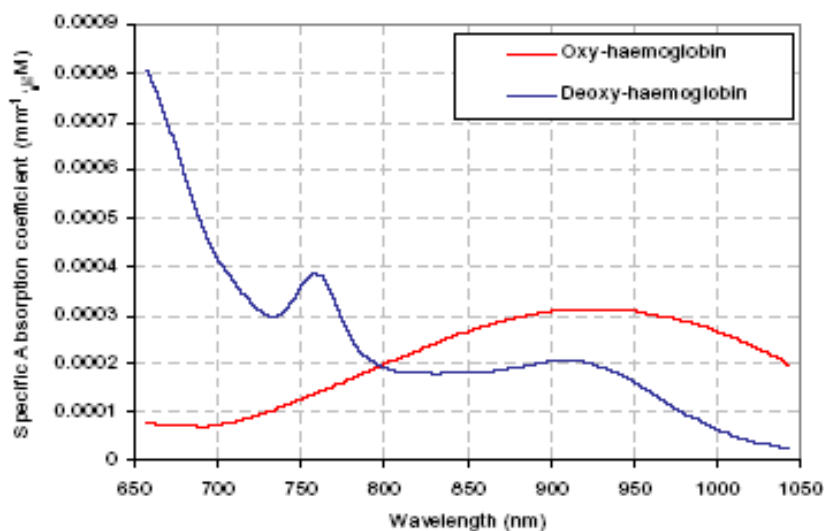


Figure 2-10 The absorption spectra of oxy- and deoxy-haemoglobin in the near infrared wavelength range

---

Source: Hillman, E.M.C., 2002, “Experimental and theoretical investigations of near infrared tomographic imaging methods and clinical applications”, Ph.D. thesis, University College London.

Table 2-3. Different malignant and benign breast tumors and their potential optically detectable features

Condition	Type	Shape	Likely to manifest as
Cyst	Benign	Round and smooth	Low scatter
Blood filled cyst	Possibly malignant	Round and smooth	High/characteristic absorption, possibly low scatter
Fibroadenoma	Benign	Round, mobile	High scatter, possibly high absorption, normal vasculature(common in younger women)
Fibrocystic/ Fibroglandular changes	Benign	Boundaries not discrete	High scatter (common in older women)
Dormant Tumour	Malignant	Small, within ducts or lobes	Possibly necrotic (de-oxygenated) core
Growing tumour	Malignant	Boundaries not discrete	Increased vasculature (hence increased absorption, scatter and anomalous oxygenation), may also have necrotic core

Source: Hillman, E.M.C., 2002, "Experimental and theoretical investigations of near infrared tomographic imaging methods and clinical applications", Ph.D. thesis, University College London.

The idea of DOT is to reconstruct the optical properties of tissues to detect possible physiological change. A big challenge in DOT is, unlike the radiation in CT, which generally travels in straight lines through the body, infrared light is strongly scattered by tissue (Schweiger, 2003). In Figure 2-11, (a) illustrates how photons may travel in tissue, (b) shows a simulation of relative probability of photon paths. The source and detector are on the top of the block, and the various images show vertical slices at a sequence of horizontal displacements from the line connecting the source-detector pair. Figure 2-12 gives a comparison of CT and DOT imaging, (a) shows a schematic view of

the straight-line projections encountered in CT imaging, and (b) shows a photon density field calculated for a scattering medium with an embedded rectangular object. Therefore, the first challenge in DOT is to develop appropriate models to describe the photon transportation in biological tissue.

#### 2.4.2 Models of Photon Transport in Tissue

Although in principle Maxwell's equations can be solved for complex system with spatially varying permittivity, in practice most models are based on a particle interpretation of light (Arridge et al., 1997). The most widely applied equation in optical imaging is the radiative transfer equation (RTE) (Chandrasekhar, 1950; Ishimaru, 1978).

$$\left(\frac{1}{c} \frac{\partial}{\partial t} + \hat{s} \cdot \nabla + (\mu_a + \mu_s)\right) \phi(r, \hat{s}, t) = \mu_s \int_{S^{n-1}} \Theta(\hat{s}, \hat{s}') \phi(r, \hat{s}', t) d\hat{s}' + q(r, \hat{s}, t) \quad (2.2)$$

which describes the change of the radiance  $\phi(r, \hat{s}, t)$  at position  $r$  in direction  $\hat{s}$  in time  $t$ . The parameters  $\mu_a$  and  $\mu_s$  are the absorption and scattering coefficients respectively,  $c$  is the velocity of light in the medium, and the function  $\Theta(\hat{s}, \hat{s}')$  is the scattering phase function characterizing the intensity of a wave incident in direction  $\hat{s}'$  scattered in direction  $\hat{s}$ .

In biological tissues light propagations highly diffusively, the RTE could be simplified to a diffusion equation (Arridge, 1999; Gibson et al., 2005)

$$-\nabla \cdot D_x(r) \nabla \Phi(r, t) + \mu_a \Phi(r, t) + \frac{1}{c} \frac{\partial \Phi(r, t)}{\partial t} = q_0(r, t) \quad (2.3)$$

where photon density  $\Phi(r, t) = \int_{S^{n-1}} \phi(r, \hat{s}, t) d\hat{s}$ ,  $q_0(r, t)$  is source function, the diffusion coefficient  $D_x = 1/(3(\mu_a + \mu_s))$ .

Equation (2.3) is in time-domain, the corresponding frequency-domain form is:

$$-\nabla \cdot D_x(r) \nabla \Phi(r, \omega) + \mu_a \Phi(r, \omega) + \frac{i\omega}{c} \Phi(r, \omega) = q_0(r, \omega) \quad (2.4)$$

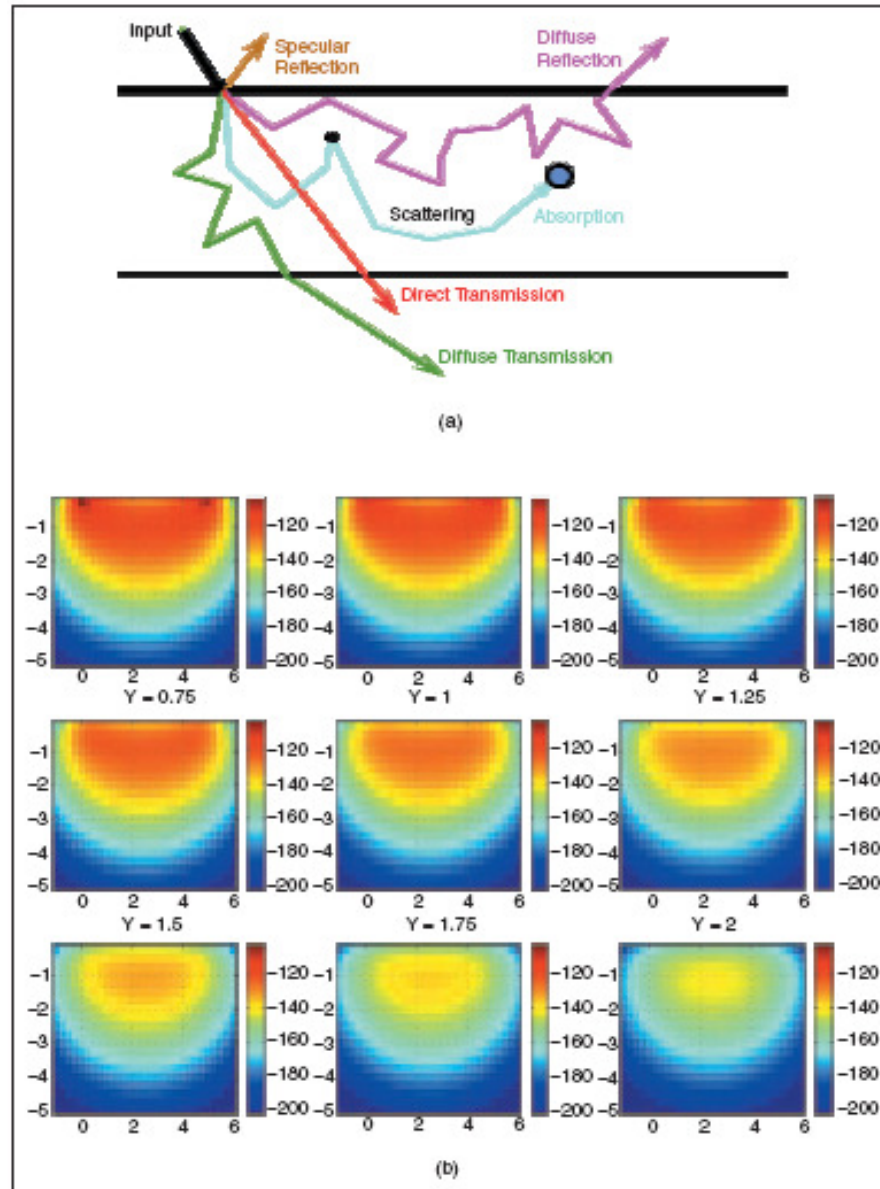


Figure 2-11 Photons travel in tissues.

Source: Boas, D.A., Brooks, D.H., Miller, E.L., DiMarzio, C.A., Gaudette, R.J., Guan, Zhang, 2001, "Imaging the body with diffuse optical tomography", *IEEE Signal Processing Magazine*, **18**(6), 57-75.

Note: (a) visualizes paths of photons through tissue, and (b) shows how probability of photon travel is distributed in a 3-D volume computational model with source and detector on the top. Source and detector are separated by 5 cm, each image shows a vertical slice, and distances shown are displacement of vertical slice from the line connecting the source/detector pair.

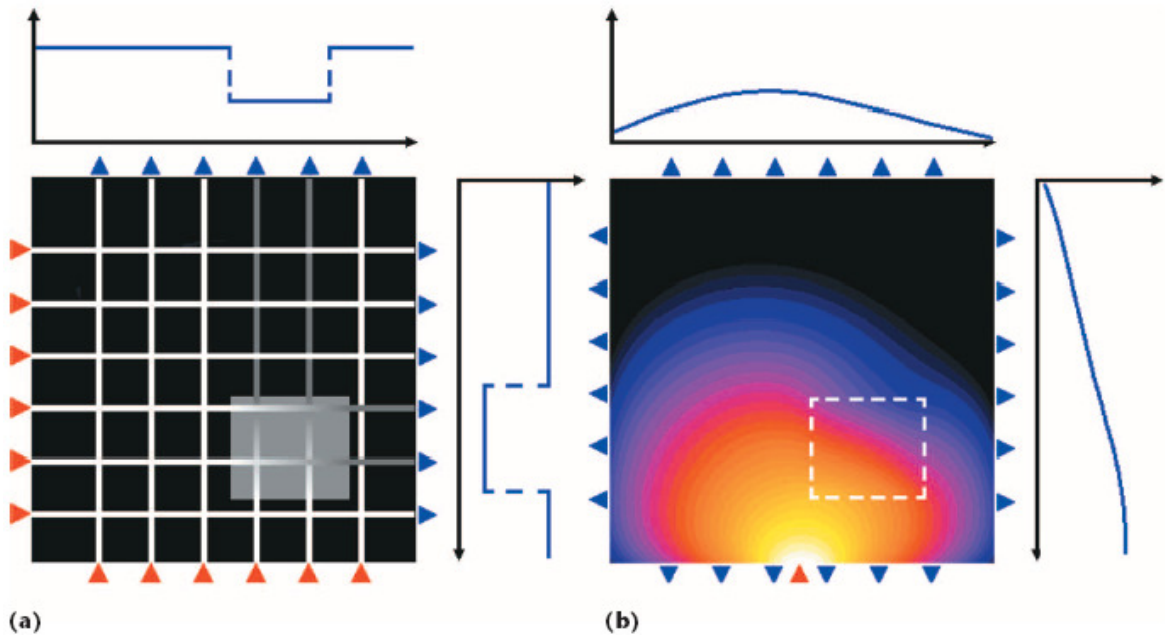


Figure 2-12 Diffuse light transports

Source: Schweiger, M., Gibson, A., Arridge, A.R., 2003, "Computational aspects of diffuse optical tomography", *Computing in Science & Engineering*, **5**(6), 33-41.

Note: (a) A schematic view CT-like projections along straight lines, where included object cast "shadows" on the opposite detector array. (b) Photon density wave from a single source propagating through a diffuse medium with an embedded object. Detectors places around the source maximize data information

### 2.4.3 Forward Problem

The DOT work can be divided as forward and inverse problem. Forward problem can be stated as: given a distribution of light sources on the boundary of a tissue, and a distribution of tissue optical parameters, find the resulting measurement on boundary. Inverse problems can be stated as: given distributions of light sources and measurements on boundary, derive the tissue optical parameters distribution within the tissue. First we review the techniques to solve forward problem.

#### 2.4.3.1 Analytical Modeling Techniques

Green's function is a method for modeling the diffusion equation analytically. The Green's function is the solution when the source is a spatial and temporal  $\delta$  - function, from which solutions for extended sources can be derived by convolution. But this method only is available for simple homogeneous objects (Arridge et al., 1992) or media which include a single spherical perturbation (Boas et al., 1994). This analytical modeling technique is hard to apply on clinical complex geometries.

#### 2.4.3.2 Statistical Modeling Techniques

Statistical modeling techniques model individual photon trajectories in tissues. Monte Carlo method is the commonly used statistical technique in diffuse optical tomography (Boas et al., 2002; Okada and Delpy, 2003; Hayashi et al., 2003). Monte Carlo method focuses on individual photons that are simulated as they undergo scattering and absorption events governed by local values of optical parameters. Photons are followed until absorbed or escape the surface, thus contributing to a measurement. This method offers great flexibility in modeling complex geometries and parameter distributions and the individual photon histories can be derived, but it requires very lengthy computation times (Arridge et al., 1997).

Another statistical method is random walk theory, in which photon transport is modeled as a series of steps on a discrete cubic lattice. The time steps may be discrete or continuous. Random walk theory is particularly suited to modeling time-domain measurements (Weiss et al., 1998; Chernomordik et al., 2000, 2002a & 2002b; Dagdug et al., 2003)

#### 2.4.3.3 Numerical Modeling Technique

Numerical technique based on finite element method (FEM), a numerical method for solution of partial differential equations in complex geometries, is the most widely used one in DOT. This method was first introduced by Arridge et al. (1993) and was explained in detail by Arridge and Schweiger (1995), Arridge (1999, 2000). The finite element method requires that the tissue is divided into a finite element mesh. According to the boundary conditions, the forward problem is reduced to finite size matrix algebra. Recall the time-domain diffusion equation (2.3), a solution  $\Phi$  of Equation (2.3), if it exists, is also a solution of

$$\int \Psi(r)(\nabla \cdot D_x(r)\nabla - \mu_a + \frac{1}{c} \frac{\partial}{\partial t})\Phi(r,t)d\Omega = -\int \Psi(r)q_0(r,t)d\Omega \quad (2.5)$$

where  $\Psi$  is a function satisfying the same boundary conditions as  $\Phi$ .

Equation (2.5) is called weak form of Equation (2.3). By deriving  $\Phi$  and  $\Psi$  into finite elements and integration by parts, Equation (2.5) is derived as:

$$[K(D_x) + C(\mu_a)]\Phi + M \frac{\partial \Phi}{\partial t} = Q + \beta \quad (2.6)$$

where

$$K_{ij} = \int D_x(r)\nabla \Psi_j(r) \cdot \nabla \Psi_i(r)d\Omega,$$

$$Q_j = \int \Psi_j(r)q_0(r,t)d\Omega,$$

$$C_{ij} = \int \mu_a(r)\Psi_j(r)\Psi_i(r)d\Omega,$$

$$\beta_j = \int \Psi_j(r) \Gamma(r, t) d(\partial\Omega),$$

$$M_{ij} = \int \Psi_j(r) \Psi_i(r) d\Omega.$$

For the time-independent case, Equation (2.6) is simplified as

$$[K(D_x) + C(\mu_a)]\Phi = Q + \beta \quad (2.7)$$

For forward problem,  $K(D_x) + C(\mu_a)$  and  $Q + \beta$  are known,  $\Phi$  can be solved by matrix algebra.

#### 2.4.4 Inverse Problem

The key point in DOT is solving the inverse problem, in which the distributions of light sources and measurements on boundary are given and the image of tissue optical parameters are reconstructed. Since the inverse problem is non-unique, ill-posed underdetermined, developing fast and robust reconstruction methods is the main challenge in making DOT a viable tool for clinical diagnostics.

##### 2.4.4.1 Linear Image Reconstruction

Inverse problem can be expressed as

$$x = F^{-1}(y) \quad (2.8)$$

where  $x$  is internal optical properties distribution,  $y$  is given measurements on boundary. It is a non-linear problem but it can be linearized if the actual optical properties  $x$  are close to an initial estimate  $x_0$  and the measured data  $y$  are close to the simulated measurements  $y_0$ . A Taylor series of Equation (2.8) about  $x_0$  is

$$y = y_0 + F'(x_0)(x - x_0) + F''(x_0)(x - x_0)^2 + \dots \quad (2.9)$$

If  $x$  is close to  $x_0$  and  $y$  is close to  $y_0$ , Equation (2.9) is simplified as

$$\Delta y = J \Delta x \quad (2.10)$$

where  $\Delta y = y - y_0$ ,  $\Delta x = x - x_0$ ,  $F'$  is represented as matrix  $J$ .

The most common techniques to solve Equation (2.9) are truncated singular value decomposition, Tikhonov regularization and the algebraic reconstruction technique (Boas



et al., 1994; O’Leary et al., 1995; Chang et al., 1995; Gaudette et al., 2000; Selb et al., 2007). The Moore-Penrose inverse  $J^{-1} = J^T(JJ^T)^{-1}$  offer a more efficient inversion if  $J$  is underdetermined. The linear inverse problem can be expressed as a

$$(JJ^T + \lambda I)\Delta x = J^T \Delta y \quad (2.11)$$

where  $I$  is the identity matrix and  $\lambda$  is a regularization parameter.  $J$  itself is calculated from the forward model.

#### 2.4.4.2 Non-linear Image Reconstruction

The linear image reconstruction provides an approximate solution to nonlinear inverse problem, but it is based on the assumption that actual optical properties are close to an initial estimation. If the inverse problem is to reconstruct absolute values that are far away from initial guesses, which is commonly the case in breast imaging (Dehghani et al., 2003), non-linear image reconstruction has been applied.

To solve the non-linear problem, an objective function  $\Psi$  is defined

$$\Psi = \|y - f(x)\|^2 + \alpha \|II\|^2 \quad (2.12)$$

which represents the difference between the measured data  $y$  and forward model calculated data  $f(x)$ . The goal of inverse problem is to find  $x$  which minimize the objective function  $\Psi$ . Because the problem is ill-posed, it must be regularized,  $\alpha$  is a regularization parameter, and  $II$  presents prior information. Usually an initial guess of  $x$  is given and iterative process is conducted to update  $x$  until a satisfied  $\Psi$  is obtained (Figure 2-13). The iterative process can be made either by a Newton method such as the Levenberg-Marquardt algorithm (Schweiger et al., 1993 & 2005) or by a gradient method such as conjugate gradients (Arridge and Schweiger, 1998; Arridge et al., 1999).

This iterative method is first proposed by Schweiger (1993), since then a great effort have been done in develop fast, efficient, and stable methods for reconstruction. Schweiger et al. (1995) discussed the boundary and source condition. Jiang et al. (1996,

1998) solved 2-D inverse problems based on numerical simulations and phantom experiments, and solved an inverse problem with multi-target. Schweiger (2003), Dierkes (2005) and Dehghani (2004) established 3D breast models and reconstructed optical properties by the iterative nonlinear reconstruction procedure.

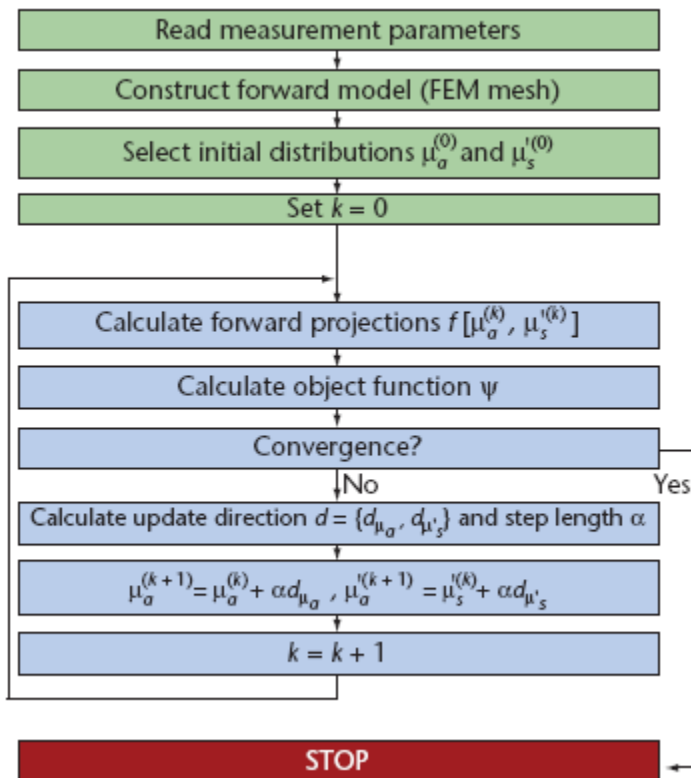


Figure 2-13 Schematic flow of iterative nonlinear reconstruction procedure

Source: Schweiger, M., Gibson, A., Arridge, A.R., 2003, "Computational aspects of diffuse optical tomography", *Computing in Science & Engineering*, **5**(6), 33-41.

## 2.4.5 Recent Advances in Diffuse Optical Imaging

### 2.4.5.1 Use of Prior Information

Because the inverse problem in DOT is a non-unique, ill-posed underdetermined problem, methods in Section 2.4.4.2 have shortcomings: unstable, time-consuming, low spatial resolution, requiring a lot of measurement data (Gibson et al., 2005). So in recent years, researchers use prior information to improve the image reconstruction. Niziachristos et al. (2000 & 2002), Schweiger et al. (2003), Brooksby et al. (2003 & 2005), Dehghani et al. (2009) used an MR image of a breast to provide the location of a tumor as a priori. Due to this approach, the spatial resolution of the optical image effectively becomes that of the MR image.

The prior information is applied in two levels: “hard priors” and “soft priors” (Brooksby, 2005). “Hard priors” are seeking parameter reduction. The target domain is divided into  $n$  regions and the homogeneous optical property is assumed in each region. Due to the small number of unknowns, the inverse problem is highly over-determined and therefore computationally fast and robust to noise in the data. Pogue and Paulsen (1998) described the use of high resolution MRI to improve simulated optical property reconstruction of a rat cranium. By accurately defining a region where heterogeneity is expected, they limit image property evolution to only those node locations.

“Soft priors” are seeking to improve regularization in iteration process. Li et al. (2003) use structural knowledge of the breast to define two discrete regions which they regularize differently in order to optimize NIR image contrasts. Figure 2-14 shows the results by implementing soft priors (Brooksby et al., 2005). The internal structure of a gelatin phantom is provided by MRI as a priori. The reconstructed images of the absorption and reduced scattering coefficients are improved by the use of the prior information.

In this thesis we have applied iterative nonlinear procedure to reconstruct optical properties and internal structure of breast is known by mammography as a prior to improve the reconstructed images.

Beside MRI, it is natural to consider combining optical imaging with X-ray mammography which could provide anatomical information to improve spatial resolution. Some preliminary results are obtained by Li et al. (2003) and Zhang et al. (2005).

Finally, there have been some attempts to combine optical imaging with ultrasound, either at the data acquisition stage by photoacoustics (Xu and Wang, 2006) or by modulating the light (Wang et al., 1995), or at the image reconstruction stage by using ultrasound to improve spatial localization (e.g. Zhu et al., 2008).

#### 2.4.5.2 Effect of Pressure

In optical tomography systems the human breast is usually compressed by flat glass plates or encircled by an array of fiber bundles. Pressure is applied to the exterior of the tissue, causing significant deformation in many cases (Ntziachristos et al., 2000). Pressure-induced changes in tissue properties have been observed in both *in vitro* (Chan et al., 1996; Changguan et al., 1998) and *in vivo* (Jiang et al., 2003; Cheng et al., 2003; Carp et al., 2006 & 2008; Boverman et al., 2007; Wang et al., 2008) biological tissue models. For example, clinical experiments by Jiang et al. (2003) are done in a group of five normal women aged 41-71 years. The result is shown in Figure 2-15, where the open symbols are phantom data and the filled symbols are human data; the circles represent measurements during closing of the array (increasing pressure) and the triangles represents measurements acquired during reopening of the array (decreasing pressure). It is shown that although little change occurred in phantom, pressure have significant impact on absorption and scattering coefficients on human tissue. Absorption coefficient decreases from 0.0056 to 0.0043 mm<sup>-1</sup> when pressure increased gradually from zero to

1100 Pa and then increases gradually to  $0.0063 \text{ mm}^{-1}$  as the pressure decreased back to 0 Pa. The scattering coefficient increased gradually from 1.0 to  $1.7 \text{ mm}^{-1}$  as the pressure increased and decreased gradually back to  $1.0 \text{ mm}^{-1}$  when pressure decreased to baseline.

This change could be explained that blood and water concentrations in breast tissue are variable when pressure applied. Thus the optical properties changes as applied pressure changes. So it indicates that pressure-induced changes must be considered when optical properties are estimated in human tissues.

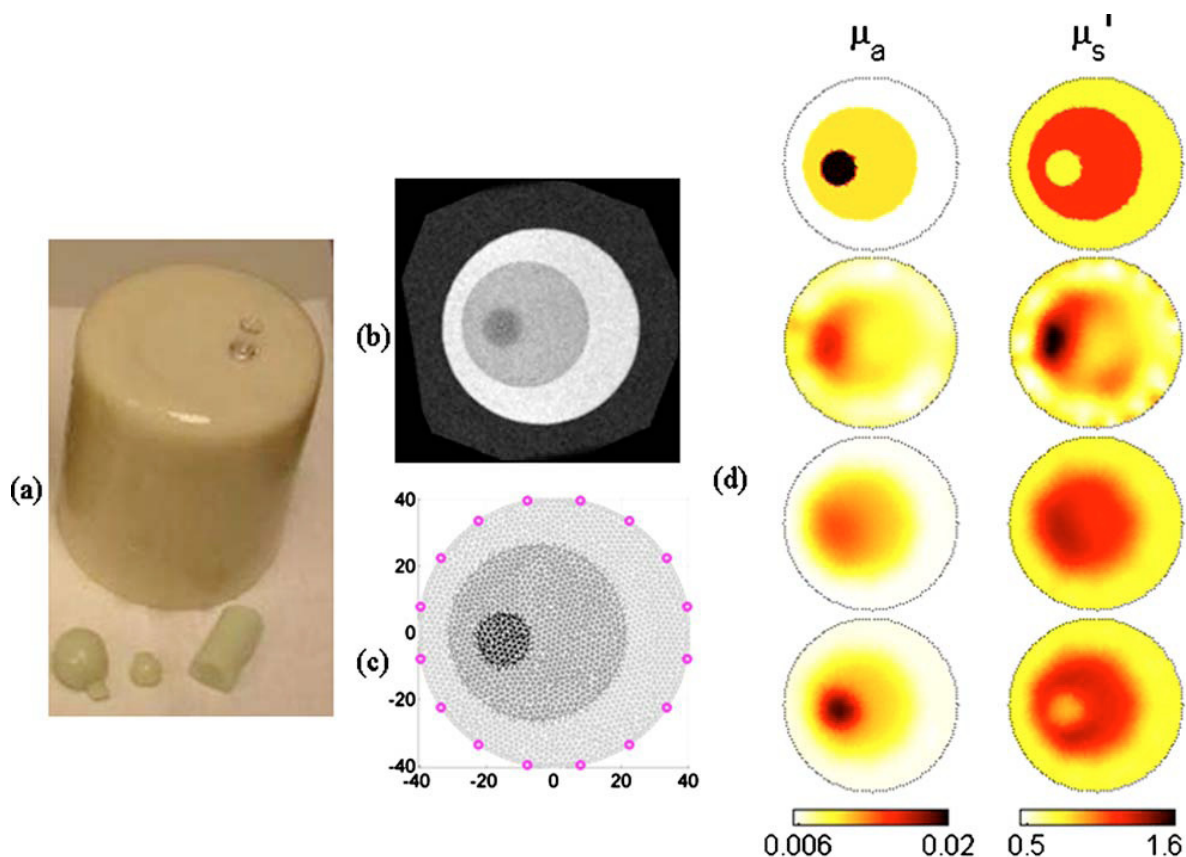


Figure 2-14 Use of prior information.

Source: Brooksby B., 2005, "Combining near infrared tomography and magnetic resonance imaging to improve breast tissue chromophore and scattering assessment", Ph.D. Thesis, Dartmouth College, Hanover, New Hampshire

Note: (a) Photograph of a gelatin phantom and a variety of inclusions (small gelatin spheres and a cylinder with different optical properties); (b) MRI showing a cross section of the cylindrical phantom, visible in the MRI are three types of gel; and (c) finite element mesh segmented according to the MRI intensity. The optical fiber source/detectors marked around the circumference are specified with millimeter accuracy. (d) Reconstructed images of the absorption and reduced scattering coefficient for this phantom. The top pair of images shows the true distribution, the second pair shows the reconstructions that do not use a prior information, the third pair shows reconstruction in which two layers were assumed from the MRI (i.e., the inclusion was ignored), and the bottom pair shows reconstructions in which the full MRI is used.

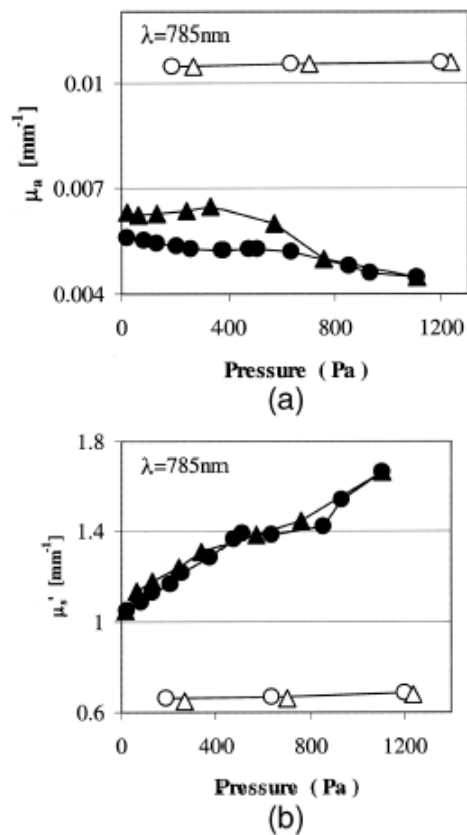


Figure 2-15. Typical absorption coefficient (a) and scattering coefficient (b) changes with applied pressure from a human subject and elastic phantom.

Source: Jiang, S.D., Pogue, B.W., Paulsen, K.D., 2003, "In vivo near-infrared spectral detection of pressure-induced changes in breast tissue", *Optics letters*, **28** (14), 1212-1214.

Note: In both (a) and (b) the open symbols are phantom data and the filled symbols are human data. The circles represent measurements during increasing pressure, and the triangles represent measurements during decreasing pressure.

## CHAPTER 3 LINEAR ELASTO-MAMMOGRAPHY

### 3.1 Introduction

Breast cancer is one of the major threats to public health in the world. Currently, X-ray mammography is the primary method for early detection and characterization of breast cancers, but it is not quite specific in terms of tumor benignity and malignancy. Although elastography has been developed to solve the problems associated with mammography, the application of elastography is limited by low penetration depth, high cost and low resolution.

The objective of this chapter is to develop a new imaging modality, called elasto-mammography, for quantification of the elastic modulus of normal and cancerous breast tissues. Instead of using ultrasound and magnetic resonance like in previous elastography, elasto-mammography method generates the elastograms of breast tissue by combining the conventional low-dose X-ray mammography with elastography framework. The displacement information is extracted from mammography projections before and after breast compression. Incorporating the displacement measurement, an elastography reconstruction algorithm is specifically developed to estimate the elastic modulus of heterogeneous breast tissue. Specifically, by adopting certain anatomically well-motivated assumptions, the geometry of tumors is estimated from the mammography projections, as well as the displacements at key points

This chapter is organized as follows: In Section 3.2, we present the optimization-based algorithm for elastography reconstructions. In Section 3.3 we further present elasto-mammography simulations using numerical breast phantoms containing tumors in. Then we investigate the influences of various errors with the measurements, including noise with displacements, geometric mismatch, and elastic contrast ratios in Section 3.4. Conclusions are drawn in the last section.



### 3.2 Methodology of Elastography Reconstruction

#### 3.2.1 Governing Equations and Finite Element Method

Under static loading, the deformation of tissues is governed by equations of equilibrium, strain-displacement, and a material constitutive law. The equilibrium equation is:

$$\frac{\partial \sigma_{i1}}{\partial x_1} + \frac{\partial \sigma_{i2}}{\partial x_2} + \frac{\partial \sigma_{i3}}{\partial x_3} + f_i = 0 \quad (3.1)$$

where  $i=1,2,3$ , the  $\sigma_{ij}$  denotes the stress tensor components and  $f_i$  represents the body forces. The strain-displacement relationship could be expressed as:

$$\varepsilon_{ij} = \frac{1}{2} \left( \frac{\partial u_i}{\partial x_j} + \frac{\partial u_j}{\partial x_i} \right) \quad (3.2)$$

where  $u_i$  is a component of the displacement vector  $\mathbf{u}=(u_1, u_2, u_3)$  in Cartesian coordinates  $\mathbf{x}=(x_1, x_2, x_3)$ . In this chapter, we focus on isotropic and linear elastic material (The case about anisotropic and nonlinear elastic material is given in Chapter 4: Nonlinear Elastography). Material constitutive law relates the strains and stresses as follows:

$$\sigma_{ij} = \frac{E}{1+\nu} \left( \varepsilon_{ij} + \frac{\nu}{(1-2\nu)} \delta_{ij} \varepsilon_{kk} \right) \quad (3.3)$$

where  $E$  and  $\nu$  represent Young's modulus and Poisson's ratio and  $\delta_{ij}$  is the Kronecker delta.  $E$  and  $\nu$  are related to Lamé parameters  $\lambda$  and  $\mu$ :

$$\lambda = \frac{E\nu}{(1+\nu)(1-2\nu)} \quad (3.4)$$

$$\mu = \frac{E}{2(1+\nu)} \quad (3.5)$$

If Lamé parameters and external loading are known, we could calculate displacements and subsequently strains and stresses by governing equations (3.1)~(3.3).

It is called forward problem. Inversely, if the external loading and displacements are measured, the distributions of Lamé parameters  $\lambda$  and  $\mu$  could be reconstructed. It is called inverse problem. The goal of elastography is to solve the inverse problem, that is, the external loadings and displacements are given, the distributions of elastic parameters are reconstructed.

Since there is no analytic solutions for equation (3.1)~(3.3), particularly in 3-D case with complex geometries, we use finite element method (FEM) in this study. FEM is a numerical technique which gives approximate solutions to differential equations. It is especially powerful when dealing with boundary conditions defined over complex geometries that are common in practical applications. In this method, the domain is first discretized into a number of simpler domains called elements. An approximate solution is assumed over an element in terms of solutions at selected points called nodes through interpolation. Using an approximation, the governing equations yield a small set of linear equations for each element called the element stiffness equation. The elements' stiffness equations are calculated and then assembled to form a linear system of equations called the global stiffness equation (Zienkiewicz et al., 2000; Bhatti, 2005)

$$\mathbf{K}\mathbf{u} = \mathbf{F} \quad (3.6)$$

where  $\mathbf{K}$ , global stiffness matrix, is real, symmetric and quasi-positive definite, and depends only on the Lamé parameters  $\lambda$  and  $\mu$ ,  $\mathbf{u}$  is unknown displacement vector and  $\mathbf{F}$  is force vector.

### 3.2.2 Objective Function

Typical clinical mammography applies compression on the breast so that the maximum amount of tissues can be imaged and examined from different view angles. Under a compression, information about the displacements can be *measured* from projective images. If the elastic modulus distribution is given, displacements can also be *calculated* by Equation (3.6). The objective of elastography problem is to optimally find

the elastic modulus distribution that minimizes the difference between the measured displacements in the biomedical medium of interest and the calculated displacements that depends on the elastic modulus distribution.

Denoting the *measured* displacement field in the biomedical medium of interest ( $\Omega$ ) as  $U(\mathbf{x})$ , and the *calculated* displacement field associated with the trial distribution of Lamé parameters  $\lambda(\mathbf{x})$  and  $\mu(\mathbf{x})$  as  $\mathbf{u}(\mathbf{x})$ , the elasto-mammography seeks Lamé parameters such that the following objective functional  $\Phi(\lambda(\mathbf{x}), \mu(\mathbf{x}))$  is optimally minimized:

$$\Phi(\lambda(\mathbf{x}), \mu(\mathbf{x})) = \int_{\Omega} (\mathbf{u}(\mathbf{x}) - U(\mathbf{x})) \cdot \chi(\mathbf{x}) \cdot (\mathbf{u}(\mathbf{x}) - U(\mathbf{x})) dV \quad (3.7)$$

where the second-order tensor  $\chi$  simply takes diagonal matrix form, i.e.,  $(\chi(\mathbf{x}))_{ij} = \delta_{ij} \omega_i(\mathbf{x})$  ( $i, j = 1, 2, 3$ ). The weight function  $\omega_i(\mathbf{x})$  equals zero if the  $i$ -th displacement component is *not* measured at point  $\mathbf{x}$ . To include the surface displacement as measurement,  $\omega_i(\mathbf{x})$  is considered as a generalized function on the boundary of  $\Omega$ .

The elasto-mammography reconstruction follows an iterative optimization procedure, as schematically shown in Figure 3-1. The initial estimate for distribution of Lamé parameters  $(\lambda, \mu)$  is given. Displacements can be calculated by Equation (3.6) and objective function is obtained by comparing measured and calculated displacements. Then Lamé parameters are updated for next iteration until a satisfied objective function is obtained.

### 3.2.3 Adjoint Method

The iterative optimization procedure usually requests user-supplied gradient. The previous elastography studies used direct or approximate finite-different method (Smani et al., 2001; Han et al., 1993) for the gradient calculation. The computation expense of these methods increases proportionally with the number of material parameters. Recently an adjoint method was introduced to compute the gradient analytically (Tardieu et al.,

2000; Oberai et al., 2003; Liu et al., 2005 & 2006). Oberai et al. (2003) adopted the adjoint method and proposed a numerical scheme for reconstructing the nonuniform shear modulus field for incompressible isotropic material using one component of displacement field. Liu et al. (2006) applied this method for anisotropic materials. In this thesis we applied this method for proposed linear elasto-mammography. The basic algorithm is recalled for linear isotropic material in this chapter and we expand it to nonlinear material in next chapter.

Stiffness equation (3.6) can be rearranged, without affecting the solution, as

$$\begin{bmatrix} K_{11} & K_{12} \\ K_{12}^T & K_{22} \end{bmatrix} \begin{Bmatrix} u_1 \\ u_2 \end{Bmatrix} = \begin{Bmatrix} F_1 \\ F_2 \end{Bmatrix} \quad (3.8)$$

where  $u_2$  corresponds to the prescribed displacements on the boundary  $\partial\Omega_u$ , i.e.  $u_2 = U$ , and  $F_1$  the given nodal forces.  $u_1$  and  $F_2$  stand for the unknown nodal displacements and forces. Note that measurement of displacements  $U$  should only taken on the nodes where the displacements are not prescribed. That is,  $U$  is only measured on the nodes associated with  $u_1$ .

The objective function (3.7) then becomes:

$$\Phi(\lambda(x), \mu(x)) = (u - U)^T X (u - U) \quad (3.9)$$

in which the matrix  $X$  corresponds to the weight function  $\chi(x)$ , and has the same dimension as the stiffness matrix  $K$ , but is diagonal, and  $X_{ii}$  equals to zero when the  $i$ -th component in  $u$  is not measured.

We defined the adjoint displacements  $w$  as:

$$\{w\} = \begin{Bmatrix} w_1 \\ w_2 \end{Bmatrix} = \begin{Bmatrix} w_1 \\ 0 \end{Bmatrix} \quad (3.10)$$

in which vector  $w_1$  has the same dimension as  $u_1$ , and  $w_2 = 0$  is because of the prescribed boundary condition  $w = 0$  on  $\partial\Omega_u$ . The weak form of stiffness equation (3.6) could be expressed as

$$w^T(Ku - F) = 0 \quad (3.11)$$

for arbitrary choice of  $w_1$ . We introduce equation (3.11) into objective function (3.9) and obtain a Lagrangian:

$$L(\lambda(x), \mu(x), u, w) = (u - U)^T X(u - U) + w^T(Ku - F) \quad (3.12)$$

It can be shown that  $\Phi(\lambda(x), \mu(x)) = L(\lambda(x), \mu(x), u, w)$  and  $\delta\Phi = \delta L$  when Equation (3.11) is satisfied for arbitrary  $w_1$ . The variation  $\delta L$  can be expressed as

$$\delta L = \delta u X(u - U) + (u - U)^T X \delta u + w^T(\delta K u + K \delta u) \quad (3.13)$$

$$\delta L = 2(u - U)^T X \delta u + w^T(\delta K u + K \delta u) \quad (3.14)$$

$$\delta L = (2(u - U)^T X + w^T K) \delta u + w^T \delta K u \quad (3.15)$$

Let  $2(u - U)^T X + w^T K = 0$ , Equation (3.15) becomes:

$$\delta L = u^T \delta K w \quad (3.16)$$

So we have

$$\delta\Phi = u^T \delta K w \quad (3.17)$$

where  $\delta K$  is due to the change of Lamé parameters  $\lambda$  and  $\mu$ , displacement vector  $u$  is associate with current value of Lamé parameters  $\lambda$  and  $\mu$  and is solved from finite element equation (3.8). The adjoint displacement vector  $w$  is resulted from the difference between the calculated and measured displacement, i.e. it satisfied

$$Kw = -2X(u - U) \quad (3.18)$$

Above formulas focus for one measurement, but typical clinical mammography applies  $M$  ( $M \geq 2$ ) individual compressions on the breast so that the maximum amount of tissues can be imaged and examined from different view angles. The displacement and force quantities with the  $i$ -th experiment are denoted with superscript “ $(i)$ ”. Denoting for the  $i$ -th loading the measured displacement vector as  $U^{(i)}$ , and the *calculated* displacement vector as  $u^{(i)}$ . The objective function (3.9) and gradient (3.17) become:

$$\Phi(\lambda(x), \mu(x)) = \sum_{i=1}^M (u^{(i)} - U^{(i)})^T X^{(i)} (u^{(i)} - U^{(i)}) \quad (3.19)$$

$$\delta\Phi = \sum_{i=1}^M (u^{(i)})^T \delta K w^{(i)} \quad (3.20)$$

where  $u^{(i)}$  and  $w^{(i)}$  satisfy

$$\begin{bmatrix} K_{11}^{(i)} & K_{12}^{(i)} \\ K_{12}^{(i)T} & K_{22}^{(i)} \end{bmatrix} \begin{Bmatrix} u_1^{(i)} \\ u_2^{(i)} \end{Bmatrix} = \begin{Bmatrix} F_1^{(i)} \\ F_2^{(i)} \end{Bmatrix} \quad (3.21)$$

and

$$\begin{bmatrix} K_{11}^{(i)} & K_{12}^{(i)} \\ K_{12}^{(i)T} & K_{22}^{(i)} \end{bmatrix} \begin{Bmatrix} w_1^{(i)} \\ w_2^{(i)} \end{Bmatrix} = -2X^{(i)} (u^{(i)} - U^{(i)}) \quad (3.22)$$

In the proposed elasto-mammography technique, anatomic structures of the normal breast tissue and tumor are pre-scanned. Therefore the breast can be modeled as a piece-wise homogeneous medium, with uniform Lamé parameters  $(\lambda_{\text{tissue}}, \mu_{\text{tissue}})$  for normal breast tissue region and uniform parameters  $(\lambda_{\text{tumor}}, \mu_{\text{tumor}})$  for the tumor region. Consequently, there are four gradients to be calculated:

$$\frac{\partial\Phi}{\partial\lambda_{\text{tissue}}} = \sum_{i=1}^M (u^{(i)})^T \frac{\partial K}{\partial\lambda_{\text{tissue}}} w^{(i)} \quad (3.23)$$

$$\frac{\partial\Phi}{\partial\mu_{\text{tissue}}} = \sum_{i=1}^M (u^{(i)})^T \frac{\partial K}{\partial\mu_{\text{tissue}}} w^{(i)} \quad (3.24)$$

$$\frac{\partial\Phi}{\partial\lambda_{\text{tumor}}} = \sum_{i=1}^M (u^{(i)})^T \frac{\partial K}{\partial\lambda_{\text{tumor}}} w^{(i)} \quad (3.25)$$

$$\frac{\partial\Phi}{\partial\mu_{\text{tumor}}} = \sum_{i=1}^M (u^{(i)})^T \frac{\partial K}{\partial\mu_{\text{tumor}}} w^{(i)} \quad (3.26)$$

Favorable feature of the adjoint method is the minimum consumption for calculating the gradients. The adjoint method is to solve adjoint displacements  $w$  during each of iteration in Equation (3.18), instead of the whole stiffness matrix  $K$  that increases the numerical efficiency significantly. By comparing Equation (3.8) and (3.18),

it can be shown that the real displacements  $u$  and the adjoint displacements  $w$  share the same stiffness matrix  $K$  and its Cholesky factorization for the finite element computation (Press et al., 1996). Because computation for stiffness matrix  $K$  and its Cholesky factorization takes most of the time consumed in the finite element method, solving Equation (3.18) for adjoint displacement  $w$  and further calculating  $\delta\Phi$  (Equation (3.17)) are expected to add a small fraction of time in addition to the solution for displacement  $u$ , which is anyway required in an optimization-based numerical scheme for an inverse problem. Oberai et al. (2004) compared three different iterative methods: (1) A gradient-based method where the adjoint approach is used to calculate the gradient; (2) A gradient-based method where the straightforward approach is used to calculate the gradient and (3) the Gauss-Newton method (Doyley et al., 2000). The results are shown in Table 3-1. The results show that “leading-order costs for the gradient-based method with the adjoint approach are smaller than the other two methods”. In this chapter we recall the adjoint method for linear material and we will extend it to nonlinear material and finite-strain deformation in chapter 4.

Table 3-1 Estimate of leading-order computational costs per iteration for various iterative method, where  $N$  is the number of unknown material parameters

	Gaussian elimination (two dimension)	Gaussian elimination (three dimension)
Gradient-based (adjoint approach)	$O(N^2)$	$O(N^{7/3})$
Gradient-based (straightforward approach)	$O(N^{5/2})$	$O(N^{8/3})$
Gauss-Newton	$O(N^3)$	$O(N^3)$

Source: Oberai, A.A., Gokhale, N.H., Doyley, M.M., Bamver, J.C., 2004, “Evaluation of the adjoint equation based algorithm for elasticity imaging”, *Physics in Medicine and Biology*, **49**(13), 2955-2974

### 3.2.4 Optimization-based Reconstruction Procedure

The reconstruction frame involved data acquisition, material modeling, and reconstruction of material parameters, shown with the flowchart in Figure 3-1. The data acquisition includes establishing finite-element model for breast, measuring displacements by mammography projections. Material modeling includes initial estimation for distribution of Lamé parameters  $\lambda$  and  $\mu$ . The reconstruction procedure is optimization-based, making use of a limited-memory BFGS (L-BFGS) optimization subroutine (Liu et al., 1989), for which user-supplied gradients are required. When solving displacement  $u$  with finite-element method, the factorization of stiffness matrix  $K$  is stored at each time step, and is used for the adjoint displacement  $w$ . Once initial guesses of distribution of Lamé parameters  $\lambda$  and  $\mu$  is given, displacements are calculated in forward problem. The calculated and measured displacements are used to form objective function (3.19). Gradients are obtained by calculating adjoint displacement  $w$  and Lamé parameters are updated. New iteration is repeated until a satisfied objective function is obtained.

### 3.3. Numerical Simulations

In this section, simulations are performed with numerical breast phantoms to identify the elastic parameters for normal tissue and tumor(s). The three-dimensional (3-D) breast phantoms contain one and two tumors, respectively. To simulate mammography compression, two types of loadings are applied, respectively, on the phantoms from different loading angles. Surface forces and part of the boundary displacements are extracted from the forward computation results, in compliance with the capability of projective imaging, and are used as input for the reconstruction. The measured displacements are used to established objective function (3.19). In the following text, unit is “cm” for length and displacements, “kPa” for elastic moduli, and “kN” for nodal forces.



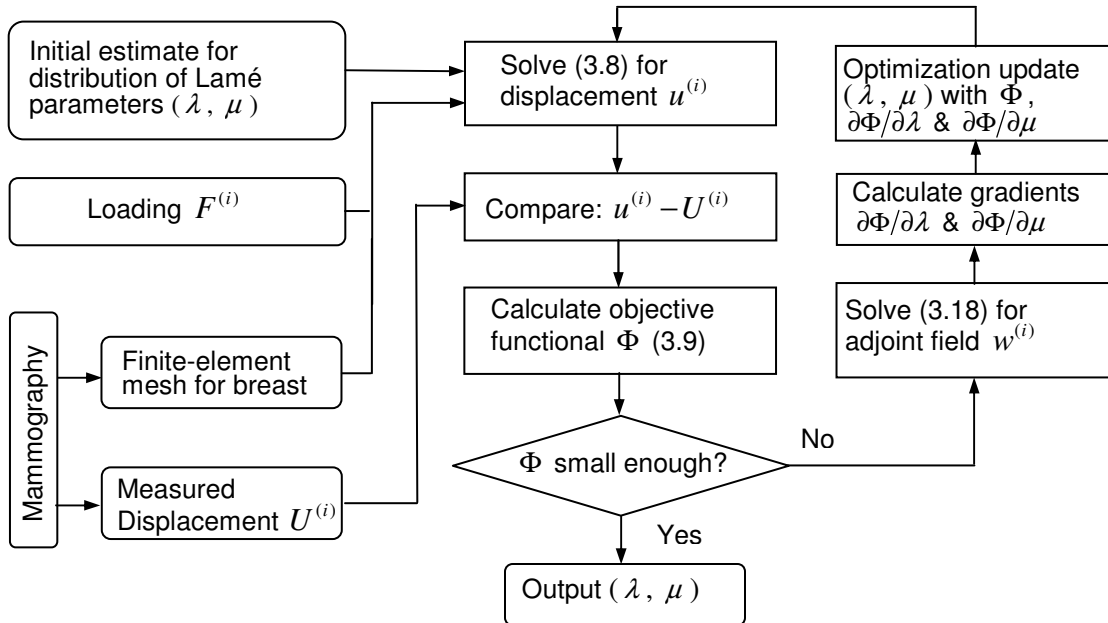


Figure 3-1 Overall flowchart for elasto-mammography reconstruction of Lamé parameters  $\lambda$  and  $\mu$  of breast tissues.

### 3.3.1 Forward Computations

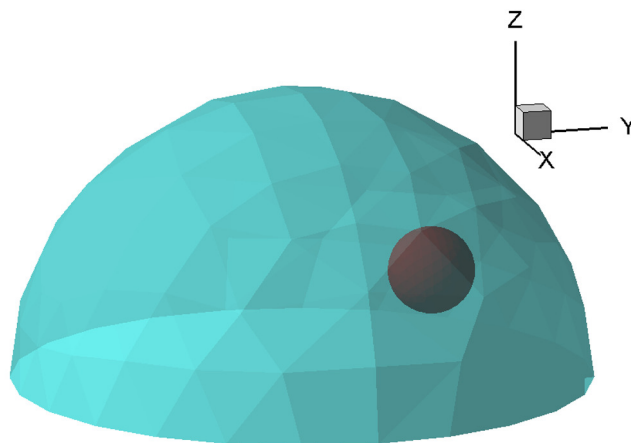
Let us first consider a 3-D phantom consisting of a half-spherical matrix with an embedded spherical inclusion (Figure 3-2 (a)). The soft matrix, 10 cm in diameter and center at  $(x, y, z)=(0, 0, 0)$ , imitates normal breast tissue. The hard inclusion, 1.5 cm in diameter and center at  $(2, 1.75, 2.25)$ , simulates a tumor. The second phantom (Figure 3-2 (b)) is similar, but has one more tumor of the same size and at  $(-1.8, 0, 2)$ . We denote these phantoms as “Phantom I” and “Phantom II”, respectively. The phantoms are discretized with standard 3-D tetrahedral elements. Phantom I consists of 1114 nodes and 6070 elements (2805 elements are in the inclusion), while Phantom II consists of 1657 nodes and 9340 elements (3969 elements are in the inclusions).

The materials are assumed isotropic. The Lamé parameters  $(\lambda, \mu)$  are  $(25, 7.5)$  for the soft breast tissue and  $(125, 25)$  for the tumor. The Young’s modulus  $E$  and the Poisson ratio  $\nu$  are related to Lamé parameters via

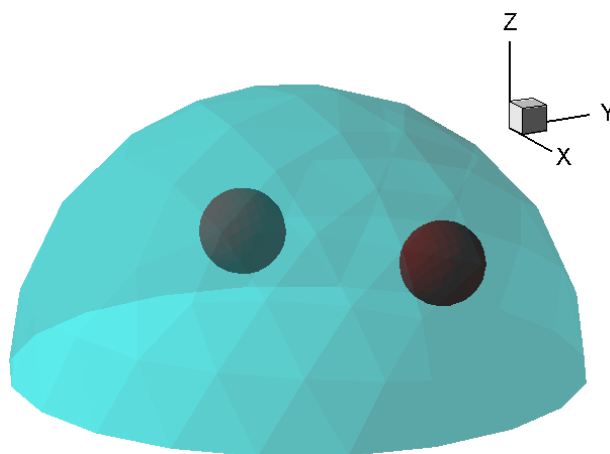
$$E = \frac{\mu(3\lambda + 2\mu)}{\lambda + \mu} \quad (3.27)$$

$$\nu = \frac{\lambda}{2(\lambda + \mu)} \quad (3.28)$$

Hence,  $(E, \nu)$  are  $(20.77, 0.39)$  for soft tissue and  $(70.83, 0.42)$  for tumor. Note that the tumor is assumed approximately 3.5 times as stiff as the surrounding tissue. In general, a tumor is much stiffer than the surrounding normal tissues. However, the ratio between the stiffness of cancerous and normal breast tissues found in the literature shows variations from a few times to a few ten times (Wellman, 1999). Skovoroda et al. (1995) recognized that this is partially due to the nonlinearity effect in which the apparent stiffness increases with the strain applied. Effects of the contrast ratio on elasto-mammography are discussed in Section 3.4.3.



(a) Phantom I with one tumor

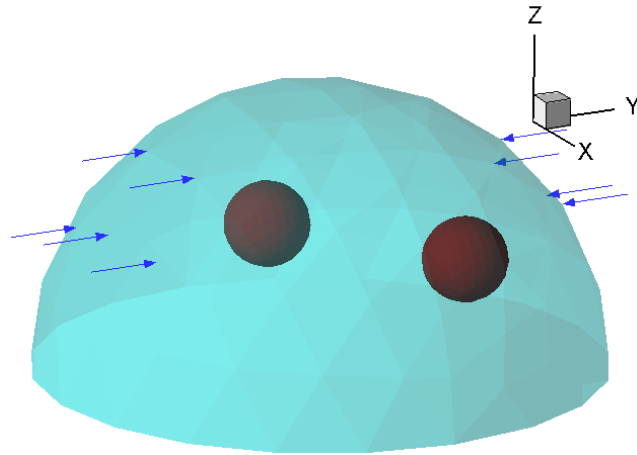


(b) Phantom II with two tumors.

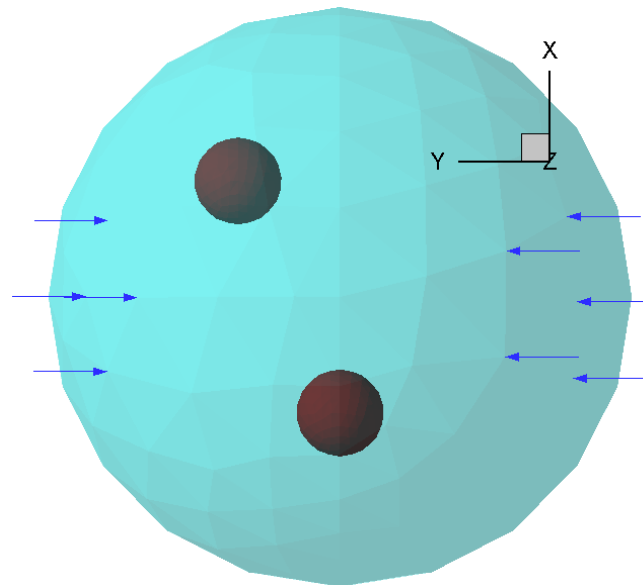
Figure 3-2 Three-dimensional phantoms mimicking the normal breast tissue and embedded tumor(s).

---

Note: Finite-element mesh is shown on the external surface. Phantom I consists of 1114 nodes and 6070 elements, while Phantom II consists of 1657 nodes and 9340 elements.

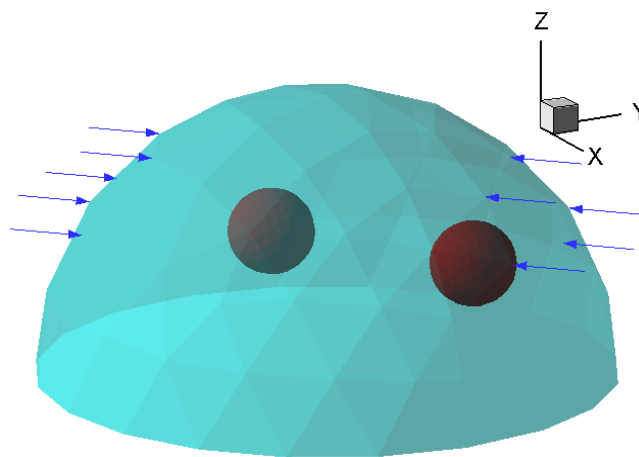


(a) Phantom II under loading 1 with 3-D view

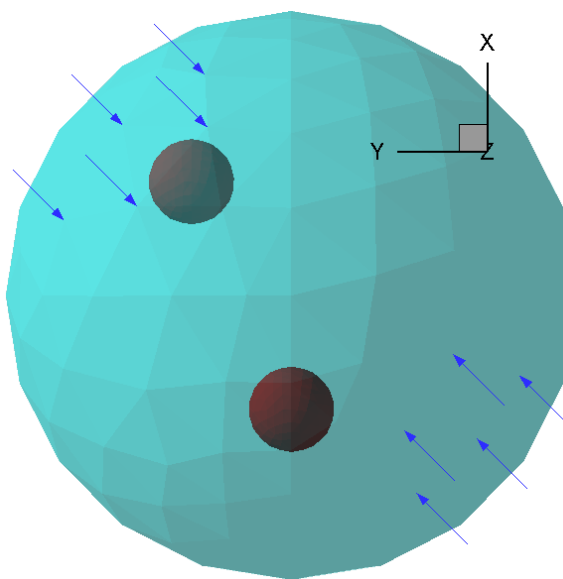


(b) Phantom II under loading 1 with x-y plane view to show direction 1

Figure 3-3 Loading 1, compression nodal force applied on the surface. Shown with Phantom II



(a) Phantom II under loading 2 with 3-D view



(b) Phantom II under loading 2 with x-y plane view to show direction 2

Figure 3-4 Loading 2, compression nodal force applied on the surface. Shown with Phantom II

In the simulations, the displacements are zero on the base surface where  $z = 0$ . Two compression loadings are applied on the upper surface of breast phantoms, respectively. For Loading 1, nodal force of 0.005 kN is applied on some of the surface nodes, as Figure 3-3 plotted with Phantom II. Loading 2 applies nodal force  $|F_x| = |F_y| = 0.004$  kN on the other set of surface nodes, as shown in Figure 3-4. Note that the loading directions are different by  $\pi/4$ . For convenience, we denote the direction with Loading 1 as “direction 1”, and that with Loading 2 as “direction 2”.

### 3.3.2 Data Acquisition

Given the Lamé parameters for normal breast tissue and tumor(s), the deformations in response to the external loadings 1 and 2 are obtained by solving Equation (3.8). First of all, the external surface of a breast at undeformed state can be reconstructed from images taken with a 3-D camera (e.g., Page et al. 2005). Then, for each external loading, two mammography projections are made in the compression direction; i.e., one projection with undeformed state, and another with deformed configuration. The shape and location of the tumor(s) can further be estimated from the undeformed projections along different orientations. It is recognized that real tumors may be irregular in shape and be difficult to reconstruct accurately with limited number of projections. As a first-order approximation, we assume that tumors are spherical initially, and deform into ellipsoids. The initial size and center of tumors are readily estimated with two undeformed projections made in different directions. For instance, directions 1 and 2 in the present simulation, as plotted with Figure 3-5 (a) and Figure 3-6 (a) for Phantom II. Note that Phantom I can be considered as Phantom II with absence of the tumor initially at  $(-1.8, 0, 2)$ .

We extract displacement information from projection of deformed configurations. Based on the micromechanics theory for deformation of an inclusion in a large medium (Eshelby, 1957), it is reasonable to estimate that an initially spherical tumor deforms into

an ellipsoid. Because of the relatively simple uniaxial compression loadings applied in mammography, it is further approximated that vertexes of an object in an undeformed projection remain vertexes in the corresponding projection after compression deformation. For example, in Figure 3-5 (b) for Loading 1, point A is the top vertex of tissue in undeformed projection. It moves to vertex A' after deformation. Points B~I are vertexes of the tumors in undeformed projection in direction 1. They move to vertexes B'~I', respectively. Thus, by measuring the vertex locations in projections before and after deformation, their displacement information can be obtained. For example, displacement components  $u_x$  and  $u_z$  in Loading 1 for vertexes A~I are extracted from the projections as in Figure 3-5. Acquisition of displacement information with Loading 2 makes use of projections Figure 3-6 (a) and (b), and follows the same procedure. It is noted that the two tumors partly overlap in the projections in direction 2, and vertexes C and G are in shadow. For such a case, the vertex displacements are still attainable, according to the grey density information in the projections with lose of some accuracy. The collected displacement data are denoted as  $U^{(1)}$  and  $U^{(2)}$  for elasto-mammography reconstruction.

Accurate displacement measurement with high spatial resolution will benefit elastography reconstruction in general. However, pinpoint tracking of large number of material points in an object is still a challenge in medical imaging (Hajnal et al., 2001), in particular for simple mammography projections that lack natural landmarks. Therefore, we propose elasto-mammography that only makes use of displacements of a few special points extracted directly from projections. As described above, the points include top vertex on the upper breast surface (A in Figure 3-5 (b)) and vertexes of the tumors in projections (B~I). Displacements measured at other points, for instance on the external surface with a 3-D camera, should enhance the efficiency and accuracy of elasto-mammography.

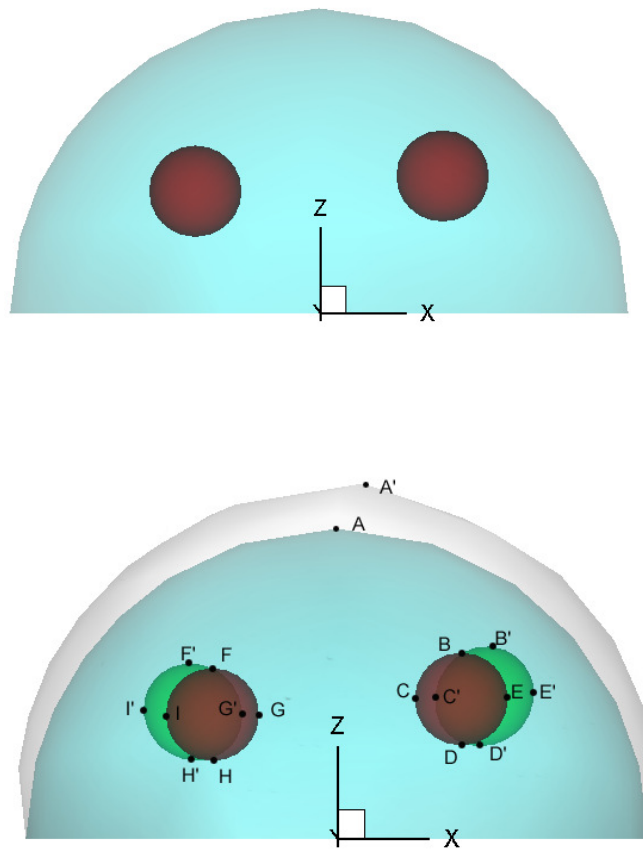


Figure 3-5 Mammography projections with Phantom II under loading 1.

Note: Projections are made in direction 1. (a) Undeformed projection; (b) Deformed projection overlaps on undeformed projection. In the projections, vertexes A ~ I in undeformed projection move to A' ~ I' in deformed projection, respectively.



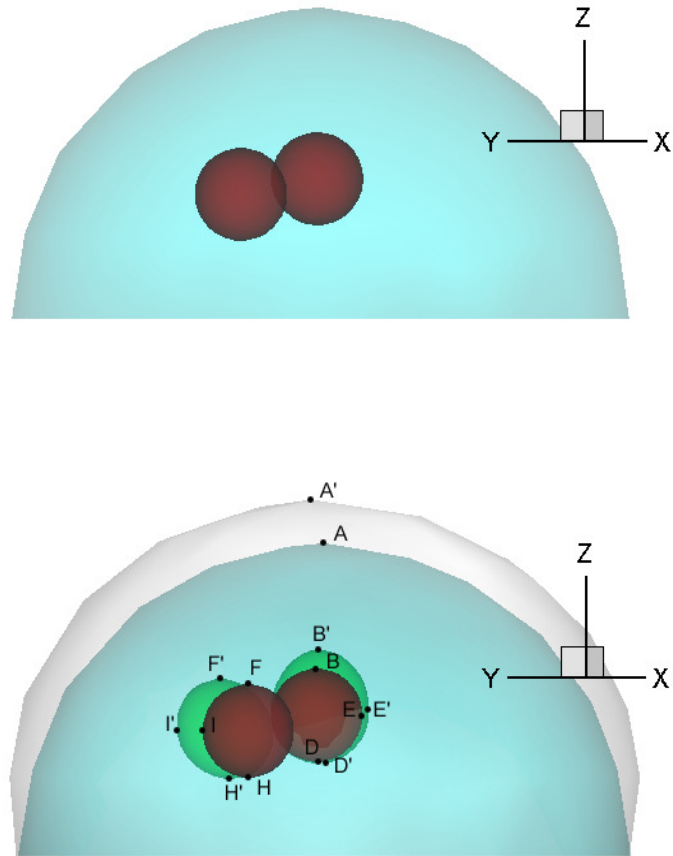


Figure 3-6 Mammography projections with Phantom II under loading 2.

Note: Projections are made along direction 2. (a) Undeformed projection; (b) Deformed projection overlaps on undeformed projection. In the projections, vertexes  $A \sim I$  in undeformed projection move to  $A' \sim I'$  in deformed projection, respectively.

### 3.3.3 Inverse Problem

With the described data acquisition method, displacements at some key points are extracted from deformed and undeformed projections with the two compression loadings, and are used as measurements  $U^{(1)}$  and  $U^{(2)}$  for elasto-mammography reconstruction. Compression nodal forces applied on the surface are also known with the loadings. Given initial estimate, the Lamé parameters for tissue and tumor are reconstructed following our optimization procedure (Figure 3-1).

Ideal case is considered first; i.e., the displacements, geometry and compression nodal forces are exactly measured, and are used as input for reconstruction. Rows “Ideal I” and “Ideal II” of Table 3-1 give the reconstruction results with Phantom I and Phantom II, respectively. All parameters are accurately identified, with the largest error of about  $\pm 0.18\%$  (for  $\lambda$  of tumor). Reconstructions using different initial estimates have been conducted. Very similar convergent profiles are found for the parameters, and highly accurate results are obtained. This indicates efficiency and uniqueness of the proposed elasto-mammography using projective measurements.

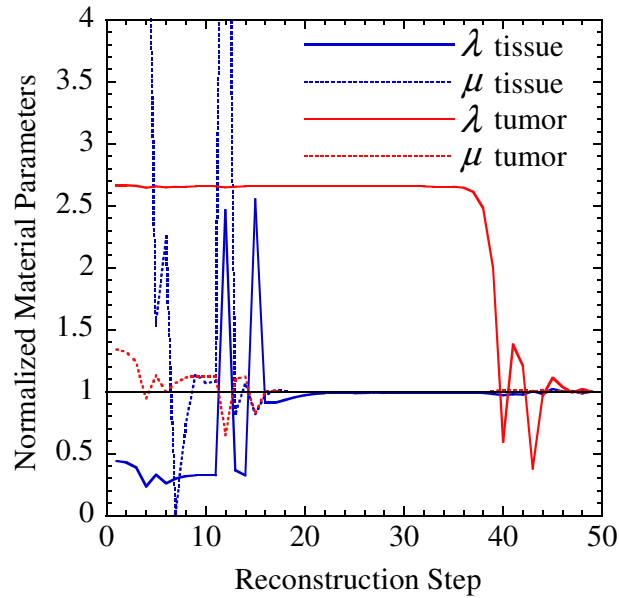
Although all parameter reach real values ultimately, the convergent speeds are quite different. Convergent loci of the Lamé parameters  $(\lambda, \mu)$  are plotted with Figure 3-7. The loci for Phantom I (Figure 3-7(a)) and Phantom II (Figure 3-7 (b)) are very similar. It is observed that  $(\lambda, \mu)$  of the tissue approach the real value rapidly. After about 20 iteration steps, their relative errors are well within the range of 5%. Then they experience some minor adjustment. In contrast, Lamé parameters of the tumor converge slower, in particular for  $\lambda$ , which starts to fall to the real value after about 40 steps. After about 50 steps, it reaches the real value.

The slower convergent speed of Lamé parameters of the tumor, in particular for  $\lambda$ , is explained by the roles they play in the deformation due to the applied loadings, as discussed in Liu et al. (2005). In general, parameters with the most significant influence

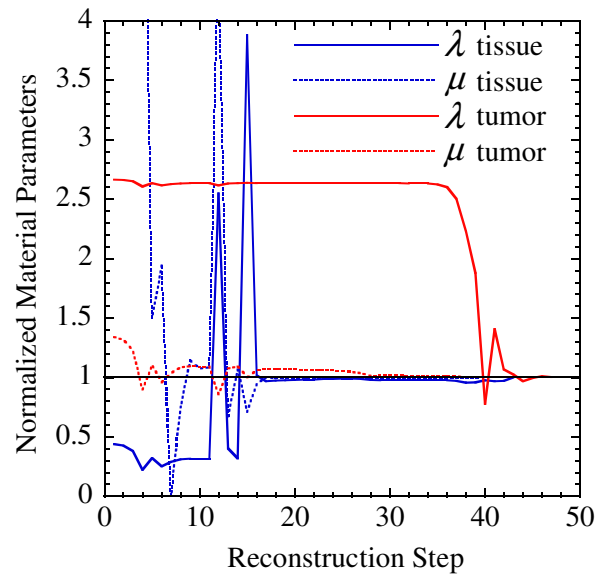
on the deformation are also those that are most accurately and easily identified. The influence of a parameter depends on size and location of the material region it belongs to, as well as characteristics of the deformation. For the present simulations,  $\lambda$  and  $\mu$  of the tissue are dominant, while those of tumor are much less influential, due to the small size and deep location of the tumor(s). Slower convergence of  $\lambda$  for tumor indicates that the present loadings do not introduce enough volumetric strain in the tumor. The loading should be close to tumors in order to make tumors have larger deformation. A well-designed loading that provide more stress-strain information will improve the convergent speed of Lamé parameters of the tumor.

Table 3-2 Initial estimate and reconstructed results for linear elasto-mammography

	Tissue				Tumor			
	$\lambda$	$\mu$	$E$	$\nu$	$\lambda$	$\mu$	$E$	$\nu$
Real	25	7.5	20.77	0.39	125	25	70.83	0.42
Estimate	11	194.5	399.44	0.03	333	33.5	97.71	0.45
Reconstruction Results								
Ideal I	24.99	7.5	20.77	0.39	124.81	25.00	70.82	0.42
Ideal II	25.01	7.5	20.76	0.39	125.21	25.03	70.95	0.42
Noise I	25.15	7.50	20.76	0.39	106.75	25.06	70.40	0.41
Noise II	26.04	7.50	20.82	0.39	146.80	22.38	64.18	0.43
Mismatch	24.97	7.50	20.78	0.38	129.39	24.90	70.93	0.42
Mismatch	25.04	7.49	20.70	0.39	155.27	26.94	78.83	0.46



(a)



(b)

Figure 3-7 Convergent loci of elasto-mammography reconstruction for Lamé parameters  $(\lambda, \mu)$  of normal breast tissue and tumor, normalized with the exact values correspondingly.

Note: No measurement error is considered. (a) Phantom I with one tumor; (b) Phantom II with two tumors.

### 3.4 Discussion

#### 3.4.1 Effect of Noise

The above elasto-mammography reconstructions are conducted using ideal inputs. In practice, several factors will affect the performance of elasto-mammography, the most common one among which is the noise with displacement measurement. To investigate the capability of the proposed elasto-mammography modality and algorithm to handle imperfect real data due to inevitable measurement errors, we conduct reconstruction using noisy input; i.e., each component of  $U^{(1)}$  and  $U^{(2)}$  is added with a randomly selected relative error in  $(-5\%, 5\%)$ .

The results are shown as “Noise I” (for Phantom I) and “Noise II” (for Phantom II) at Table 3-1 and the convergent loci are plotted with Figure 3-8. The overall convergent loci are very similar to the “ideal” cases. Lamé parameters  $(\lambda, \mu)$  of the tissue need about 20 steps to approach closely to the real values, while those of the tumor needs about 50 steps for convergence. The tissue parameters are very accurately identified, with the largest relative error of 4% for  $\lambda$  of Phantom II, and errors are within  $\pm 1\%$  for the others. The Lamé parameters  $(\lambda, \mu)$  for tumors, however, are not as robust, with relative errors of  $(-14.6\%, 0.22\%)$  and  $(17.4\%, -15.5\%)$  for Phantom I and Phantom II, respectively. In spite of these reconstruction errors, it is still positive that the elasto-mammography results are accurate enough for diagnosis of tumors, noting the significant differences of stiffness between normal tissue, benign and malignant tumors (Sarvazyan et al., 1995; Wellman et al., 1999; Skovoroda et al., 1995). The better robustness of the tissue parameters is also explained by the strong roles they play in the deformation, as we have discussed in section 3.3.3. Furthermore, as suggested by Liu et al. (2005), multiple sets of well-designed loadings should help to bring out the influences of all the material parameters, and thus suppress the effects of noise.

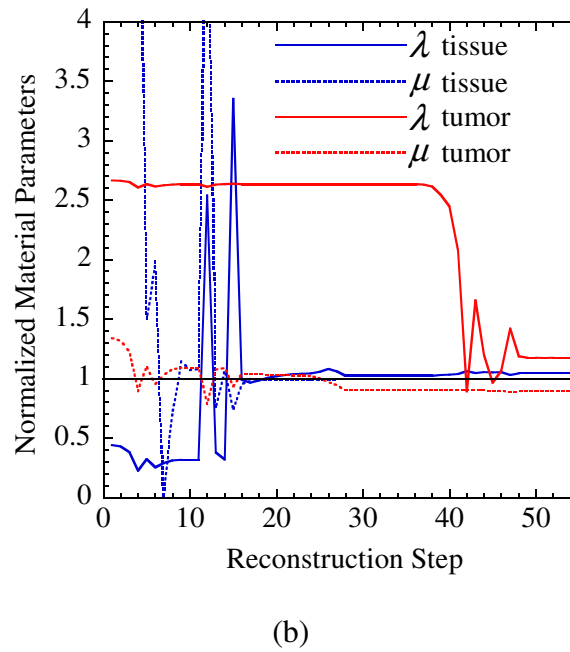
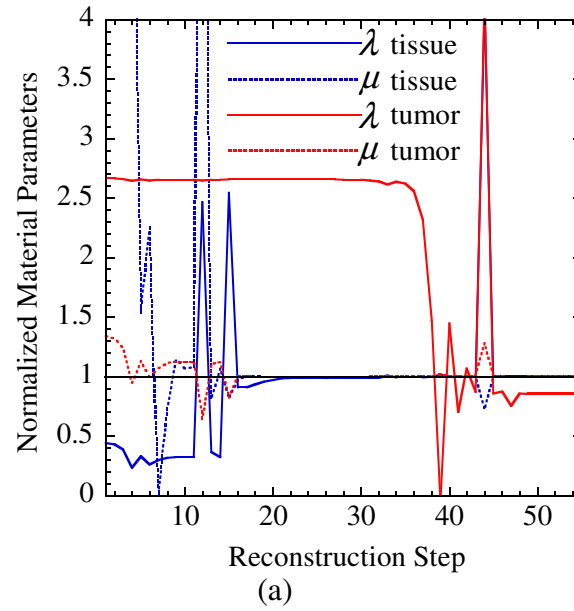


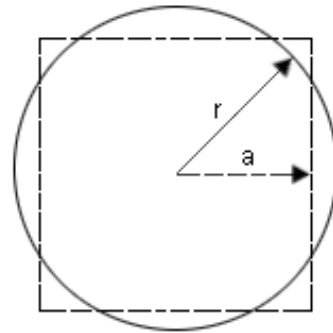
Figure 3-8 Convergent loci of elasto-mammography reconstruction for Lamé parameters ( $\lambda$ ,  $\mu$ ) of normal breast tissue and tumor, normalized with the real values correspondingly. Noise is considered.

Note: (a) Phantom I with one tumor; (b) Phantom II with two tumors.

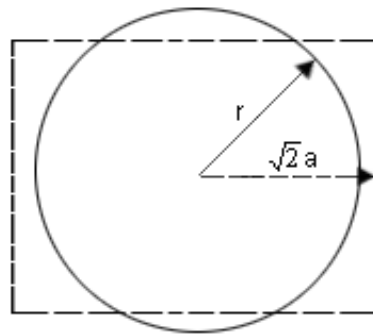
### 3.4.2 Effect of Geometry Mismatch

Another concern for elasto-mammography is the geometric depiction of the tumor. As described in the section of data acquisition, we use a simple sphere to approximate a real tumor, and estimate its size and location from two undeformed mammography projections. This inevitably introduces geometric mismatch for practical elasto-mammography. To investigate the effect of geometry mismatch, the two phantoms are re-designed by replacing the spherical tumors with cubic tumors. Note that the edge length of the cube is  $3/\sqrt{5}$  cm. Forward simulations are conducted under the same Loading 1 and Loading 2 with the new phantoms. Then, mammography projections are made of the new undeformed and deformed configurations. To extract geometric and displacement data from the projections, we still used spherical approach. As schematically shown in Figure 3-9, a cubic tumor is approximated with a spherical one, whose size and location are determined by the two undeformed projections in direction 1 and direction 2. Then, the estimated spherical tumors are used for elasto-mammography reconstruction of the material parameters. The results are shown as “Mismatch I” (for Phantom I) and “Mismatch II” (for Phantom II) in Table 3-1. Convergent loci are found to be similar to the previous cases, and are not shown.

The tissue parameters again show excellent robustness. The geometric mismatch introduces relative errors less than 0.17% . Due to the relatively small size of the tumor(s), their Lamé parameters ( $\lambda, \mu$ ) are more sensitive to geometric mismatch, with relative errors (3.52%, 0.40%) for Phantom I and (24.2%, 7.78%) for Phantom II. In comparison to the displacement noise, the geometry mismatch seems to have slightly less overall influence on the reconstruction results. However, this point is based on the current phantoms, and needs further investigation.



(a)



(b)

Figure 3-9. Geometry mismatch.

---

Note: A sphere is used to approximate a real cubic tumor. Size and location of the sphere are determined from projections of the cubic tumor in direction 1 (a) and direction 2 (b).  $r/a = \sqrt{5}/2$ .



### 3.4.3 Effect of Contrast Ratio

The material stiffness is a key feature that distinguishes benign from malignant tumors (Wellman et al., 1999; Skovoroda et al., 1995; Ophir et al., 1991). Contrast ratio, defined as the ratio of Young's modulus of tumor to normal breast tissue, covers a wide range. For benign tumors, contrast ratio typically varies from 2.0 to about 5.0. For malignant tumors, it is considerably higher. The numerical experiments (Liu et al., 2005) indicate that accuracy of elastography reconstruction depends not only on type of loading and measurement accuracy, but also on the contrast ratio. For case that the tumor is very hard, the material parameters may be identified qualitatively, but not quantitatively.

To investigate the effect of contrast ratio, we conducted elasto-mammography reconstructions with soft and hard phantoms, whose Lamé parameters ( $\lambda, \mu$ ) are set to create contrast ratio (CR) of 1.5 and 8.0, respectively. Table 3-2 gives the real Lamé parameters and reconstruction results. Comparing with the previous case with CR about 3.5 (Table 3-1, "Ideal I" and "Ideal II"), results for the soft phantoms (CR=1.5) are even more accurate, in particular for  $\lambda$  of the tumor. For the hard phantoms (CR=8.0), the tissue parameters are also exact; however,  $\lambda$  of tumor carries relative errors of about 13% for both phantoms, which is considerably larger than the soft cases with CR=3.5 and 1.5. The reason is that deformation of a relatively softer tumor is larger than a hard one, and thus is more sensitive to small variation of its material parameters. Also as discussed above,  $\lambda$  of the tumor seems to have the least influence on the specific deformations considered in the simulations. On the other hand, it is convincing that the proposed elasto-mammography is efficient to reveal the contrast ratio, and tell whether a tumor is malignant or benign. In general, a tumor is suspected of malignancy when the contrast ratio is higher than 6. In the present simulations, when the "real" contrast ratio is 8.0, the elasto-mammography reconstruction yields 8.11, which is fully acceptable for the diagnostic purpose.

Table 3-3 Elasto-mammography simulation using phantoms with different stiffness contract ratio

	Tissue				Tumor			
	$\lambda$	$\mu$	$E$	$\nu$	$\lambda$	$\mu$	$E$	$\nu$
Contrast Ratio=1.5								
Real	25	7.5	20.77	0.39	54.98	11.00	31.15	0.42
Phantom I	25	7.5	20.77	0.39	54.98	11.00	31.15	0.42
Phantom II	24.93	7.5	20.77	0.38	55.71	11.03	31.15	0.42
Contrast Ratio=8.0								
Real	25	7.5	20.77	0.39	293.22	58.64	166.15	0.42
Phantom I	24.99	7.5	20.77	0.39	332.56	58.68	167.23	0.43
Phantom II	24.99	7.5	20.76	0.39	331.42	59.12	168.42	0.42

#### 3.4.4 Uniqueness and Multiple Measurements

A general mathematical proof for uniqueness results of elastography have not reported. Some researches have shown that the uniqueness of the solution depends on the boundary conditions. For instance, it is known that, for plane strain problems with prescribed displacement boundary conditions, a single measured displacement field is not sufficient to ensure uniqueness (Barbone et al., 2002 & 2004). In plane stress, on the other hand, a single displacement field is sufficient to determine the shear modulus in an incompressible material.

For clinical application, Barbone et al., (2004) demonstrated the feasibility of using multiple displacement fields to reduce the likelihood of nonuniqueness for 2-D isotropic elastography. Then Liu et al. (2005) discussed the multiple sets of measurements in 3-D anisotropic media. The tumor and normal breast tissue were assumed as general anisotropic materials, and four sets of loadings were applied on a

breast phantom to bring out all the elastic parameters. Their isotropic simulation suggested that displacements measured from a single loading are adequate for unique identification of the Lamé parameters ( $\lambda, \mu$ ) of tissue and tumor. However, their measurement includes displacement on the entire external surface and the tissue-tumor interface of a breast, requiring more complex imaging equipment. In our proposed elasto-mammography, displacement measurement is obtained only on a few vertices from simple mammography projections. A tradeoff is that two or more sets of compression loadings may be needed to obtain adequate information.

The key point from using multiple sets of measurements is to bring more deformation modes simultaneously into consideration. The loadings should be close to tumors in order to make tumors have larger deformation. It is shown in Figure 3-7 and 3-8 that the convergent speed of Lamé parameters of the tumor is slower than these of the normal tissue. Well-designed loadings that provide more stress-strain information will improve the convergent speed of Lamé parameters of the tumor.

Mathematical proof for uniqueness results of elasto-mammography using projection measurements is yet under further investigation. Our simulations always yield the same material parameters (within the numerical processing errors), regardless of the initial estimate. With ideal measurements, the resulting parameters exactly match the real values specified for the models. When displacement noise and geometry mismatch are taken into consideration, the resulting parameters have reconstruction errors, however, reconstructed parameters are close enough to their real values for application purpose. In summary, the proposed elasto-mammography method is numerically stable and robust, relatively simple to perform, and thus has great potential for clinical applications.

### 3.5. Conclusions

A new imaging modality framework, called elasto-mammography, is proposed to generate the elastograms of breast tissue based on conventional X-ray mammography.

Displacement and geometry measured from mammography projections before and after breast compressions are applied as input data to reconstruct the isotropic material parameters for normal breast tissue and tumor. Case studies with numerical breast phantoms are conducted to demonstrate the capability of the proposed elastomammography. Effects of noise with measurement, geometric mismatch, and elastic contrast ratio are evaluated in the numerical simulations. It is shown that the proposed methodology is stable and robust for characterization of the elastic moduli of breast tissues from the projective displacement measurement.

## CHAPTER 4 NONLINEAR ELASTOGRAPHY

### 4.1 Introduction

Current elastography reconstruction frameworks are based on infinitesimal-strain linear elastic deformation theory, and only very few have considered large deformation, nonlinear and anisotropic behaviors of breast tissues and tumor. It is shown, however, that the deformation of most biological soft tissues is not linear elastic (Wellman et al., 1999). Developing a nonlinear model is essential for elastography in clinical applications.

In this chapter, an elastography method for reconstruction of nonlinear breast tissue properties is developed. In Section 4.2, we present an algorithm based on finite-strain deformation theory, instead of infinitesimal-strain theory. The iterative Newton method is applied to solve unknown displacements and forces. In order to find elastic modulus distribution that minimizes the objective function based on measured and calculated forces, the adjoint gradient method is employed to provide user-supplied gradients in nonlinear elastography. In last chapter, the adjoint method is introduced in linear elasto-mammography. Here we first develop a nonlinear adjoint method that significantly improves the numerical efficiency and enhance the stability of elastography reconstruction. Numerical simulation is described in Section 4.3 including establishing a three-dimensional (3-D) heterogeneous finite element method (FEM) breast phantom and applying exponential-form nonlinear material model. Four types of compressive loadings are applied in the forward problem. The iterative reconstruction based on force measurements on surface is also detailed. In Section 4.4, the result of the inverse problem is obtained and the effect of noise is investigated. A user-defined penalty function is introduced to reduce the impact of noise on reconstruction. Conclusions are drawn in the last section.

## 4.2 Methodology of Nonlinear Elastography

### 4.2.1 Finite-Strain Deformation Equations

We use continuum description for the breast tissues (Gurtin 1981). Let  $\Omega^0$  be a biological object. From the displacement tensor  $\mathbf{u}(\mathbf{X})$  based on Lagrangian coordinate system  $\mathbf{X}$ , the deformation gradient is

$$\mathbf{F} = \mathbf{I} + \partial\mathbf{u}/\partial\mathbf{X} \quad (4.1)$$

and the Green strain is

$$\mathbf{E} = (\mathbf{F}^T \cdot \mathbf{F} - \mathbf{I})/2 \quad (4.2)$$

where “ $\cdot$ ” denotes the contraction operation between two tensors.

The breast tissues are assumed hyperelastic so that the second Piola-Kirchhoff stress is

$$\mathbf{S} = \partial W(\mathbf{E}; \mathbf{p})/\partial \mathbf{E} \quad (4.3)$$

where  $W$  is the strain energy and  $\mathbf{p}$  denotes material parameters in the model. We use “;” to separate material parameters from deformation variables (Fung, 1993).

The governing equation and boundary conditions for  $\mathbf{u}$  are

$$\begin{cases} \nabla \cdot (\mathbf{S} \cdot \mathbf{F}^T) + \mathbf{b}(\mathbf{X}, \mathbf{u}(\mathbf{X})) = \mathbf{0} & \mathbf{X} \in \Omega^0 \\ \mathbf{N}(\mathbf{X}) \cdot (\mathbf{S} \cdot \mathbf{F}^T) = \mathbf{t}(\mathbf{X}, \mathbf{u}(\mathbf{X})) & \mathbf{X} \in \Gamma_t^0 \\ \mathbf{u}(\mathbf{X}) = \bar{\mathbf{u}}(\mathbf{X}) & \mathbf{X} \in \Gamma_u^0 \end{cases} \quad (4.4)$$

The boundary of  $\Omega^0$  consists of  $\Gamma_t^0$ , with  $\mathbf{N}$  the outer normal, on which external force  $\mathbf{t}$  is applied, and  $\Gamma_u^0$  where displacement  $\bar{\mathbf{u}}$  is prescribed. Here, we consider general problems that the body force  $\mathbf{b}$  and surface force  $\mathbf{t}$  are deformation dependent. Following the standard finite element method (Belytschko et al., 2000; Oden, 1972; Bhatti, 2005), the displacement  $\mathbf{u}$  is discretized as nodal displacement vector  $\{u\} = \{u_1, u_2\}^T$ , where  $u_2$  corresponds to  $\bar{\mathbf{u}}$  prescribed on  $\Gamma_u^0$ , and  $u_1$  is to be solved from nonlinear equations:

$$\begin{Bmatrix} f_1^{\text{in}}(u_1, u_2; \mathbf{p}) \\ f_2^{\text{in}}(u_1, u_2; \mathbf{p}) \end{Bmatrix} - \begin{Bmatrix} f_1^{\text{out}}(u_1, u_2) \\ f_2^{\text{out}} \end{Bmatrix} = \begin{Bmatrix} 0 \\ 0 \end{Bmatrix}. \quad (4.5)$$

The internal nodal force  $f^{\text{in}}$  corresponds to stress  $\mathbf{S}$ ; i.e., it changes with  $u_1$  and material parameters  $\mathbf{p}$ , as  $u_2$  is given. The external nodal force  $f_1^{\text{out}}$  is due to the prescribed surface force  $\mathbf{t}$  on  $\Gamma_t^0$  and body force  $\mathbf{b}$  in  $\Omega^0$ . It varies with the displacement in large deformation. The nodal force  $f_2^{\text{out}}$  is the unknown constraint force on  $\Gamma_u^0$ .

A classic Quasi-Newton method (Press et al., 1996) is employed to solve Equation (4.5) for  $u_1$ . Let  $u_1^{(n)}$  be the trial solution of the unknown  $u_1$  at the  $n$ -th iterative step. An improved solution  $u_1^{(n+1)} = u_1^{(n)} + \delta u_1$  can be obtained at the next step, in which  $\delta u_1$  is the solution of linear equations:

$$K_{\text{eff}}^{(n)} \delta u_1 = f_1^{\text{out}}(u_1^{(n)}, u_2) - f_1^{\text{in}}(u_1^{(n)}, u_2; \mathbf{p}) \quad (4.6)$$

where

$$K_{\text{eff}}^{(n)} = \left. \frac{\partial (f_1^{\text{in}} - f_1^{\text{out}})}{\partial u_1} \right|_{u_1 = u_1^{(n)}} \quad (4.7)$$

The iteration is put into effect until the residue  $\|f_1^{\text{out}} - f_1^{\text{in}}\|$  is smaller than the preset criterion.

#### 4.2.2 Objective Function

Experimental measurements for elastography include displacement and force. We consider that the biological object  $\Omega^0$  is discretized into FE mesh, and the measurements are discretized consistently into nodal displacement and nodal force. We catalog the measurements as the following:

(i) If the displacement at a node is known (prescribed or measured after deformation), it will be included into  $u_2$  which is considered “prescribed” in Equation (4.5). The corresponding nodal force (known or unknown) will be in the constraint force, denoted as  $F_2^M$ . Note that  $F_2^M$  corresponds to  $f_2^{\text{out}}$  in Equation (4.5).

(ii) All the other nodal displacements will be in  $u_1$  and the corresponding nodal force will be in  $f_1^{\text{out}}$ . For category (ii),  $f_1^{\text{out}}$  must be considered “prescribed” to fulfill the requirement of the well-posedness of a solid-mechanics problem.

For elastography problem, the obtained  $u_2$  and  $f_1^{\text{out}}$  are known in Equation (4.5), and the constraint force  $F_2^M$  is considered as “measurement”. For given material parameter  $\mathbf{p}$ , the unknown displacement  $u_1$  and constraint force  $f_2^{\text{out}}$  (which depends on  $\mathbf{p}$ ) will be solved from Equation (4.5). Elastography procedure thus searches for  $\mathbf{p}$  so that the overall difference between measured  $F_2^M$  and computed  $f_2^{\text{out}}$  is minimum, that is, minimize objective function

$$\Phi(\mathbf{p}) = (f_2^{\text{out}} - F_2^M)^T \Lambda (f_2^{\text{out}} - F_2^M) \quad (4.8)$$

where the diagonal weight matrix  $\Lambda = \text{diag}(a_1, a_2, \dots, a_j, \dots)$ . The component  $a_j = 1$  when the  $j$ -th component of  $F_2^M$  is measured or  $a_j = 0$  otherwise. The present algorithm is mathematically equivalent to one in Chapter 3 for linear elasto-mammography where the displacement is used as “measurement”. For breast tissue whose tangent stiffness significantly increases with strain, this “force version” shows better numerical efficiency.

#### 4.2.3 Nonlinear Adjoint Method

Efficient and robust optimization-based elastography schemes request user-supplied gradient  $\partial\Phi/\partial\mathbf{p}$ . The previous elastography studies used direct or approximate finite-difference method for the gradient calculation (Smani et al., 2001; Han et al., 1993). The computational expense of these methods increases proportionally with the number of material parameters, and becomes unaffordable for problems involving finite-strain deformation. Recently an adjoint method was introduced to compute the gradient analytically (Tardieu et al., 2000; Oberai et al., 2003; Liu et al., 2005 & 2006). In Chapter 3 we recalled this method for linear elasto-mammography. Here we first develop nonlinear adjoint method for finite-strain deformation.



The goal of the adjoint method is to calculate the gradient  $\partial\Phi/\partial\mathbf{p}$  efficiently. We introduce the constraint Equation (4.5) into the objective function Equation (4.8), and obtain a Lagrangian:

$$L(u_1, \mathbf{p}) = (f_2^{out} - F_2^M)^T \Lambda ((f_2^{out} - F_2^M)) + \begin{Bmatrix} w_1 \\ w_2 \end{Bmatrix}^T \begin{Bmatrix} \delta f_1^{in} - \delta f_1^{out} \\ \delta f_2^{in} - \delta f_2^{out} \end{Bmatrix} \quad (4.9)$$

where  $w_1$  and  $w_2$  are arbitrary virtual displacements. It is noted that variables  $u_1$  and  $\mathbf{p}$  are no longer coupled. It is also noted that  $\Phi = L$  and  $\delta\Phi = \delta L$  under the constraint Equation (4.5). Since the equality constraint Equation (4.5) is satisfied with  $u_1$ , the variation  $\delta L$  can be expressed as

$$\delta L = \left( 2(f_2^{out} - F_2^M)^T \Lambda - w_2^T \right) (\delta f_2^{out}) + w_1^T (\delta f_1^{in} - \delta f_1^{out}) + w_2^T \delta f_2^{in} \quad (4.10)$$

It can be simplified by setting the arbitrary virtual displacement  $w_2$  as

$$w_2 = 2\Lambda (f_2^{out} - F_2^M) \quad (4.11)$$

so that

$$\delta L = w_1^T (\delta f_1^{in} - \delta f_1^{out}) + w_2^T \delta f_2^{in} \quad (4.12)$$

Consider that  $u_1$  and  $\mathbf{p}$  are independent in  $L$  and that the external force term  $f_1^{out}$  should not explicitly depend on the material parameter  $\mathbf{p}$  and  $\Delta u_2 = 0$ , Equation (4.12) becomes

$$\delta L = \left( w_1^T \frac{\partial (f_1^{in} - f_1^{out})}{\partial u_1} + w_2^T \frac{\partial f_2^{in}}{\partial u_1} \right) \delta u_1 + \left( w_1^T \frac{\partial f_1^{in}}{\partial \mathbf{p}} + w_2^T \frac{\partial f_2^{in}}{\partial \mathbf{p}} \right) \delta \mathbf{p} \quad (4.13)$$

If we choose  $w_1$  as the solution of

$$w_1^T \frac{\partial (f_1^{in} - f_1^{out})}{\partial u_1} + w_2^T \frac{\partial f_2^{in}}{\partial u_1} = 0 \quad (4.14)$$

only one term remains, i.e.,

$$\delta L = \left( w_1^T \frac{\partial f_1^{in}}{\partial \mathbf{p}} + w_2^T \frac{\partial f_2^{in}}{\partial \mathbf{p}} \right) \delta \mathbf{p} \quad (4.15)$$

Since  $\delta\Phi = \delta\mathcal{L}$ , the gradient is readily obtained as:

$$\frac{\partial\Phi}{\partial\mathbf{p}} = \begin{Bmatrix} w_1 \\ w_2 \end{Bmatrix}^T \begin{Bmatrix} \partial f_1^{in} / \partial \mathbf{p} \\ \partial f_2^{in} / \partial \mathbf{p} \end{Bmatrix} \quad (4.16)$$

where the adjoint displacements  $w_1$  and  $w_2$  are solved from linear equations

$$w_2 = 2\Lambda(f_2^{out} - F_2^M) \quad (4.17)$$

$$(K_{eff})^T w_1 = -\left(\frac{\partial f_2^{in}}{\partial u_1}\right)^T w_2 \quad (4.18)$$

where  $K_{eff} = \partial(f_1^{in} - f_1^{out}) / \partial u_1$  is defined in Equation (4.7).

The most significant features of the adjoint method are its analytical formulation, high accuracy, and computational efficiency (Liu et al., 2006). By introducing the adjoint method, it seems that more equations and variables ( $w_1$  and  $w_2$ ) need to be solved. But the solution of Equation (4.17) and (4.18) is straightforward and computational cost is minimized because  $K_{eff}$  has been computed and factorized when solving for the displacement  $u_1$  as in Equation (4.6). Furthermore, it only needs to solve linear Equation (4.17) and (4.18) regardless of the number of unknown parameters in  $\mathbf{p}$ . More details are discussed in Section 4.4.3.

#### 4.2.4 Optimization-based Reconstruction Procedure

The reconstruction frame involved data acquisition, material modeling, and reconstruction of material parameters, shown with the flowchart in Figure 4-1. The data acquisition includes establishing finite element model for breast, measuring displacements and forces. It is well known that the mechanical behavior of biological soft tissue is nonlinear. In this chapter we apply hyperelastic model to represent the stress-strain relation of breast tissue and tumor. We denote the material parameters  $\mathbf{p} = \{\lambda, \mu, \gamma\}$ . More details are given in Section 4.3.1. The reconstruction procedure is optimization-based, making use of a limited-memory BFGS (L-BFGS) optimization

subroutine (Liu et al., 1989), for which user-supplied gradients are required. Once initial guesses of distribution of material parameters  $\{\lambda, \mu, \gamma\}$  are given, displacements and forces are calculated in forward problem. The calculated and measured forces are used to form objective function (4.8). Gradients are obtained by calculating adjoint displacement  $w$  and material parameters are updated. The iteration is put into effect until the objective function is smaller than the preset criterion.

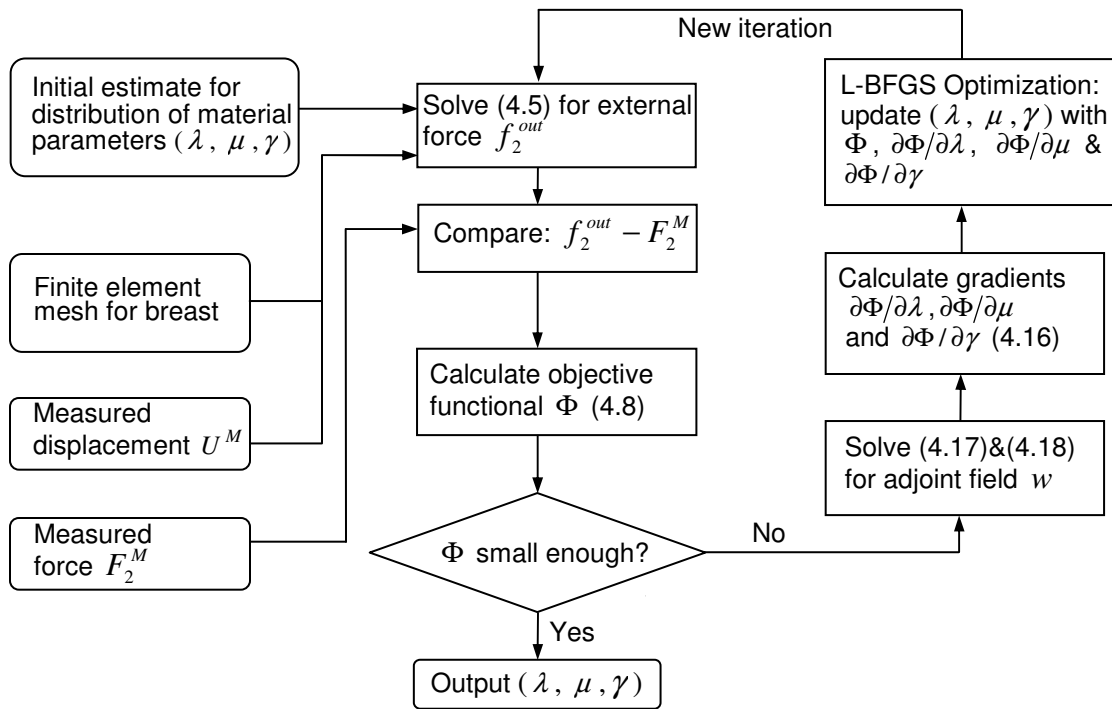


Figure 4-1 Overall flowchart for reconstruction of material parameters  $\lambda$ ,  $\mu$  and  $\gamma$  in nonlinear elastography.

### 4.3 Numerical Simulations

This section presents phantom simulations to identify the nonlinear elastic properties of the fatty, glandular and cancerous tissues in a breast. First of all, a 3-D breast FEM phantom attracting from the real data is introduced. Then Fung's model (Fung, 1993) is applied to describe the deformation of breast tissues. With the applied loading, the forward-problem computation is performed. Furthermore, boundary forces are extracted from the forward computation results and are used as input for reconstruction for nonlinear breast tissue properties.

#### 4.3.1 Breast Phantom

To perform numerical simulations, a 3-D numerical heterogeneous breast phantom extracting from real CT images, containing fatty tissue, glandular tissue and a tumor is established (Figure 4-2). Boundaries of these regions are described with sets of splines. The phantom is discretized with standard 3-D tetrahedral elements, consisting of 1835 nodes and 8115 elements, in which 2958 elements are in fatty tissue, 5081 elements are in glandular tissue and 76 elements are in the tumor (Figure 4-3).

In previous elastography research, in order to simplify the model, it is usually assumed that breast tissue is linear elastic. However, it is well known that most of biological soft tissues exhibit a nonlinear mechanical response (Fung, 1993). While tissue models based on linear elasticity have been broadly used, they are reliable only where tissue deformation is limited to small strain values of less than 5% (O'Hagan, 2008). For most clinical application for mammography or elastography, breast tissue undergoes large deformation. In this chapter we apply a nonlinear model to simulate the deformation of breast tissues and tumors.

Hyperelastic models have commonly been applied to describe the finite strain deformation and highly nonlinear mechanical properties of biological soft tissue (Zulliger et al., 2004). Among them is the classical work of Fung and his coworkers (Fung, 1993).

In this work, I employed a Y.C. Fung-type isotropic constitutive model for the breast tissues and tumor, whose strain energy function reads

$$W(\mathbf{E}; \mathbf{p}) = \gamma(\exp Q - 1) = \gamma(\exp[\lambda(\mathbf{E} : \mathbf{I})^2 / 2 + \mu \mathbf{E} : \mathbf{E}] - 1) \quad (4.19)$$

where  $Q(\mathbf{E}) = \lambda(\mathbf{E} : \mathbf{I})^2 / 2 + \mu \mathbf{E} : \mathbf{E}$ ,  $\mathbf{E}$  is the Green strain, and  $\mathbf{p} = \{\lambda, \mu, \gamma\}$  denotes the material parameters. The second Piola-Kirchhoff stress  $\mathbf{S}$  can thus be derived as:

$$\mathbf{S} = \partial W / \partial \mathbf{E} = \gamma \exp Q [\lambda(\mathbf{E} : \mathbf{I}) \mathbf{I} + 2\mu \mathbf{E}] \quad (4.20)$$

Specifically, in uniaxial tension/compression, the relation between the axial strain  $E$  and axial stress  $S$  is simplified as:

$$S = \gamma \exp\left(\frac{\kappa E^2}{2}\right) \kappa E \quad (4.21)$$

where  $\kappa = \mu(3\lambda + 2\mu) / (\lambda + \mu)$ , and  $\gamma$  (with the unit of stress, kPa),  $\lambda$  (dimensionless), and  $\mu$  (dimensionless) are material parameters.

Equation (4.21) is the exponentially nonlinear model that can be applied for breast tissues. Three parameters  $\gamma$ ,  $\lambda$  and  $\mu$  can be determined by the experiment (Samani 2004). Wellman (1999) developed a technique to measure the nonlinear elastic parameters of breast tissues using force-displacement data of thin slice tissue undergoing indentation experiment. The tissue samples tested were obtained during surgery and were tested immediately after removal from the body. Six breast tissues (fatty tissue, glandular tissue, lobular carcinoma, fibroadenoma, infiltrating ductal carcinoma, and ductal carcinoma in situ) were tested in uniaxial tension. The stress-strain data were fitting with Equation (4.21) and the results are plotted in Figure 4-4, where lobular carcinoma and fibroadenoma are benign tumors; infiltrating ductal carcinoma, ductal carcinoma in situ are malignant tumors. It is shown that the mechanical properties between normal soft breast tissue and tumors are quite different. Tumors are stiffer than the surrounding breast tissues and malignant tumors are much stiffer than benign ones.

In the following example study, the material parameters of ‘ductal carcinoma in situ’ (Wellman, 1999) are assigned to the tumor, as  $\lambda_d = 80$ ,  $\mu_d = 35$ ,  $\gamma_d = 1.5$  ( $\lambda$  and  $\mu$  are dimensionless,  $\gamma$  is in kPa). The parameters for fatty tissue are  $\lambda_f = 35$ ,  $\mu_f = 12.5$ ,  $\gamma_f = 0.4$ , and for glandular tissue are  $\lambda_g = 50$ ,  $\mu_g = 25$ ,  $\gamma_g = 0.25$ .

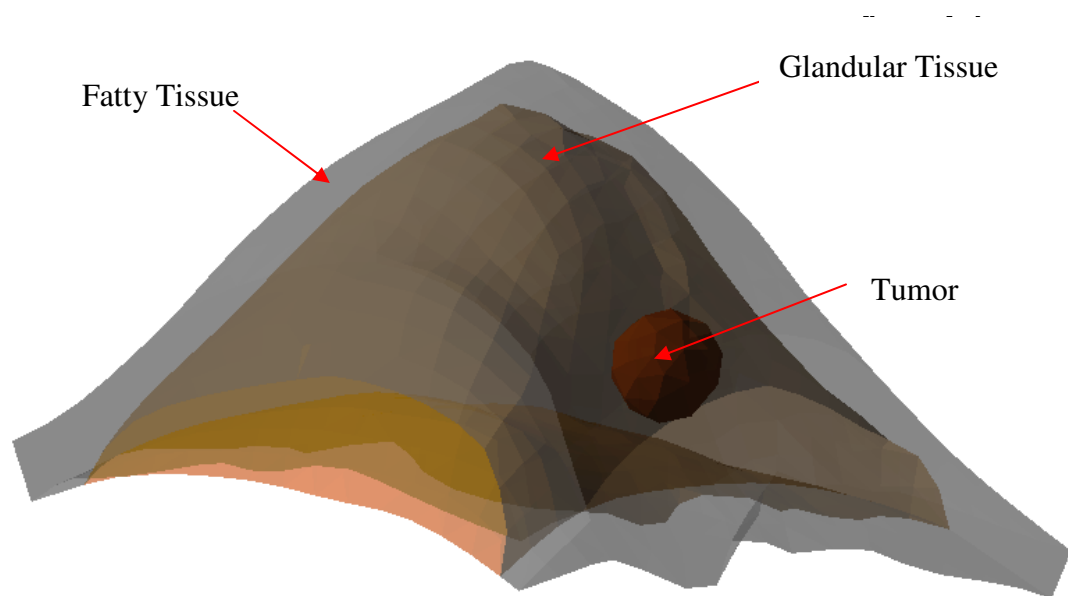


Figure 4-2 A 3-D heterogeneous breast phantom extracted from real CT images, containing fatty tissue, glandular tissue and a tumor.

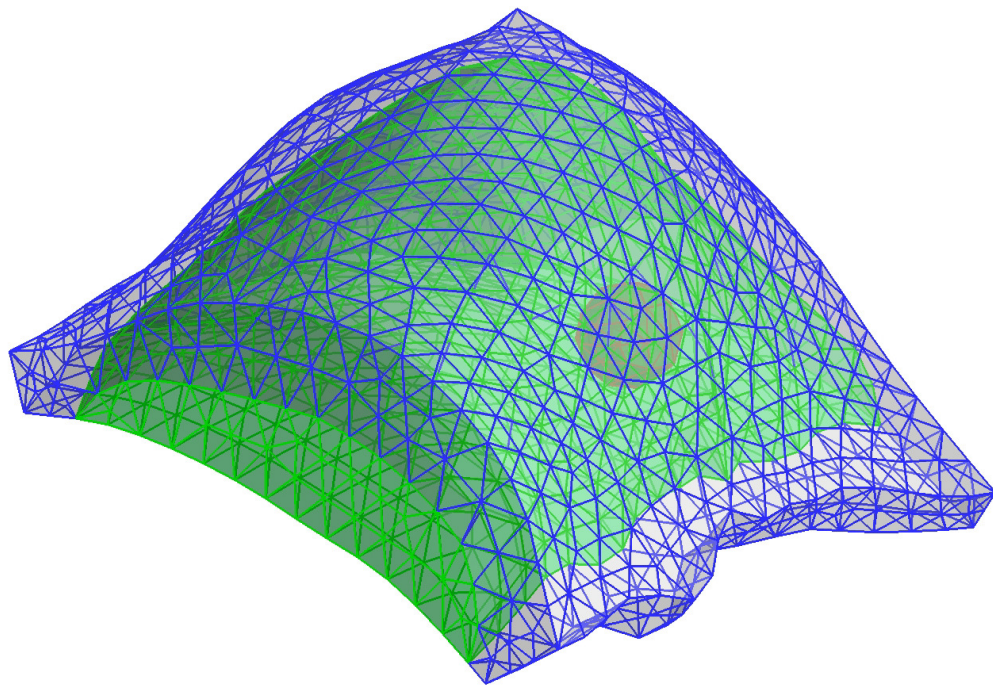


Figure 4-3 FE model for nonlinear elastography.

---

Note: The phantom is discretized with standard 3D tetrahedral elements, consisting of 1583 nodes and 8115 elements.

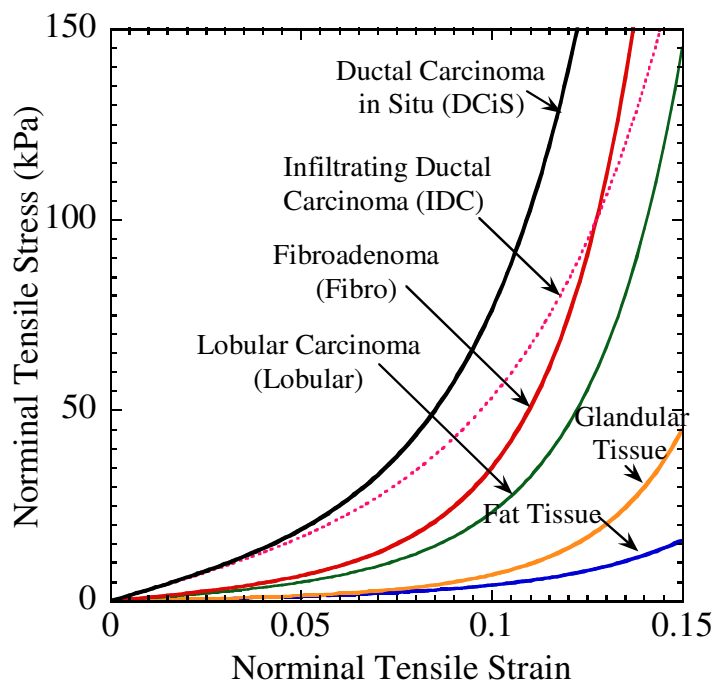


Figure 4-4 Nonlinear stress-strain curves for six breast tissues: fatty tissue, glandular tissue, lobular carcinoma, fibroadenoma, infiltrating ductal carcinoma, and ductal carcinoma in situ.

Source: Wellman, P., 1999, "Tactile imaging", Ph.D. dissertation, Harvard University, Cambridge, Mass, USA.

Note: Lobular carcinoma and fibroadenoma are benign tumors; infiltrating ductal carcinoma, ductal carcinoma in situ are malignant tumors. Curves are fitted to the experimental data in Wellman (1999) and Equation (4.21).



### 4.3.2 Forward Problem

After the breast phantom and material model are established, a forward problem is solved in which material parameters and external loadings are given and deformation is solved. Displacements are zero on the base of phantom. Tilted compression by paddles is applied on upper surface (Figure 4-5). The paddle close to tumor gives compression and another paddle is fixed during loading. Four types of compression loading with different angles are applied. As shown in Figure 3-6, blue lines represent paddle locations before loading, green lines represent those after loadings. Figure 4-7 shows the comparison of paddle locations in four loadings. Note that the right paddle is fixed for all loadings.

The reason that four sets of loadings are applied in forward problem is to provide more information to reconstruct material parameters. Most of inverse problem in elasticity is non-uniqueness. Previous research, for example Liu et al., (2005), has demonstrated that one set of measurements of displacements and forces may not provide sufficient information for the reconstruction of modulus distribution. So we apply multiple sets of loadings to provide more information for reconstruction of material parameters.

Given material parameters and loadings, the displacements and forces can be calculated based on Equation (4.5). The surface forces are used as input to reconstruct material parameters in the inverse problem. In fact, surface displacement and force are equivalent as input to solve inverse problem. Most of previously research applied displacements in linear elastography. In Chapter 3 linear elasto-mammography, displacements measured from mammography projections are used to reconstruct elastic parameters. In this nonlinear elastography study, it is found the reconstruction is more sensitive to force than displacement. Therefore surface force is measured and compared with calculated force to reconstruct material parameters.

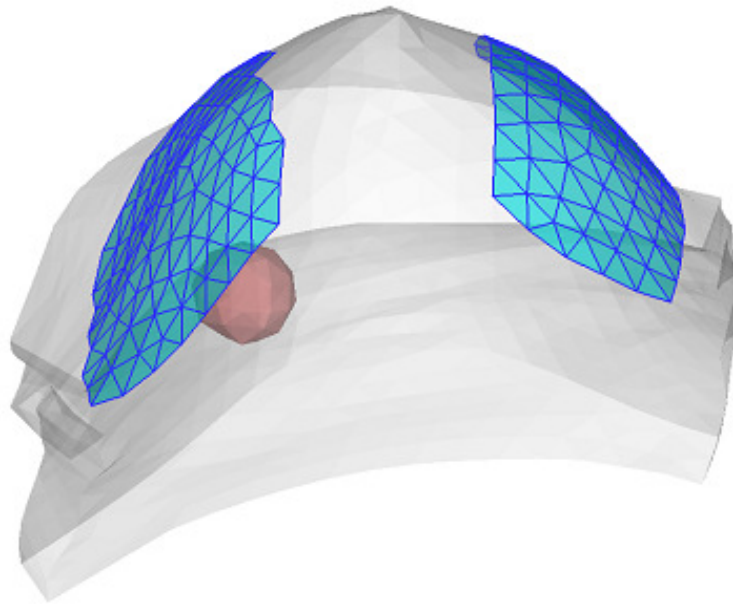
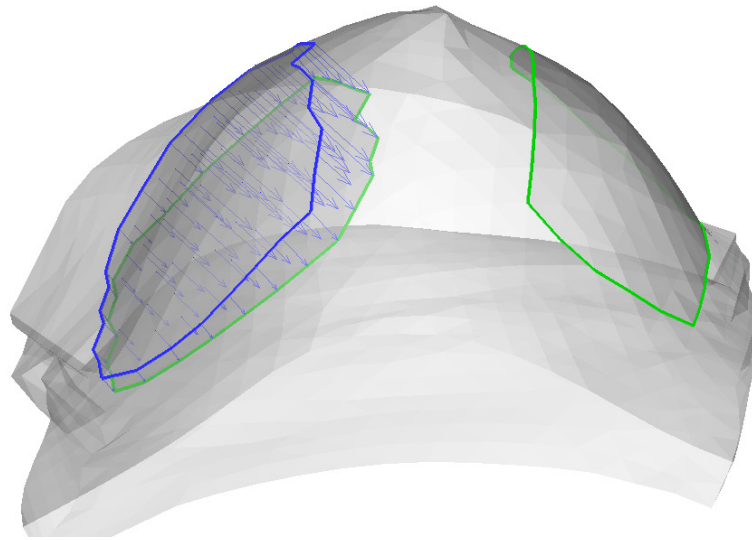


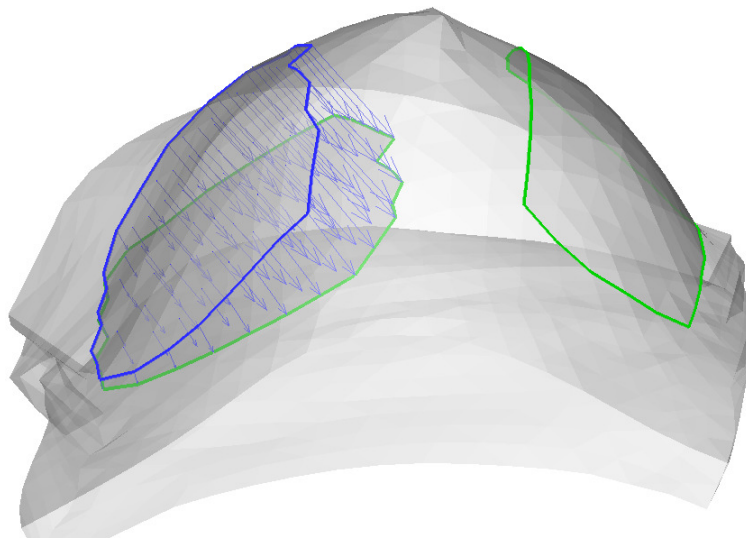
Figure 4-5 Titled compression is given on breast surface by two paddles.

---

Note: The one close to tumor gives displacement loading on breast phantom and another is fixed during loading. The reason to move the paddle close to tumor is to provide more deformation information related with tumor.



(a)

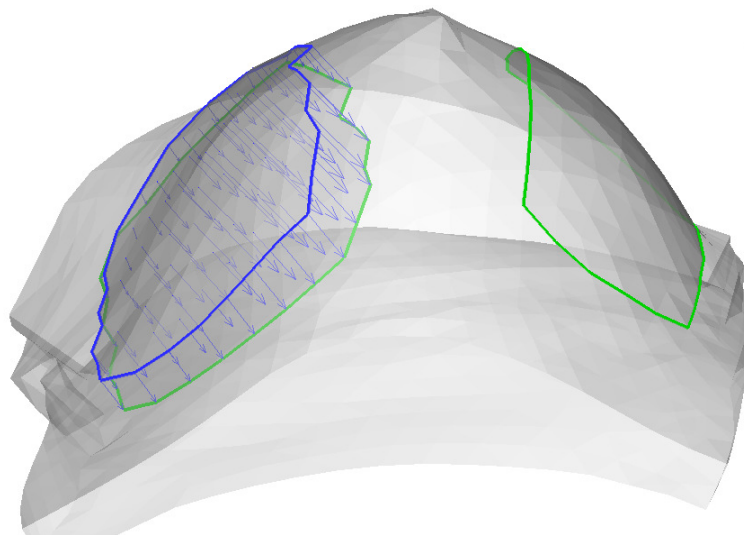


(b)

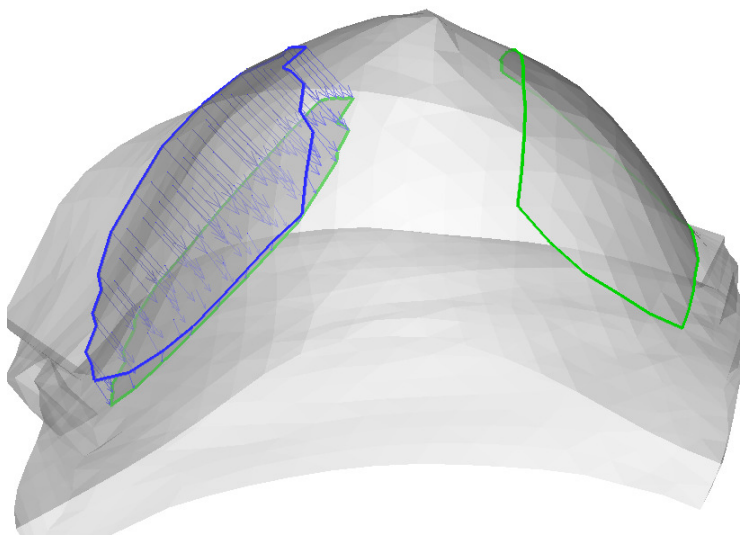
Figure 4-6 Four types of compression loading by paddles.

---

Note: Blue lines represent paddle locations before loadings, green lines represent after loadings. The right paddle is fixed for all loadings.



(c)



(d)

Figure 4-6 Continued

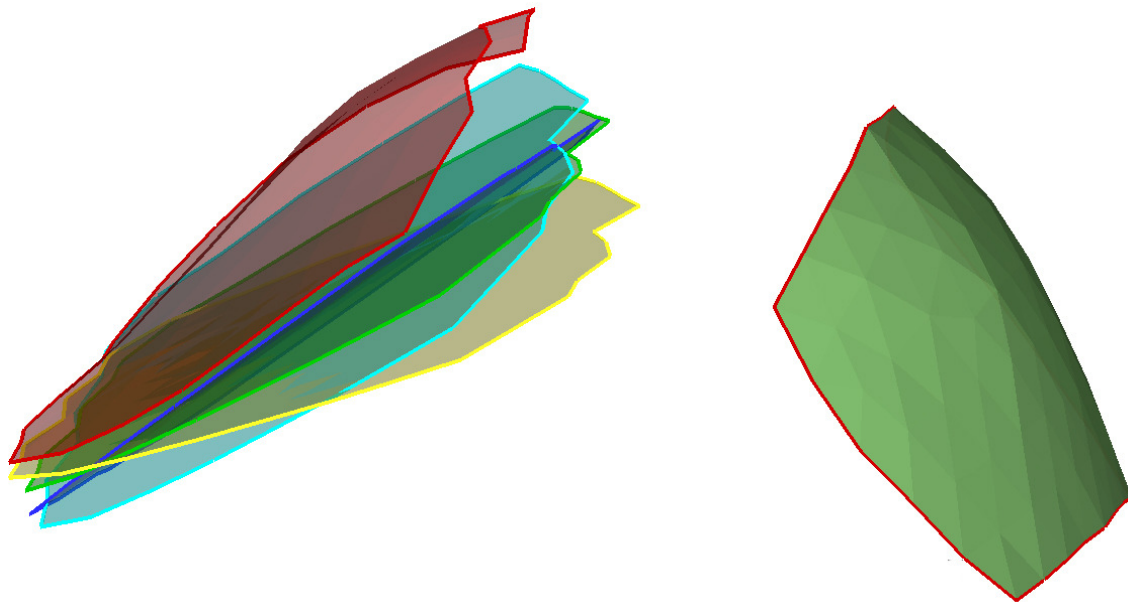


Figure 4-7 Comparison of paddle locations in four loadings.

---

Note: The right paddle is fixed for all loadings.

### 4.3.3 Inverse Problem

Reconstruction for nonlinear elastic moduli in 3-D breast phantom take input extracted from the deformation in response to loading modes A~D described in Figure 4-6. In each loading, the forces on surface nodes are measured as input. Then initial guesses for material parameters are given. In this study, the same initial guesses are applied to three materials:  $\lambda_0 = 20$  ,  $\mu_0 = 10$  ,  $\gamma_0 = 1$  (kPa). Therefore, the surface force can be calculated based on initial guesses of material parameters. The difference between calculated and measured force is used to form the objective function (Equation 4.8). Following the iterative optimization procedures (Figure 4-1), gradients of the objective function are calculated (Equation 4.16) and material parameters are updated. The iteration is put into effect until the objective function is smaller than the preset criterion.

For three materials, elastic parameters are:  $\lambda_f = 35$  ,  $\mu_f = 12.5$  ,  $\gamma_f = 0.4$  for fatty tissue;  $\lambda_g = 50$  ,  $\mu_g = 25$  ,  $\gamma_g = 0.25$  for glandular tissue, and  $\lambda_d = 80$  ,  $\mu_d = 35$  ,  $\gamma_d = 1.5$  for ductal carcinoma in situ. Table 4-1 shows the initial estimate and reconstructed results for nonlinear elastography. The results in the first part are based on the ideal input and the same material parameters are yield, regardless of the initial estimate. It is demonstrated that the reconstructed results are very close to the real values. For parameters of fatty and glandular tissue, the error is less than 0.1%. For parameters of tumor, the error is larger than one of fatty and glandular tissue. For example, the real and reconstructed value of  $\lambda_d$  is 80 and 81.53, with a 1.92% error. It could be explained by the roles of they play in the deformation due to the applied loadings. In general, parameters with the most significant influence on the deformation are also those that are most accurately and easily identified. The influence of a parameter depends on size and location of the material region it belongs to, as well as characteristics of the deformation. For the present simulations, material parameters of the tissue are dominant, while those of tumor are much less influential, due to the small size and deep location of the tumor(s).

The loadings should be close to tumors in order to make tumors have larger deformation. In forward problem the paddles close to tumor give displacement loading on breast phantom and another is fixed during loading. The reason to move the paddle close to tumor is to provide more deformation information related with tumor. A similar situation occurs in linear elastography reconstruction discussed in Section 3.3.3.

Table 4-1 Initial estimate and reconstructed results for nonlinear elastography

	Fatty			Glandular			Tumor		
	$\lambda_f$	$\mu_f$	$\gamma_f$	$\lambda_g$	$\mu_g$	$\gamma_g$	$\lambda_d$	$\mu_d$	$\gamma_d$
Real	35	12.5	0.4	50	25	0.25	80	35	1.5
Guess	20	10	1	20	10	1	20	10	1
	Ideal Input								
Recon	35.00	12.50	0.40	50.05	25.00	0.25	81.53	34.94	1.50
	5% Noise, Without Regularization								
Recon	22.28	8.42	1.51	56.20	21.54	0.25	0.01	41.56	2.00
	5% Noise, With Exponential Form Regularization								
Recon	37.56	12.48	0.46	50.00	25.00	0.24	80.00	39.15	1.50

Note: The results in the first part are based on ideal input, the ones in the second part are based on input with 5% noise and regularization is not used. The third part is based on input with 5% noise and regularization is applied to reduce the impact of noise. ( $\lambda$  and  $\mu$  are dimensionless,  $\gamma$  is in kPa)

## 4.4 Results and Discussion

### 4.4.1 Effect of Noise

The above results are based on ideal input. However, noise cannot be avoidable in experiments. To investigate the capability of the nonlinear elastography algorithm to

handle imperfect real data due to inevitable measurement errors, we conduct reconstruction using noisy input; i.e., each component of measured forces is added with a randomly selected relative error in  $(-5\%, 5\%)$ . The results are shown in the Table 4-1, second part “5% noise, without regularization”. It is obvious that the reconstructed parameters are far away from the real values. The algorithm fails to reconstruct material parameters of nonlinear material model.

A possible reason is that, while the goal is to find real material parameters that minimize the objective function, a global minimum is not well defined with noise. In another words, real material parameters may not give a global minimum of the objective function with noise. Several similar parameters around real ones may give some local minimums. Our algorithm may reach one of them but fail to find real one because they all give local minimums. A typical way to solve this problem is to add a penalty term which provides additional constraint on the solution space. The penalty term may push the solution into the right area of the solution space and minimize the resulting objective. A new objective function is therefore proposed as

$$F = \Phi + \chi\Pi \quad (4.22)$$

where  $\Phi$  is the original objective function (4.8) which represents the difference between measured and calculated values. In addition,  $\chi$  is the regularization factor and  $\Pi$  is the penalty term.

Specific forms of penalty term have been designed for different problems (Hielscher et al., 2001). In this study, an exponential form of penalty term is applied as:

$$\Pi = \sum_{k=1}^K (1 - \exp(-(\xi_k - a_k)^2)) \quad (4.23)$$

where  $K=9$  is the total number of material parameters, and  $\xi_k$  and  $a_k$  are the reconstructed and true elastic parameters, respectively. If the true material parameters are unknown, we can estimate  $a_k$  as close as possible. This is reasonable since several



experiments have provided the nonlinear elastic parameter for breast tissues (Van Houten et al., 2003; Samani et al., 2007).

The results are shown in Table 4-1, the third part “5% Noise, With Exponential Form Regularization”. It is demonstrated that the regularization method significantly improves the reconstruction data. Most of parameters are close enough to the true values. The largest error occurs for  $\gamma$  in fatty tissue from 0.4 to 0.46, approximately 15%. By adding the penalty term, the reconstructed values are pulled from the values that make local minimum of object function into the range close to true values. It is noted that the regularization factor  $\chi$  varies in different scenarios. For example, if we have higher confidence of experiment-data accuracy,  $\chi$  could be smaller. On the contrary, if a high-level noise is expected, we could set  $a_k$  closer to the true value and make  $\chi$  larger so that penalty term has a larger weight in Equation (4.22). For this study, the elastic parameters in fatty and glandular tissues are stable, comparing with the ones in tumors (Figure 4-4). Therefore, larger regularization factors are used for fatty and glandular tissues while smaller  $\chi$  can be applied for tumors.

In Chapter 3 linear elasto-mammography we investigated the effect of noise in Section 3.4.1. The tissue parameters are very accurately identified, with the largest relative error of 4%. The material parameters for tumor have larger error, about 15%. But, in spite of these reconstruction errors, it is still positive that the elasto-mammography results are accurate enough for diagnosis of tumors, noting the significant differences of stiffness between normal tissue, benign and malignant tumors. But for nonlinear elastography, the reconstructed results with 5% noise are far away from real values. For example, reconstructed  $\lambda_d$  for tumor is 0.01 while the real value is 80. We have to use regularization to push it to real value. One of reasons probably is deformation information about tumor. It is demonstrated that it is more difficult to identify material parameters for tumor since it is much less influential on the deformation due to the small size and deep location of tumors. In linear elasto-mammography the deformation

information of tumor is obtained by mammography projections. The information is used to improve the accuracy of reconstruction for tumors. In nonlinear elastography, only deformation information on surface is measured. So it becomes more difficult to reconstruct parameters for tumors.

#### 4.4.2 Linear v.s. Nonlinear

Since elastography emerged as a new technology to imaging tissue elastic modulus in a quantitative manner for detection of breast tumors in 1990s, most approaches assume that the tissue can be modeled as a linear isotropic elastic solid undergoing infinitesimal-strain deformation, and only very few have considered large deformation, nonlinear and anisotropic behaviors of breast tissues and tumor.

It is shown, however, that the deformation of most biological soft tissues is not linear elastic. Krouskop et al. (1998) and Wellman et al. (1999) measured the tissue stiffness changes due to the nonlinear stress-strain relationship in tissue. The experiment shows that fatty tissues are generally characterized by a linear relationship, and normal glandular tissue and fibrous tissue, as well as ductal and intraductal tumors, exhibit nonlinear characteristics, which means the elastic moduli of these tissues vary with strain. That is, if it is assumed that elastic moduli of tissues are constant and large compression, the results of elastography may cause a misdiagnosis. Therefore Varghese et al. (2000) simulated ultrasound elastograms to analyze the effects of nonlinear behavior of breast tissues on the diagnostic value of ultrasound breast elastograms. The results show that there was a significant effect in the contrast of the elastograms due to nonlinearity. The assumption of a linear stress-strain relationship and use of larger applied compressions may lead to misdiagnosis by converting a stiff tumor to a soft one or reducing the contrast between the tumor and its surrounding tissue.

On the other hand, the degree of nonlinearity in the stress-strain relationship of breast tissue, as well as linear elastic properties, may be an indicator of the undergoing

histology. In the experiment by Wellman (1999), elastic moduli at various strain levels were measured and it is found that malignant and benign breast tumors have significant differences in the rate of increase of stiffness with strain. Krouskop et al. (1998) found malignant tumors are much stiffer at a higher strain level as compared to fat or normal glandular tissue.

Therefore it is necessary to develop a nonlinear elastography for clinical application. A nonlinear model that could be used to describe the large deformation of biological tissues should include two items. First, for most soft tissues, the elastic modulus increases as a function of strain. This effect is often referred to as “*material nonlinearity*”. Second, a more complete description of the equilibrium equation, including nonlinear strain-displacement relation, must be used for large deformations. This effect is often referred to as “*geometric nonlinearity*” (Skovoroda et al., 1999).

While there is large collection of work in linear elasticity imaging, there have been few attempts at imaging the nonlinear properties of tissue. Skovoroda et al. (1999) presented a method to reconstruct the elastic modulus of soft tissue based on ultrasonic displacement and strain images for large deformation, however they assumed linear stress-strain behavior, that is, the material nonlinearity was not considered. Erkamp et al. (2004) evaluated nonlinear elastic parameters of tissue using force-displacement data, however they assumed homogeneous material properties and the algorithm is applied on a simple cylindrical phantom. Gokhale et al. (2008) discussed and solved an inverse problem in nonlinear elasticity imaging. They considered the geometric and material nonlinearity of the tissue by assuming a hyperelastic model for the soft tissue. But they assumed homogeneous material properties and numerical simulation was carried on a 2-D simple rectangle phantom.

In this chapter, we developed a new nonlinear elastography which considers the geometric and material nonlinearity, and first present the nonlinear adjoint method to solve inverse problem. In Section 4.2, we present an algorithm based on finite strain

deformation, that is, geometric nonlinearity. The iterative Newton method is applied to solve unknown displacements and forces. In order to find elastic modulus distribution that minimizes the objective function based on measured and calculated forces, the adjoint gradient method is employed to provide user-supplied gradients. Here we first developed a nonlinear adjoint method that significantly improves the numerical efficiency and enhance the stability of elastography reconstruction. In Section 4.3 numerical simulation, we apply a hyperelastic model to describe the large deformation of breast tissue and tumors (material nonlinearity), and establish a 3-D numerical heterogeneous breast phantom extracting from real CT images. Therefore we have considered the geometric and material nonlinearity in this study and developed stable and efficient algorithm for elastography. The results are encouraging for further clinical applications.

#### 4.4.3 Nonlinear Adjoint Methods

Elastography includes forward and inverse problem. In forward problem, material parameters and loadings are given to calculate the deformation; while in inverse problem, external loadings and deformation are known to reconstruct material parameters. Most researchers established certain objective function and minimize it with a proposed iterative algorithm. The challenge is how to calculate the gradient of objective function efficiently and accurately. A straightforward calculation of gradients requires solving stiffness matrix in each of iteration, which takes most of the time consumed in the finite element method.

Recently the adjoint method has been employed to analytically calculate the gradient. Oberai et al. (2003) adopted the adjoint method and proposed a numerical scheme for reconstructing the non-uniform shear modulus field for incompressible isotropic materials using one component of displacement field. Liu et al. (2005) applied

this method for anisotropic materials. In Chapter 3 we apply the adjoint method to reconstruct material parameters in proposed linear elasto-mammography.

But above applications are all for infinitesimal-strain deformation theory, only very few have considered large deformation. It is shown, however, that the deformation of most biological soft tissues is not linear elastic (Wellman et al., 1999). In this study, we have developed the adjoint method for nonlinear elastography in Section 4.2.3.

The advantage of adjoint method is to solve two adjoint displacements during each of iteration ( $w_1$  and  $w_2$  at Equation. (4.17) and (4.18)), instead of the whole stiffness matrix, that increases the numerical efficiency significantly. By introducing the adjoint method, it seems that more equations and variables ( $w_1$  and  $w_2$ ) need to be solved. But the solution of Equation (4.17) and (4.18) is straightforward and computational cost is minimized because stiffness matrix has been computed and factorized when solving forward problem.

A comparison between adjoint method and traditional Gauss-Newton method for gradients calculation could make it clear. In traditional Gauss-Newton method, for each unknown parameter  $P_i$ , we should calculate forward problem twice, for  $P_i$  and  $P_i + \Delta P_i$ , then the gradient could be obtained by  $\Delta\Phi/\Delta P_i$ , where  $\Delta\Phi$  is the change of objective function due to  $\Delta P_i$ . If there are  $N_p$  unknown parameters, we apply  $N_l$  external loadings and the reconstruction iteration process takes  $N_i$  steps. The total computation cost is  $N_{total} = 2 \times N_p \times N_l \times N_i$  forward problem solver. In this study, unknown parameters  $N_p = 9$ , external loadings  $N_l = 4$  and iteration  $N_i \approx 500$ ,  $N_{total} = 2 \times 9 \times 4 \times 500 = 36,000$  forward problem solver. If the adjoint method is applied, for each iterative step, we solve forward problem once regardless of the number of unknown parameters. That is,  $N'_{total} = 1 \times N_l \times N_i = 1 \times 4 \times 500 = 2,000$ , the computation cost is saved more than 90%.

Oberai et al. (2004) compared three different iterative methods: (1) A gradient-based method where the adjoint approach is used to calculate the gradient; (2) A gradient-based method where the straightforward approach is used to calculate the gradient and (3)

the Gauss-Newton method. The results show that “leading-order costs for the gradient-based method with the adjoint approach are smaller than the other two methods”. In fact, without the adjoint method, nonlinear elastography can only be discussed in concepts (Pathmanathan et al., 2004) or applied on simple objects using supercomputing power (Kauer et al., 2004).

In this study we perform numerical simulations on a 3-D numerical heterogeneous breast phantom extracting from real CT images, containing fatty tissue, glandular tissue and a tumor. Deformation of breast tissue is simulated with an exponential hyperelastic model. The material parameters are reconstructed accurately by adopting nonlinear elastography algorithm and adjoint method. The results are encouraging for further clinical applications.

#### 4.4.4 Multiple Sets of Measurements

The key point for using multiple sets of measurements is to bring more deformation modes simultaneously into consideration. The loadings should be close to tumors in order to make tumors have larger deformation. In Figure 4-6, four sets of loadings close to tumors are designed to obtain more deformation for reconstruction. This explanation serves as a guideline for design of loadings in clinical applications. Reduction of the number of required loadings will increase the clinical efficiency and benefit the patients. In other words, loadings with the richest stress-strain information are most desired. The design of feasible loadings is important for success in clinical application of nonlinear elastography.

### 4.5 Conclusions

Elastography is developed as a quantitative approach to imaging elastic properties of tissues to detect suspicious tumors. In this chapter the nonlinear elastography method is introduced for reconstruction of complex breast tissue properties. The elastic parameters are estimated by optimally minimizing the difference between the computed

forces and experimental measures. A reconstruction algorithm based on finite-strain deformation is developed and the nonlinear adjoint method is derived to calculate the gradient of the objective function, which significantly enhances the numerical efficiency and stability. Simulations are conducted on a three-dimensional heterogeneous breast phantom extracting from real imaging including fatty tissue, glandular tissue, and tumors. An exponential-form of nonlinear material model is applied. The effect of noise is taken into account. Results demonstrate that the proposed nonlinear method open the door toward nonlinear elastography and provides guidelines for future development and clinical application in breast cancer study.

## CHAPTER 5 NONLINEAR ELASTO-MAMMOGRAPHY

### 5.1 Introduction

Motivated by the important of detecting breast tumors and the current limitations of mammography and elastography modalities, we have developed a nonlinear elasto-mammography method that takes into consideration of the finite-strain nonlinear properties of breast tissues, in combination with mammography visualizations. In development of nonlinear elasto-mammography, we have experienced two stages as the follows.

First, a *linear elasto-mammography* method was developed to generate the elastograms of breast tissues by combining the conventional low-dose X-ray mammography with elastography framework (introduced in Chapter 3). Instead of using ultrasound or magnetic resonance as in the previous elastography, linear elasto-mammography uses displacement information extracted from mammography projections before and after breast compression. Incorporating the displacement measurement, an elastography reconstruction algorithm was specifically developed to estimate the elastic moduli of heterogeneous breast tissues. Case studies with numerical breast phantoms showed that the displacement measurement obtained from mammography is sufficient to identify the material parameters of breast tissues and tumors within the framework of linear elasticity.

Then, a *nonlinear elastography* method was proposed in Chapter 4. Most of the current elastography (USE or MRE) reconstruction frameworks are based on the assumption of linear elasticity theory. However, the deformation of biological soft tissues cannot be described by linear elastic (Wellman, 1999; Khaled, 2007). Instead, continuum mechanics description with finite-strain nonlinearity is needed. Thus, the consideration of nonlinearity is essential for elastography in clinical application. For the first time, we developed nonlinear elastography method to identify the mechanical properties of soft



breast tissues and tumor, for which a nonlinear adjoint gradient method was introduced to improve the computational efficiency and enhance the stability in elastography reconstruction. The exemplar study demonstrated that the complex nonlinear mechanics of soft breast tissues and tumors can be quantified from displacement measurements for the purpose of detection and evaluation of the tumors.

Based on the accomplishment of linear elasto-mammography and nonlinear elastography, the objective of this chapter is to propose a novel *nonlinear elasto-mammography* method. In Section 5.2, we present the mathematics derivation for elasto-mammography, where a nonlinear adjoint gradient method is modified to consider the projective displacement measurements. In Section 5.3 numerical simulations are described. A 3-D heterogeneous FEM breast phantom is established and Fung's-type nonlinear constitutive model is applied. The material parameters are identified from mammography displacement. Two types of mammography compressive loadings are applied, and the displacements at key points on the tissue interface are extracted from mammography projections before and after deformation. The iterative reconstruction is also detailed. In Section 5.4, the results are presented and the effect of noise is investigated.

## 5.2 Methodology of Nonlinear Elastography

We first recall the finite-strain deformation equations described in Chapter 4 and the objective function. Then a global projection matrix is derived for mammography projection. The nonlinear adjoint method is applied to obtain gradients of the objective function and finally optimization-based reconstruction procedure is described in Section 5.2.5.

### 5.2.1 Finite-Strain Deformation Equations

We first recall the finite-strain deformation equation described in Chapter 4 as:

$$\begin{Bmatrix} f_1^{in}(u_1, u_2; \mathbf{p}) \\ f_2^{in}(u_1, u_2; \mathbf{p}) \end{Bmatrix} - \begin{Bmatrix} f_1^{out}(u_1, u_2) \\ f_2^{out} \end{Bmatrix} = \begin{Bmatrix} 0 \\ 0 \end{Bmatrix} \quad (5.1)$$

The internal nodal force  $f^{in}$  corresponds to stress  $\mathbf{S}$ ; i.e., it changes with  $u_1$  and material parameters  $\mathbf{p}$ , as  $u_2$  is prescribed. The external nodal force  $f_1^{out}$  is due to the prescribed surface force  $\mathbf{t}$  on  $\Gamma_t^0$  and body force  $\mathbf{b}$  in  $\Omega^0$ . It changes with the displacement in large deformation. The nodal force  $f_2^{out}$  is the unknown constraint force on  $\Gamma_u^0$ .

A classic Quasi-Newton method (Press et al., 1996) is employed to solve Equation (5.1) for  $u_1$ . Let  $u_1^{(n)}$  be the trial solution of the unknown  $u_1$  at the  $n$ -th iterative step. An improved solution  $u_1^{(n+1)} = u_1^{(n)} + \delta u_1$  can be obtained at the next step, in which  $\delta u_1$  is the solution of linear equations:

$$K_{11}^{eff}(u_1^{(n)})\delta u_1 = f_1^{in}(u_1^{(n)}, u_2; \mathbf{p}) - f_1^{out}(u_1^{(n)}, u_2) \quad (5.2)$$

where the matrices are calculated at  $u_1^{(n)}$  as

$$K_{11}^{eff} = (K_{11}^{in} - K_{11}^{out}), \quad K_{11}^{in} = \frac{\partial f_1^{in}}{\partial u_1}, \quad K_{11}^{out} = \frac{\partial f_1^{out}}{\partial u_1} \quad (5.3)$$

### 5.2.2 Objective Function

Experimental measurements for elastography include displacement and force. We consider that the biological object  $\Omega^0$  is discretized into FE mesh, and the measurements are discretized consistently into nodal displacement and nodal force. We catalog the measurements as the following:

(i) If the force a node is known (prescribed or measured after deformation), it will be included into  $f_1^{out}$  which is considered ‘‘prescribed’’ in Equation (5.1). The corresponding nodal displacement will be in the constraint displacement, denoted as  $U_1^M$ . Note that  $U_1^M$  corresponds to  $u_1$  in Equation (5.1).

(ii) All the other nodal displacements will be in  $u_2$  and the corresponding nodal force will be in  $f_2^{\text{out}}$ . For category (ii),  $u_2$  must be considered “prescribed” to fulfill the requirement of the well-posedness of a solid-mechanics problem.

For elastography problem, displacement are also measured at some of the nodes associated with  $u_1$ , and are denoted as  $U_1^M$ . Given material parameter  $\mathbf{p}$ , the unknown displacement  $u_1$  and constraint force  $f_2^{\text{out}}$  (which depends on  $\mathbf{p}$ ) will be solved from Equation (5.1). The Elastography method thus searches for  $\mathbf{p}$  so that the overall difference between measured  $U_1^M$  and computed  $u_1$  is minimum, that is, minimize objective function

$$\Phi(\mathbf{p}) = (u_1 - U_1^M)^T \mathbf{X}(u_1 - U_1^M) \quad (5.4)$$

where the diagonal weight matrix  $X = \text{diag}(a_1, a_2, \dots, a_j, \dots)$ . The component  $a_j = 1$  when the  $j$ -th component of  $U_1^M$  is measured or  $a_j = 0$  otherwise. The present algorithm is mathematically equivalent to ones in Chapter 4 for nonlinear elastography where the force is used as “measurement”. For elasto-mammography, displacements could be taken from X-ray projections before and after deformation. So we change the objective function from “force version” in Chapter 4 to this “displacement version”.

In mammography, however, the measurement of displacement is limited by the projection; i.e., only the two components perpendicular to the projection direction are obtainable. Correspondingly, the computed displacement  $u_1$  should be 'projected' to in the same direction as in mammography, and then compared with the mammography measurement  $U_1^M$ . The projection can be represented by a linear translation of  $u_1$ , as  $\mathbf{R}u_1$ , where  $\mathbf{R}$  is the global projection matrix. Let  $u_1'$  be the projected displacement, that is,  $u_1' = \mathbf{R}u_1$ . The objective function for nonlinear elasto-mammography then reads

$$\Phi(\mathbf{p}) = (u_1' - U_1^M)^T \mathbf{X}(u_1' - U_1^M) \quad (5.5)$$

This is noted that Equation (5.5) and Equation (3.9) have the similar form. If the computed displacement  $u_1$  and measurement  $U_1^M$  are in different direction, we can

translate  $u_1$  to  $u'_1$  by global projection matrix  $\mathbf{R}$ . If computed displacement  $u_1$  and measurement  $U_1^M$  are in the same direction,  $\mathbf{R}$  becomes an identity matrix, Equation (5.5) becomes to Equation (3.9).

### 5.2.3 Global Projection Matrix

In objective function (5.5), the global projection matrix  $\mathbf{R}$  is used to translate displacement  $u_1$  to a mammography projection. This section aims to derive the global projection matrix  $\mathbf{R}$ .

To be consistent with computational geometry, we call the projection coordinates as eye coordinates. As illustrated in Figure 5-1, the global coordinates are  $[X, Y, Z]$  and eye coordinates are  $[x, y, z]$ . Their direction vectors are  $\mathbf{E} = [\mathbf{e}_x, \mathbf{e}_y, \mathbf{e}_z]^T$  and  $\mathbf{E}' = [\mathbf{e}'_x, \mathbf{e}'_y, \mathbf{e}'_z]^T$ , respectively. The eye coordinates rotate from global coordinates by three angles: Z-Axis tilt angle  $\psi$ , twist angle about eye/original ray  $\alpha$ , and rotation angle about Z-Axis  $\theta$ . We first need to establish the relation between  $\mathbf{E}$  and  $\mathbf{E}'$ , that is to find a rotation matrix  $[Q]$  such that  $\mathbf{E}' = [Q]\mathbf{E}$ .

When all the angles are zero, the eye view is from the top of  $\mathbf{e}_z$ , that is

$$\mathbf{E}'_{(0,0,0)} = \begin{pmatrix} \mathbf{e}'_x \\ \mathbf{e}'_y \\ \mathbf{e}'_z \end{pmatrix}_{(0,0,0)} = \begin{bmatrix} 1 & 0 & 0 \\ 0 & 1 & 0 \\ 0 & 0 & -1 \end{bmatrix} \begin{pmatrix} \mathbf{e}_x \\ \mathbf{e}_y \\ \mathbf{e}_z \end{pmatrix} \quad (5.6)$$

We have three steps to rotate  $\mathbf{E}'_{(0,0,0)}$  to  $\mathbf{E}'_{(\theta,\psi,\alpha)}$ .

Step 1: Rotate around  $\mathbf{e}'_{z(0,0,0)}$  by angle  $\theta$  and  $\mathbf{E}'_{(0,0,0)}$  becomes  $\mathbf{E}'_{(\theta,0,0)}$

$$\mathbf{E}'_{(\theta,0,0)} = \begin{pmatrix} \mathbf{e}'_x \\ \mathbf{e}'_y \\ \mathbf{e}'_z \end{pmatrix}_{(\theta,0,0)} = \begin{bmatrix} \cos \theta & \sin \theta & 0 \\ -\sin \theta & \cos \theta & 0 \\ 0 & 0 & 1 \end{bmatrix} \begin{pmatrix} \mathbf{e}'_x \\ \mathbf{e}'_y \\ \mathbf{e}'_z \end{pmatrix}_{(0,0,0)} \quad (5.7)$$

Step 2: Rotate around  $\mathbf{e}'_{y(\theta,0,0)}$  by angle  $\psi$  and  $\mathbf{E}'_{(\theta,0,0)}$  becomes  $\mathbf{E}'_{(\theta,\psi,0)}$

$$\mathbf{E}'_{(\theta,\psi,0)} = \begin{pmatrix} \mathbf{e}'_x \\ \mathbf{e}'_y \\ \mathbf{e}'_z \end{pmatrix}_{(\theta,\psi,0)} = \begin{bmatrix} \cos\psi & 0 & -\sin\psi \\ 0 & 1 & 0 \\ \sin\psi & 0 & \cos\psi \end{bmatrix} \begin{pmatrix} \mathbf{e}'_x \\ \mathbf{e}'_y \\ \mathbf{e}'_z \end{pmatrix}_{(\theta,0,0)} \quad (5.8)$$

Step 3: Rotate around  $\mathbf{e}'_{z(\theta,\psi,0)}$  by angle  $\alpha$  and  $\mathbf{E}'_{(\theta,\psi,0)}$  becomes  $\mathbf{E}'_{(\theta,\psi,\alpha)}$

$$\mathbf{E}'_{(\theta,\psi,\alpha)} = \begin{pmatrix} \mathbf{e}'_x \\ \mathbf{e}'_y \\ \mathbf{e}'_z \end{pmatrix}_{(\theta,\psi,\alpha)} = \begin{bmatrix} \cos\alpha & \sin\alpha & 0 \\ -\sin\alpha & \cos\alpha & 0 \\ 0 & 0 & 1 \end{bmatrix} \begin{pmatrix} \mathbf{e}'_x \\ \mathbf{e}'_y \\ \mathbf{e}'_z \end{pmatrix}_{(\theta,\psi,0)} \quad (5.9)$$

Combine the above 3 steps, we finally get:

$$\begin{aligned} \begin{pmatrix} \mathbf{e}'_x \\ \mathbf{e}'_y \\ \mathbf{e}'_z \end{pmatrix}_{(\theta,\psi,\alpha)} &= \underbrace{\begin{bmatrix} \cos\alpha & \sin\alpha & 0 \\ -\sin\alpha & \cos\alpha & 0 \\ 0 & 0 & 1 \end{bmatrix}}_{Q_3} \underbrace{\begin{bmatrix} \cos\psi & 0 & -\sin\psi \\ 0 & 1 & 0 \\ \sin\psi & 0 & \cos\psi \end{bmatrix}}_{Q_2} \underbrace{\begin{bmatrix} \cos\theta & \sin\theta & 0 \\ -\sin\theta & \cos\theta & 0 \\ 0 & 0 & 1 \end{bmatrix}}_{Q_1} \underbrace{\begin{bmatrix} 1 & 0 & 0 \\ 0 & 1 & 0 \\ 0 & 0 & -1 \end{bmatrix}}_{Q_0} \begin{pmatrix} \mathbf{e}_x \\ \mathbf{e}_y \\ \mathbf{e}_z \end{pmatrix} \\ &= \underbrace{Q_3 \cdot Q_2 \cdot Q_1 \cdot Q_0}_{[Q]} \begin{pmatrix} \mathbf{e}_x \\ \mathbf{e}_y \\ \mathbf{e}_z \end{pmatrix} = [Q] \begin{pmatrix} \mathbf{e}_x \\ \mathbf{e}_y \\ \mathbf{e}_z \end{pmatrix} \end{aligned} \quad (5.10)$$

where the rotation matrix is

$$[Q] = \begin{bmatrix} \cos\alpha \cdot \cos\theta \cdot \cos\psi - \sin\alpha \cdot \sin\theta & \cos\theta \cdot \sin\alpha + \cos\alpha \cdot \cos\psi \cdot \sin\theta & \cos\alpha \cdot \sin\psi \\ -\cos\theta \cdot \cos\psi \cdot \sin\alpha - \cos\alpha \cdot \sin\theta & \cos\alpha \cdot \cos\theta - \cos\psi \cdot \sin\alpha \cdot \sin\theta & -\sin\alpha \cdot \sin\psi \\ \cos\theta \cdot \sin\psi & \sin\theta \cdot \sin\psi & -\cos\psi \end{bmatrix} \quad (5.11)$$

Now, consider a displacement vector  $\mathbf{u}$  of a point from undeformed position to deformed position. It is  $\mathbf{u} = \{u_x, v_y, w_z\} \cdot \mathbf{E}$  in the global coordinates, and  $\mathbf{u} = \{u_x, v_y, w_z\} \cdot \mathbf{E}'$  in the eye coordinate, in which

$$\begin{pmatrix} u_x \\ v_y \\ w_z \end{pmatrix} = [Q] \begin{pmatrix} u_X \\ v_Y \\ w_Z \end{pmatrix} \quad (5.12)$$

In mammography projection, the displacement component in  $\mathbf{e}'_z$  direction,  $w_z$ , is not obtainable, and only  $u_x$  and  $v_y$  are measured. Therefore, (5.12) reduces to

$$\begin{aligned}
\begin{pmatrix} u_x \\ v_y \end{pmatrix} &= \underbrace{\begin{bmatrix} \cos \alpha \cdot \cos \theta \cdot \cos \psi - \sin \alpha \cdot \sin \theta & \cos \theta \cdot \sin \alpha + \cos \alpha \cdot \cos \psi \cdot \sin \theta & \cos \alpha \cdot \sin \psi \\ -\cos \theta \cdot \cos \psi \cdot \sin \alpha - \cos \alpha \cdot \sin \theta & \cos \alpha \cdot \cos \theta - \cos \psi \cdot \sin \alpha \cdot \sin \theta & -\sin \alpha \cdot \sin \psi \end{bmatrix}}_{[Q']} \begin{pmatrix} u_x \\ v_y \\ w_z \end{pmatrix} \\
&= [Q'] \begin{pmatrix} u_x \\ v_y \\ w_z \end{pmatrix}
\end{aligned} \tag{5.13}$$

Finally, the FE solution of displacement field  $u_1$ , when projected, becomes  $\mathbf{R}u_1$  where  $\mathbf{R}$  is the assemble of  $[Q']$  according to the FE discretization and assembling methods.

#### 5.2.4 Nonlinear Adjoint Method

Efficient and robust optimization-based elastography schemes request user-supplied gradients of the objective function  $\partial\Phi/\partial\mathbf{p}$ . Direct calculation of the gradients  $\partial\Phi/\partial\mathbf{p}$  involved in the minimization-based parametric identification is difficult, because  $u_1$  is an implicated function of  $\mathbf{p}$ . An adjoint method will be derived here for efficient and analytical calculation of the gradients. To release the implicit coupling between  $u_1$  and  $\mathbf{p}$ , we introduce the constraint Equation (5.1) into the objective function Equation (5.5), and obtain a Lagrangian:

$$L = (\mathbf{R}u_1 - U_1^M)^T \mathbf{X}(\mathbf{R}u_1 - U_1^M) + \begin{Bmatrix} w_1 \\ w_2 \end{Bmatrix}^T \begin{Bmatrix} f_1^{in} - f_1^{out} \\ f_2^{in} - f_2^{out} \end{Bmatrix} \tag{5.14}$$

where  $w_1$  and  $w_2$  are arbitrary virtual displacements.

In this Lagrangian,  $u_1$  and  $\mathbf{p}$  are no longer coupled. It is noted that  $\Phi = L$  and  $\delta\Phi = \delta L$  for arbitrary  $w_1$  and  $w_2$  under the constraint Equation (5.1). The variation  $\delta L$  can be expressed as

$$\begin{aligned}
\delta L &= 2(\mathbf{R}u_1 - U_1^M)^T \mathbf{X}(\mathbf{R}\delta u_1) + (w_1^T K_{11}^{in} - w_1^T K_{11}^{out} + w_2^T \frac{\partial f_2^{in}}{\partial u_1} - w_2^T \frac{\partial f_2^{out}}{\partial u_1}) \delta u_1 \\
&\quad + w_1^T \frac{\partial f_1^{in}}{\partial \mathbf{p}} \delta \mathbf{p} + w_2^T \frac{\partial f_2^{in}}{\partial \mathbf{p}} \delta \mathbf{p} - w_2^T \frac{\partial f_2^{out}}{\partial \mathbf{p}} \delta \mathbf{p}
\end{aligned} \tag{5.15}$$

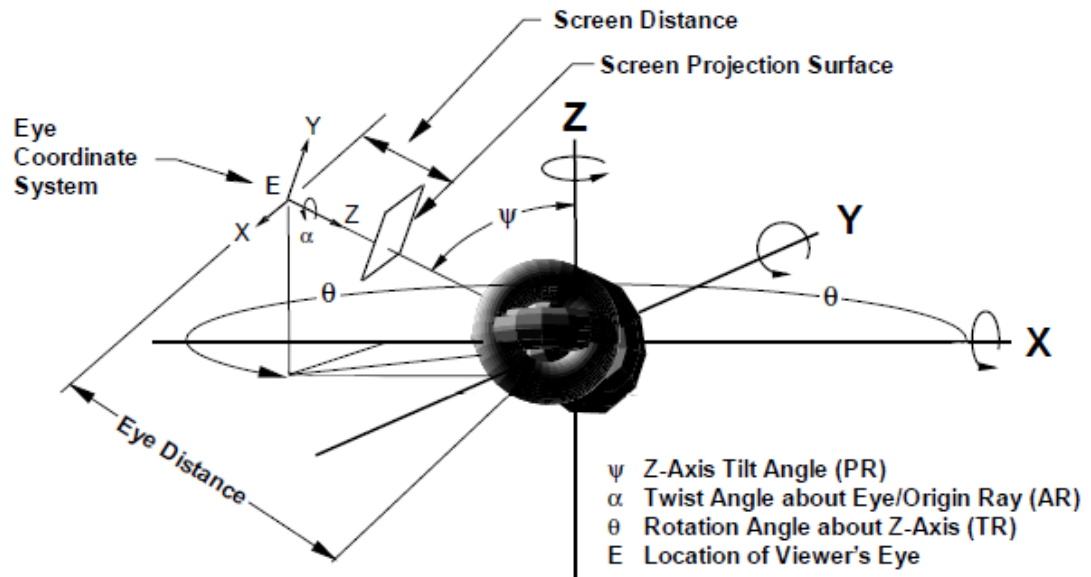


Figure 5-1 Illustration of global coordinate and eye coordinate.

Note: An object in global coordinate is projected in eye coordinate. The relation between direction vectors are dependent on  $\psi$ ,  $\alpha$  and  $\theta$ .

for which the equality constraint Equation (5.1) has been applied. Note that the prescribed external force  $f_1^{out}$  is independent of  $\mathbf{p}$ . Equation (5.15) can be further simplified by letting the arbitrary virtual displacement  $w_2 = 0$ , as:

$$\delta L = \{2(\mathbf{R}u_1 - U_1^M)^T \mathbf{X}\mathbf{R} + w_1^T K_{11}^{in} - w_1^T K_{11}^{out}\} \delta u_1 + w_1^T \frac{\partial f_1^{in}}{\partial \mathbf{p}} \delta \mathbf{p} \quad (5.16)$$

If we select a  $w_1$  to let  $\{2(\mathbf{R}u_1 - U_1^M)^T \mathbf{X}\mathbf{R} + w_1^T K_{11}^{in} - w_1^T K_{11}^{out}\} \delta u_1 = 0$  for arbitrary  $\delta u_1$ , we can get

$$(K_{11}^{in} - K_{11}^{out}) w_1 = -2\mathbf{R}^T \mathbf{X}(\mathbf{R}u_1 - U_1^M) \quad (5.17)$$

$$K_{11}^{eff} w_1 = -2\mathbf{R}^T \mathbf{X}(\mathbf{R}u_1 - U_1^M) \quad (5.18)$$

We obtain the simplest form of  $\delta L$ , as:

$$\delta L = w_1^T \frac{\partial f_1^{in}}{\partial \mathbf{p}} \delta \mathbf{p} = \left( w_1^T \frac{\partial f_1^{in}}{\partial \mathbf{p}} + w_2^T \frac{\partial f_2^{in}}{\partial \mathbf{p}} \right) \delta \mathbf{p} \quad (w_2 = 0) \quad (5.19)$$

Consider that  $\delta \Phi = \delta L$  for arbitrary  $w_1$  and  $w_2$ , we have the gradients of the objective function

$$\frac{\partial \Phi}{\partial \mathbf{p}} = \begin{Bmatrix} w_1 \\ w_2 \end{Bmatrix}^T \begin{Bmatrix} \partial f_1^{in} / \partial \mathbf{p} \\ \partial f_2^{in} / \partial \mathbf{p} \end{Bmatrix} \quad (5.20)$$

where the virtual adjoint displacements  $w_1$  and  $w_2$  are solved from linear equations

$$\begin{cases} (K_{11}^{in} - K_{11}^{out}) w_1 = K_{11}^{eff} w_1 = -2\mathbf{R}^T \mathbf{X}(\mathbf{R}u_1 - U_1^M) \\ w_2 = 0 \end{cases} \quad (5.21)$$

with the tangent stiffness matrix  $K_{11}^{eff}$  defined in (5.3).

By introducing the adjoint method, it seems that more equations (5.21) and variables ( $w_1$  and  $w_2$ ) are involved. But the solution of Equation (5.21) is straightforward and the computational cost is minimal, because  $K_{11}^{eff}$  has been computed and factorized when solving for the displacement  $u_1$  as in Equation (5.2) and (5.3).

The gradients  $\partial \Phi / \partial \mathbf{p}$  can also be calculated directly as



$$\frac{\partial \Phi}{\partial \mathbf{p}} = 2(\mathbf{R}u_1 - U_1^M)^T \mathbf{X} \mathbf{R} \frac{\partial u_1}{\partial \mathbf{p}}. \quad (5.22)$$

in which  $\partial u_1 / \partial \mathbf{p}$  can be computed numerically using finite-different method:

$$\frac{\partial u_1}{\partial \mathbf{p}} \approx \frac{u_1(\mathbf{p} + \delta \mathbf{p}) - u_1(\mathbf{p})}{\delta \mathbf{p}} \quad (\delta \mathbf{p} \text{ is a small increase of } \mathbf{p}) \quad (5.23)$$

or analytically by solving linear equations:

$$K_{11}^{eff} \frac{\partial u_1}{\partial \mathbf{p}} = -\frac{\partial f_1^{in}}{\partial \mathbf{p}} \quad (5.24)$$

For finite-strain nonlinear problem, the finite-different method is unaffordable due to the high computational expense to solve Equation (5.1) for  $u_1$ . Solving Equation (5.24) is straightforward and is much less expensive for  $K_{11}^{eff}$  has been computed and factorized. However, Equation (5.24) needs to be solved for every material parameters involved; for example, in the exemplar simulations in this work, it needs to be solved nine times because each material has three parameters. In comparison, the proposed adjoint method Equations (5.20) and (5.21) require only one solution for  $w_1$ , regardless of the number of material parameters involved.

### 5.2.5 Optimization-based Reconstruction Procedure

The reconstruction procedure is illustrated in Figure 5-2. We first establish a numerical model of the breast tissue and external loadings are applied. In order to measure displacement, we compare the mammography projections before and after the deformation. Then initial guess of distribution for material parameters  $(\lambda, \mu, \gamma)$  is given. It is well known that the mechanical behavior of biological soft tissue is nonlinear. In Chapter 4 we apply hyperelastic model to represent the stress-strain relation of breast tissue and tumor and the material parameters are denoted as  $\mathbf{p} = \{\lambda, \mu, \gamma\}$ . In this chapter we applied the same material model.

Given the external loadings and material parameters, the displacement field  $u_1$  is solved from Equation (5.1), and is projected to  $\mathbf{R}u_1$  according to the mammography

direction. The difference between prediction  $\mathbf{R}u_1$  and measurement  $U_1^M$  are evaluated by the objective function (5.5). The adjoint field  $w$  is calculated by Equation (5.21) and gradients  $\partial\Phi/\partial\mathbf{p}$  are obtained by Equation (5.20). The material parameters could be updated by limited-memory BFGS (L-BFGS) optimization subroutine (Liu et al., 1989). The iteration continues until a minimization is reached.

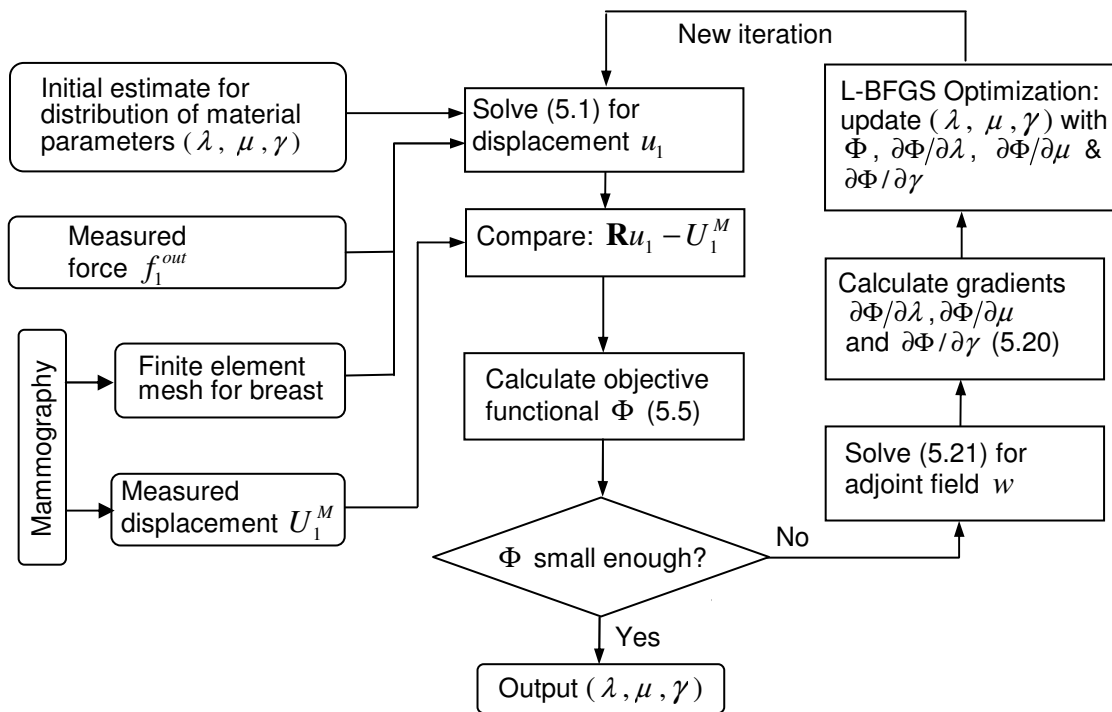


Figure 5-2 Overall flowchart for reconstruction of material parameters  $\lambda$ ,  $\mu$  and  $\gamma$  of breast tissues in nonlinear elasto-mammography.

### 5.3 Numerical Simulations

#### 5.3.1 Breast Phantom and Forward Problem

This section presents phantom simulations to identify the nonlinear elastic properties of the fatty, glandular and cancerous tissues in a breast. In chapter 4 nonlinear elastography, we have established a 3-D breast FEM phantom attracting from the real data (Figure 4-2 and 4-3) and we developed the Fung's model to describe the nonlinear deformation of breast tissues (Figure 4-4). In this chapter the same FEM phantom and material model are applied for nonlinear elasto-mammography.

In the following exemplar study, the material parameters of 'ductal carcinoma in situ' (Wellman, 1999) are assigned to the tumor, as  $\lambda_d = 80$ ,  $\mu_d = 35$ ,  $\gamma_d = 1.5$  ( $\lambda$  and  $\mu$  are dimensionless,  $\gamma$  is in kPa). The parameters for fatty tissue are  $\lambda_f = 35$ ,  $\mu_f = 12.5$ ,  $\gamma_f = 0.4$ , and those for glandular tissue are  $\lambda_g = 50$ ,  $\mu_g = 25$ ,  $\gamma_g = 0.25$ .

Meanwhile four types of loadings are designed for nonlinear elastography in last chapter (Figure 4-6). The base of the breast phantom is fixed. Two paddles are used to apply displacement on the upper surface of the breast. The paddle close to tumor applies tilted compression, and another paddle is fixed to restrict the breast. In this chapter nonlinear elasto-mammography, we apply only two compression loadings on the breast phantom. The two loadings are denoted as compression 1 and 2 and shown at Figure 4-6 (a) and (c).

#### 5.3.2 Acquisition Projection Data

Deformation of the breast can be seen in Figure 5-4 under mammography compression 1. To mimic the displacement obtainable from mammography, we will extract the displacement components in the projection plane at some discrete material points, and denoted them as  $U_1^M$ . We selected three mammography projection directions. With each direction, one projection is made at undeformed state, and one is made at deformed configuration. Then the displacement components on the projection plane are

extracted on a set of landmarks in the tissues by comparing their position in undeformed and deformed projections. The landmarks include the top vertex on the upper breast surface (point A in Figure 5-5), four vertexes of the tumor surface (points B~E in Figure 5-5), and ten material points on the fat-glandular interface (points A~J in Figure 5-6). It is noted that the surfaces of tumor and glandular tissue are not smooth; i.e., there are plenty of landmarks that can be used to track the deformation.

To explain the procedure, we use mammography compression 1 as example. Figure 5-3 shows the mammography projection before deformation. The boundary of the fatty tissue, glandular tissue and a tumor can be seen in the projection. Figure 5-4 shows mammography projection taken in the same direction with compression 1 applied on the breast. Then displacement components on the projection plane can be extracted by comparing the undeformed and deformed projections. More specifically, the undeformed and deformed projections of fatty tissue and the tumor are registered and shown together for the comparison in Figure 5-5. The top vertex of fatty tissue, point A, moves to vertex A' after deformation. Points B~E are vertexes of the tumor in undeformed projection, and they move to vertexes B'~E' after deformation. On the fat-glandular surface, we select additional ten landmarks that move from A~J to A'~J', respectively (Figure 5-6). Thus, by measuring the vector from a point to its deformed position, for example  $A \rightarrow A'$ , the projective displacement components are obtained, and recorded as  $U_1^M$ .

In addition, we make assumption that there is no slip between the paddles and breast surface during mammography compression. Therefore, the displacement of the material points directly compressed by the paddles are considered known (Figure 4-6) and are added to the measurement  $U_1^M$ .

In summary, we have obtained the following displacement measurements from mammography compression:

- (i) The top vertex on the upper breast surface and four vertexes of the tumor;
- (ii) Ten nodes on the fat-glandular interface;

(iii) Material points directly compressed by the paddles.

These displacement measurements are denoted as  $U_1^M$  and are used to identify the material parameters of the tissues.

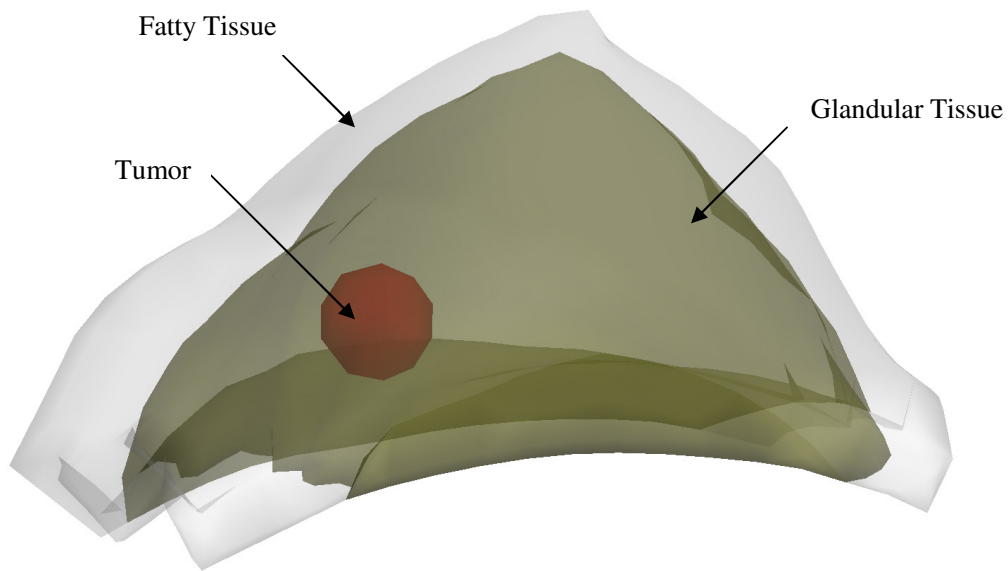


Figure 5-3 Mammography projections for 3-D heterogeneous breast phantom before deformation. Fatty tissue, glandular tissue and a tumor are shown.

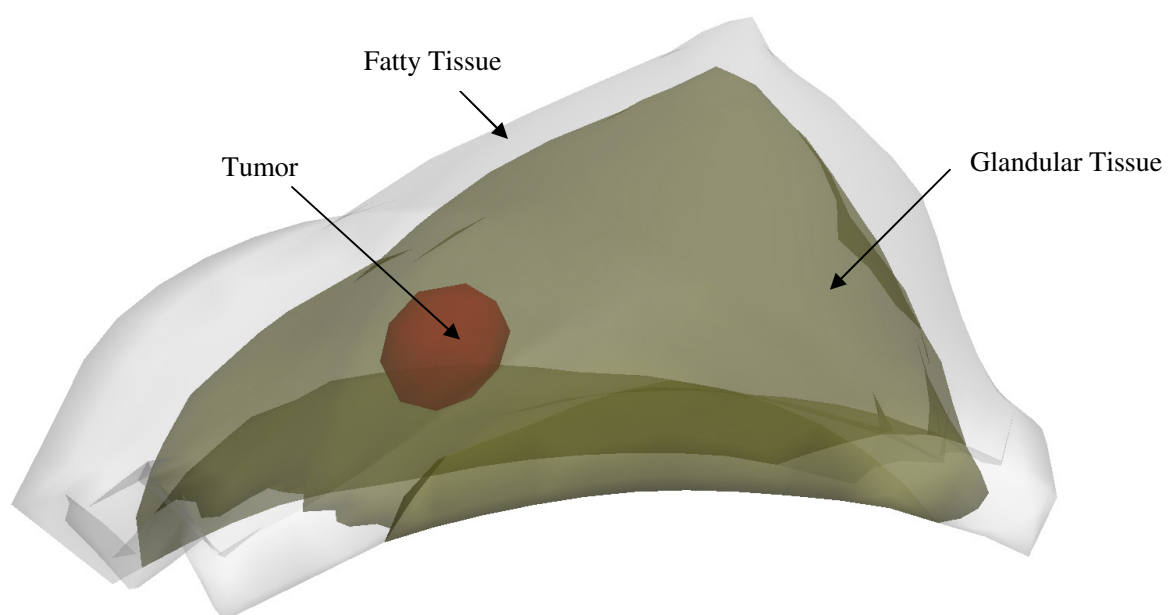


Figure 5-4 Mammography projections for 3-D heterogeneous breast phantom after deformation.

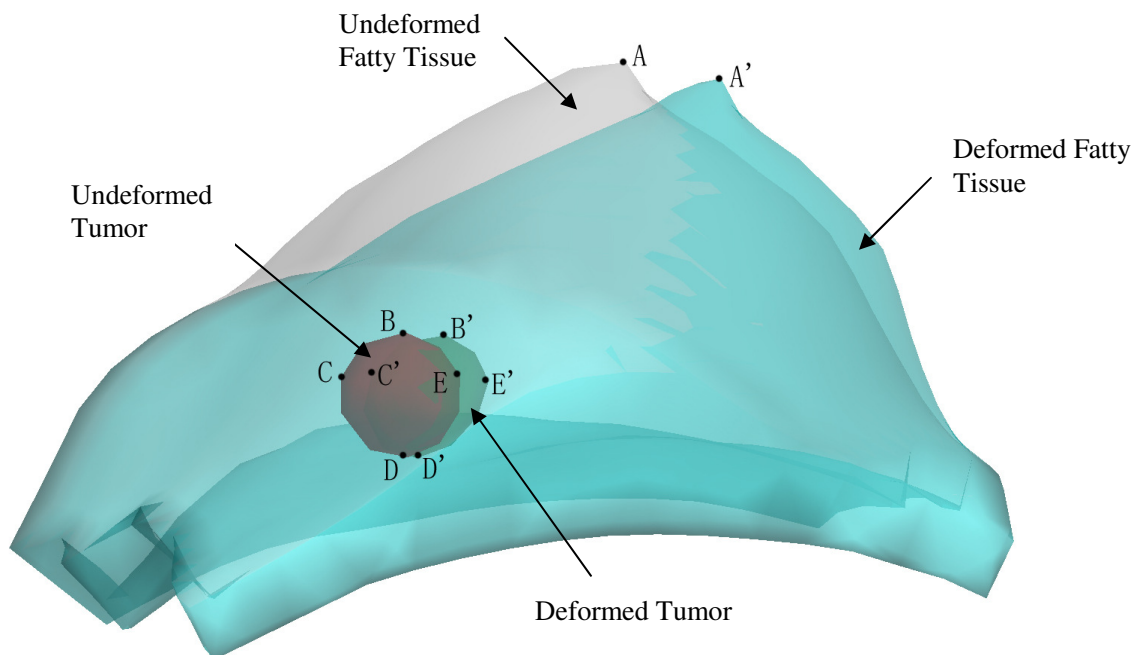


Figure 5-5 Deformed projections overlaps on undeformed projection (only fatty tissue and the tumor are shown).

---

Note: In the projections, vertexes A~E in undeformed projection move to A'~E' in deformed projection, respectively. By comparing mammography projections before and after deformation, displacements of vertexes can be measured.

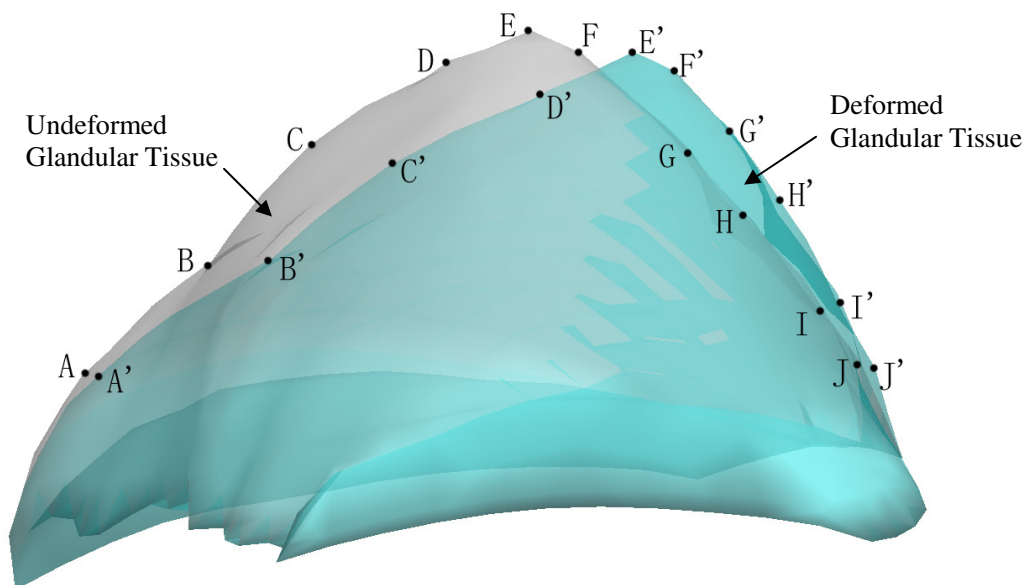


Figure 5-6 Deformed projections overlaps on undeformed projection (only glandular tissue is shown).

---

Note: In the projections, ten nodes A~J on the surface of glandular tissue in undeformed projection move to A'~J' in deformed projection, respectively. By comparing mammography projections before and after deformation, displacements of the nodes can be measured.



### 5.3.3 Inverse problem

Having obtained measurement  $U_1^M$  from mammography compression, the inverse problem will be conducted to identify the material parameters  $\mathbf{p} = \{\lambda_f, \mu_f, \gamma_f, \lambda_g, \mu_g, \gamma_g, \lambda_d, \mu_d, \gamma_d\}$  of the fatty tissue, glandular tissue and tumor (ductal carcinoma in situ), with use of an iterative optimization procedure (Figure 5-2). The initial guesses of the parameters are  $\lambda_0 = 20$ ,  $\mu_0 = 10$ ,  $\gamma_0 = 1$  ( $\lambda$  and  $\mu$  are dimensionless,  $\gamma$  is in kPa) of all materials. With a trial  $\mathbf{p}$ , the displacement field  $u_1$  is solved from the FE equation (5.1), and is projected to  $\mathbf{R}u_1$  according to the mammography direction. The global projection matrix  $\mathbf{R}$  is calculated from Equation (5.11). The difference between prediction  $\mathbf{R}u_1$  and measurement  $U_1^M$  are evaluated by the objective function  $\Phi(\mathbf{p})$  (Equation 5.5). The gradients  $\partial\Phi/\partial\mathbf{p}$  are computed with the proposed nonlinear adjoint method. Then, a modified trial  $\mathbf{p}$  will be obtained according to the present  $\Phi$  and  $\partial\Phi/\partial\mathbf{p}$  by using L-BFGS minimization subroutine (Figure 5-2). The iteration continues until a minimization is reached, which corresponds to identified material parameters.

## 5.4 Results and Discussion

### 5.4.1 Ideal Input

For three materials, elastic parameters are:  $\lambda_f = 35$ ,  $\mu_f = 12.5$ ,  $\gamma_f = 0.4$  for fatty tissue;  $\lambda_g = 50$ ,  $\mu_g = 25$ ,  $\gamma_g = 0.25$  for glandular tissue, and  $\lambda_d = 80$ ,  $\mu_d = 35$ ,  $\gamma_d = 1.5$  for ductal carcinoma in situ. Table 5-1 shows the initial estimate and reconstructed results. The results in the first part are based on the ideal input. It is demonstrated that the reconstructed results are very close to the real values. The maximum error is only 0.3% ( $\gamma$  for tumor). Reconstructions using different initial estimations have been conducted and highly accurate results are obtained. This indicates

efficiency and uniqueness of the proposed elasto-mammography for nonlinear breast tissue properties.

Convergent loci of the elastic parameters ( $\lambda, \mu, \gamma$ ) is plotted in Figure 5-7. It is observed that elastic parameters of fatty tissue and glandular tissue approach the real values rapidly. After about 50 iteration steps, their relative errors are well within the range of 5%. Then they experience some minor adjustment. In contrast, elastic parameters of the tumor converge slower. They start to fall to the real values after 300 steps. After 350 steps all parameters are accurately identified. Reconstructions using different initial estimates have been conducted and very similar convergent profiles are found for the parameters.

The slower convergent speed of elastic parameters of the tumor is explained by the roles they play in the deformation due to the applied loadings, as discussed by Liu et al. (2005). In general, parameters with the most significant influence on the deformation are also those that are most accurately and easily identified. The influence of a parameter depends on size and location of the material region it belongs to, as well as characteristics of the deformation. For the present simulations, elastic parameters of fatty tissue and glandular tissue are dominant, while those of tumor are much less influential, due to the small size and deep location of the tumor. So parameters of fatty tissue and glandular tissue are more accurately and easily identified than those of the tumor (Figure 5-7). Therefore it is crucial for successful reconstruction of elastic breast tissue properties to get sufficient information related with the tumor directly. In this study of nonlinear elasto-mammography, displacements of key points on the tumor are extracted from mammography projections, which increase the accuracy and efficiency to reconstruct the elastic parameters, especially for the tumor.

Table 5-1 Initial estimate and reconstructed results for nonlinear elasto-mammography.

	Fatty			Glandular			Tumor		
	$\lambda_f$	$\mu_f$	$\gamma_f$	$\lambda_g$	$\mu_g$	$\gamma_g$	$\lambda_d$	$\mu_d$	$\gamma_d$
Real	35	12.5	0.4	50	25	0.25	80	35	1.5
Guess	20	10	1	20	10	1	20	10	1
	Ideal Input								
Recon	35.00	12.50	0.40	50.00	25.00	0.25	79.83	34.93	1.51
	5% Noise (I)								
Recon	32.95	11.76	0.44	51.82	26.15	0.23	77.12	31.10	1.69
	5% Noise (II)								
Recon	34.82	12.35	0.41	51.62	26.10	0.23	66.14	29.57	1.88
	5% Noise (III)								
Recon	35.90	12.69	0.39	49.67	25.08	0.25	83.75	37.27	1.40
	10% Noise (I)								
Recon	35.14	12.68	0.40	48.87	24.40	0.26	107.59	35.56	1.41
	10% Noise (II)								
Recon	31.88	11.69	0.46	52.17	25.39	0.24	90.29	31.01	1.69
	10% Noise (III)								
Recon	36.75	12.89	0.37	48.30	24.54	0.26	107.20	48.89	0.92

Note: The results in the first part are based on ideal input, the second part with 5% noise, and the third part with 10% noise.

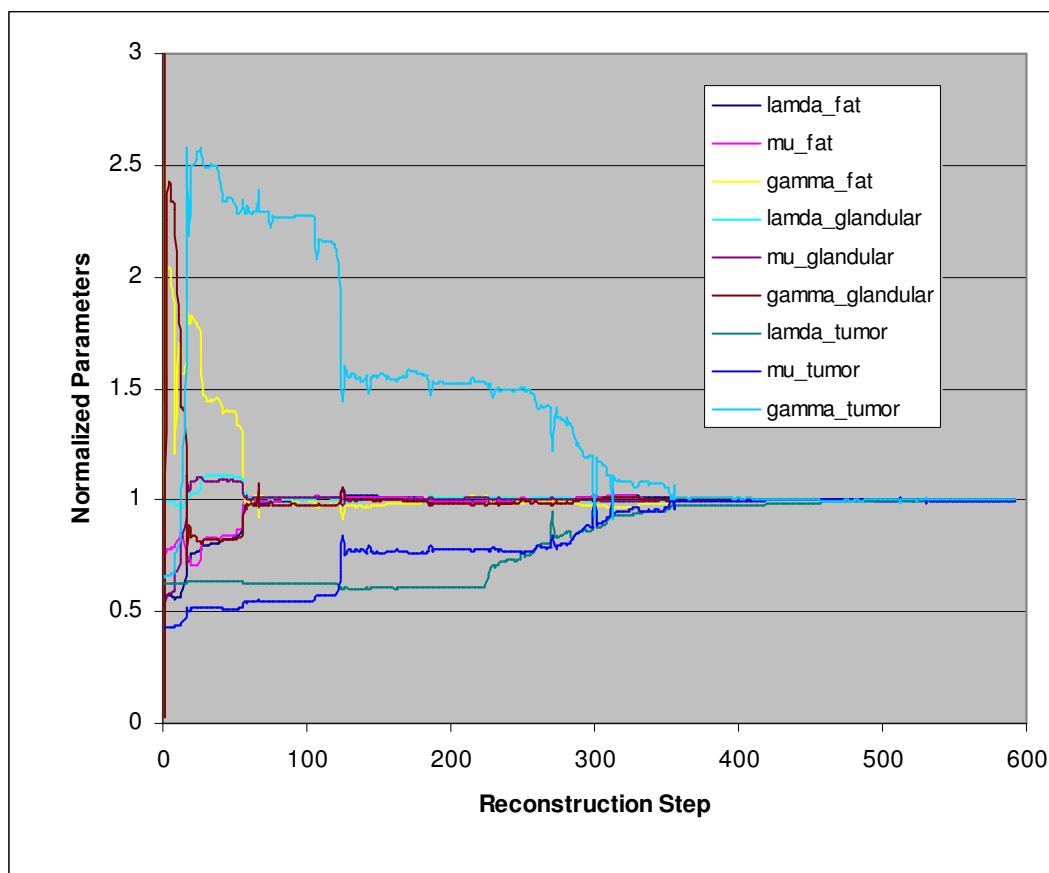


Figure 5-7 Convergent loci of nonlinear elasto-mammography reconstruction for elastic parameters ( $\lambda, \mu, \gamma$ ) of fatty tissue, glandular tissue and tumor, normalized with the exact values correspondingly.

#### 5.4.2 Multiple Sets of Measurements

Because of the nonuniqueness nature of most inverse problems in elasticity, it is important for reconstruction of elastic field of breast tissue to provide sufficient information to reduce the likelihood of nonuniqueness. For 2-D isotropic elastography, Barbone and Bamber (2002) have shown that one set of measurements for the displacements and forces, especially those taken only on the boundaries, may not provide sufficient information to the reconstruction of modulus distribution. Barbone and Gokhale (2004) further demonstrated the feasibility of using multiple displacement fields. Liu et al. (2005) discussed the multiple sets of measurements in 3-D anisotropic media. In our previous study of nonlinear elastography (Wang et al., 2009), four independent titled compression loadings are designed and stable material parameters could be reconstructed. In this study we applied only two sets of loadings and stable material parameters are reconstructed due to different initial guesses. In another word, it is demonstrated that two sets of loadings can provide sufficient information for reconstruction of elastic field. Reduction of the number of required loadings will increase the clinical efficiency and benefit the patients.

The reason of the reduction of the number of required loadings is that more information about the deformation of the tumors is extracted from the mammography projections. As discussed in Section 5.4.1, it is crucial for successful reconstruction of elastic breast tissue properties to get sufficient information related with the tumor directly since the tumor has less influence on the deformation on boundary. In nonlinear elastography we have to increase the number of required loadings to make sure that information is sufficient because all information is obtained on the boundary, without direct information about the tumor. The increase of the number of loadings will cause clinical difficulty and is inconvenient for patients. In this study of nonlinear elastomammography, displacements of key points on the tumor are extracted from

mammography projections, which increase the accuracy and efficiency to reconstruct the elastic parameters, especially those for the tumor. The results have shown that two sets of loadings can provide sufficient information for reconstruction in nonlinear elasto-mammography. The application of mammography not only decreases the cost, comparing with traditional elastography where ultrasound or MR is normally used, but also reduces the number of required loadings which increases the clinical efficiency and benefits the patients.

#### 5.4.3 Iteration Steps

The nonlinear elasto-mammography reconstruction follows an iterative optimization procedure, as schematically shown in Figure 5-2. First the initial guesses for material parameters are given. The displacements can be calculated based on the initial guesses. The difference between calculated and measured displacements is used to set up the objective function (5.5). Following the iterative optimization procedures, gradients of the objective function are calculated and material parameters are updated to approach the optimal values. The iterative optimization procedure is controlled by user-defined criteria. In this study we give a more strict criteria and it takes 592 steps to reach the real nonlinear material parameters. The strain-stress curves of updated material parameters for the tumor in the 1<sup>st</sup>, 100<sup>th</sup>, 200<sup>th</sup>, 300<sup>th</sup> and 592<sup>nd</sup> iterative steps are plotted in Figure 5-8. It is observed that the reconstructed values approach the real ones rapidly in first 300 iterative steps. After that, the reconstructed curve fits the real one very well and experiences some minor adjustment.

In clinical practice a more tolerable criteria may be applied to control iterative optimization procedure to save computational source. It has been recognized that tissue stiffness plays an important role for diagnosis of breast cancers, as tumors are stiffer than that surrounding breast tissues, and malignant tumors are much stiffer than benign ones (Wellman, 1999). In another word, the stiffness ratio of fatty tissue to tumor, instead of

real values, could be used to identify the character of tumor. In Figure 5-8, the lowest curve is for fatty tissue and it is observed that, starting from the 100<sup>th</sup> iterative step, stiffness ratio of fatty tissue to tumor increase rapidly. More tolerable criteria may be designed so that iterative procedure could be stopped when the ratio of fatty tissue to tumor is accurate enough to determine the character of the tumor. It will make this nonlinear elasto-mammography modality more feasible in clinical view.

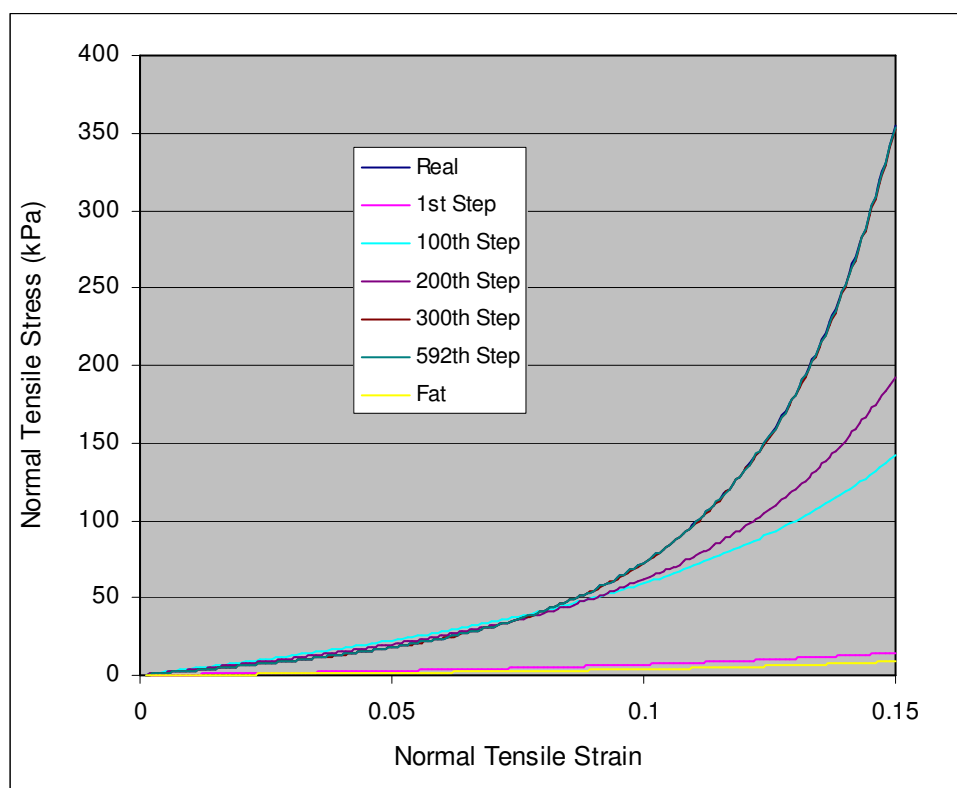


Figure 5-8 Nonlinear stress-strain curves for the tumor in different iteration steps. The lowest curve is for fatty tissue.

#### 5.4.4 Adjoint Method

In the study of nonlinear elastography we introduced for the first time a nonlinear adjoint gradient method that significantly improves the numerical efficiency and enhances the stability of elastography reconstructions (Wang et al., 2009). In this chapter we further developed the adjoint method for nonlinear elasto-mammography. In fact a big challenge of solving inverse problem is how to calculate the gradient of objective function efficiently and accurately. A straightforward calculation of gradients requires solving stiffness matrix in each of iteration, which takes most of the time consumed in the finite element method. Therefore the adjoint method is developed to analytically calculate the gradients. The advantage of adjoint method is to solve adjoint displacement,  $w$ , during each of iteration, instead of the whole stiffness matrix, that increases the numerical efficiency significantly. More details have been discussed in Section 4.4.3.

#### 5.4.5 Input with Noise

The above elasto-mammography reconstructions are conducted using ideal inputs. However, noise can not be avoided in experiments. To investigate the capability of the proposed nonlinear elasto-mammography modality and algorithm to handle imperfect real data due to inevitable measurement errors, we conduct reconstruction using noisy input, that is, each measured displacement is added with a randomly selected relative error 5% or 10%.

The results are shown as Noise 5% (I)~(III) and Noise 10% (I)~(III) in Table 5-1 and the strain-stress curves of material parameters for the tumor are plotted in Figure 5-9. It is observed that curves with noisy input have similar shape to the ones with ideal input. It is not surprised that curves with 10% noise, especially 10% noise (III), have relative larger error than ones with 5% noise. In order to get robust results, we need to make effort to decrease the noise in displacement measurements. It is also noticed that all curves for tumor is far away from the curve of fatty tissue (the lowest curve in Figure 5-



9), in spite of these reconstruction errors. It demonstrates that the nonlinear elastomammography results are accurate enough for diagnosis of tumors, noting the significant differences of stiffness between normal tissue, benign and malignant tumors.

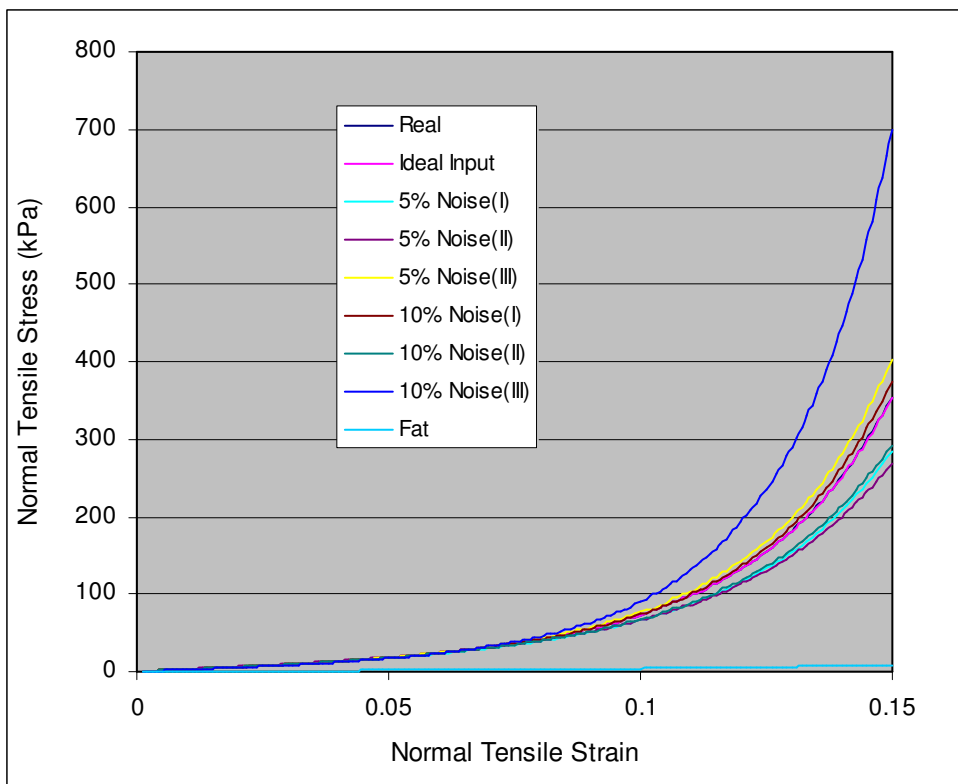


Figure 5-9 Nonlinear stress-strain curves for the tumor with 5% and 10% noise. The lowest curve is for fatty tissue.

In last chapter nonlinear elastography, the algorithm fails to reconstruct material parameters with 5% noisy input. A regularization method is applied to provide additional constraint. In this study, the reconstruction is successful with 5% or 10% noisy input. The possible reason is, as mentioned in Section 5.4.1 and 5.4.2, that direct information about

deformation of tumor is extract from mammography projections, which make it robust and efficient to reconstruct the elastic parameters, especially for the tumor.

### 5.5 Conclusions

This study presents a nonlinear elasto-mammography method that combines elastography and mammography for the purpose of diagnosis of breast tumor by identification of the material parameters of breast tissues and tumor.

A 3-D model is developed for heterogeneous breast tissues extracting from real images including fatty tissue, glandular tissue, and tumors and an exponential-form of nonlinear material model is applied. The displacement information is extract from mammography projections before and after breast compression. A 3-D inverse-problem algorithm is developed to reconstruct nonlinear material parameters. The adjoint gradient method is introduced to improve the numerical efficiency and enhance the stability of reconstruction. Results demonstrate that the proposed methodology is stable and robust for characterization of the elastic moduli of nonlinear breast tissue from the projective displacement measurement.

## CHAPTER 6 DIFFUSE OPTICAL TOMOGRAPHY

### 6.1 Introduction

Elastography have been developed to detect breast tumors by recognizing that the tissue stiffness plays an important role for diagnosis of breast cancers, as tumors are stiffer than the surrounding breast tissues (Sarvazya et al., 1995; Wellman et al., 1999), and malignant tumors are much stiffer than benign ones (Skovoroda et al., 1995). In Chapter 3-5, we have developed the elasto-mammography method for reconstruction of nonlinear breast tissue properties.

In addition to elastic properties differences between normal tissues and tumors, it is known that optical properties of tissue also play important role in clinical diagnostic. Diffuse optical tomography (DOT) emerged as a tool to image optical properties related with physiological change. “Diffuse optical tomography is a medical imaging modality in which tissue is illuminated by near-infrared light from an array of sources, the multiply-scattered light which emerges is observed with an array of detectors, and then a model of the propagation is used to infer the localized optical properties of the illuminated tissue” (Boas et al., 2001).

The DOT work can be divided as forward and inverse problem. *Forward problem* can be stated as: given a distribution of light sources on the boundary of a tissue, and a distribution of tissue optical parameters, find the resulting measurements on boundary. *Inverse problem* can be stated as: given distributions of light source and measurements on boundary, derive the tissue optical parameters distribution within the tissue.

As we have successfully developed nonlinear adjoint method to provide gradient of the objective function in elasto-mammography, we have expanded this method to diffuse optical tomography. We have developed a finite-element-based algorithm to solve the inverse problem of frequent-domain diffusion equation. The nonlinear adjoint method is expanded to complex domains for the reconstruction of optical parameters. Numerical

simulation is carried out and compared with phantom experiments. The results show our adjoint-based algorithm is efficient and robust for reconstructing the optical properties.

The work is organized as follows. In Section 6.2, a finite element optimization-based algorithm is derived to solve the inverse problem of diffusion equation in frequency domain. First the diffuse equation and its finite element form is introduced. Then the objective function is established and adjoint method in the complex domain is developed to provide gradient efficiently. Finally optimization-based reconstruction is explained. In Section 6.3 a phantom experiment is described and our numerical model is given in Section 6.4, followed by our results, discussion and conclusions in Section 6.5.

## 6.2 Methodology

### 6.2.1 Diffuse Equation

Photon transportation in tissue may be modeled in one of two basic ways: an essentially discrete model of individual photon interactions, such as Monte Carlo, or a continuous model based on a differential equation approximation. The most widely applied differential equation in optical imaging is the radiative transfer equation (RTE) (Chandrasekhar, 1950; Ishimaru, 1978).

$$\left(\frac{1}{c} \frac{\partial}{\partial t} + \hat{s} \cdot \nabla + (\mu_a + \mu_s)\right) \phi(r, \hat{s}, t) = \mu_s \int_{s_{n-1}} f(\hat{s}, \hat{s}') \phi(r, \hat{s}', t) d\hat{s}' + q(r, \hat{s}, t) \quad (6.1)$$

which describes the change of the radiance  $\phi(r, \hat{s}, t)$  at position  $r$  in direction  $\hat{s}$  in time  $t$ . The parameters  $\mu_a$  and  $\mu_s$  are the absorption and scattering coefficients respectively,  $c$  is the velocity of light in the medium, and the function  $f(\hat{s}, \hat{s}')$  is the scattering phase function characterizing the intensity of a wave incident in direction  $\hat{s}'$  scattered in direction  $\hat{s}$ .

In biological tissues with highly diffusive light propagations, the RTE can be simplified to a diffusion equation (Arridge, 1999; Gibson et al., 2005)

$$-\nabla \cdot [D_x(r)\nabla\Phi(r,t)] + \mu_a\Phi(r,t) + \frac{1}{c} \frac{\partial\Phi(r,t)}{\partial t} = q_0(r,t) \quad (6.2)$$

where the photon density  $\Phi(r,t) = \int_{s^{n-1}} \phi(r,\hat{s},t) d\hat{s}'$ , diffusion coefficient  $D_x = 1/(3(\mu_a + \mu'_s))$ , reduced scattering coefficient  $\mu'_s = (1-f)\mu_s$ , and  $q_0(r,t)$  is source function.

While in time-domain, the frequency domain form of Equation (6.2) can be obtained by performing the Fourier transform in time ( $\partial/\partial t \rightarrow i\omega$ ):

$$-\nabla \cdot [D_x(r)\nabla\Phi(r,\omega)] + \mu_a\Phi(r,\omega) + \frac{i\omega}{c} \Phi(r,\omega) = q_0(r,\omega) \quad (6.3)$$

In this study we will apply this frequency-domain form in the model.

The solution of Equation (6.2) and (6.3) requires the specification of appropriate boundary condition. A Robin Boundary Condition (RBC) is given by Schweigher et al. (1995)

$$\Phi + 2D_x A \hat{n} \cdot \nabla\Phi = 0 \quad (6.4)$$

where  $A = (1 + \gamma)/(1 - \gamma)$  and  $\gamma$  is the parameter governing the internal reflection at the boundary.  $A$  could be derived from Fresnel's law as

$$A = \frac{2/(1 - R_0) - 1 + |\cos\theta_c|^3}{1 - |\cos\theta_c|^2} \quad (6.5)$$

where  $\theta_c = \arcsin(1/n)$  is the critical angle, and  $R_0 = (n-1)^2/(n+1)^2$ .  $n$  is the refractive index and setting  $n=1$  means no internal reflection.

A finite element method (FEM) is used to calculate solutions of the diffusion equation (6.3) and boundary condition (6.4). FEM is a numerical technique which gives approximate solutions to differential equations. It is especially powerful when dealing with boundary conditions defined over complex geometries that are common in practical applications. In this method, the domain is first discretized into a number of simpler domains called elements. An approximate solution is assumed over an element in terms of solutions at selected points called nodes through interpolation, that is,  $\Phi(r,\omega)$  at each point  $r$  within an element is given by a linear interpolation of nodal value  $\Phi_j$ ,

$$\Phi(r, \omega) = \sum \Phi_j(\omega) \psi_j(r) \quad (6.6)$$

where  $\psi_j$  are linear nodal shape functions with support over all elements which have the node  $N_j$  as a vertex, and  $\psi_j(r_i) = \delta_{ij}$ , where  $r_i$  is the position of node  $N_i$ .

The weak form of diffusion equation (6.3) using the Galerkin approach is given as

$$\int_{\Omega} \psi_j(r) [-\nabla \cdot D_x(r) \nabla + \mu_a + \frac{i\omega}{c}] \Phi(r, \omega) d\Omega = \int_{\Omega} \psi_j(r) q_0(r, \omega) d\Omega \quad (6.7)$$

for each node  $j$ . Integration by parts and substitution of Equation (6.6) leads to

$$\begin{aligned} & \int_{\Omega} [\psi_j(r) \psi_i(r) \frac{i\omega}{c} \Phi_i(\omega) + \nabla \psi_j(r) \cdot D_x(r) \nabla \psi_i(r) \Phi_i(\omega) + \mu_a(r) \psi_j(r) \psi_i(r) \Phi_i(\omega)] d\Omega \\ & = \int_{\Omega} \psi_j(r) q_0(r, \omega) d\Omega - \frac{1}{c} \int_{\partial\Omega} \psi_j(r) \Gamma(r, \omega) d(\partial\Omega) \end{aligned} \quad (6.8)$$

Combined with boundary condition (6.4), we could get

$$[\mathbf{P}(D_x) + \mathbf{Q}(\mu_a) + \frac{i\omega}{c} \mathbf{M} + \mathbf{B}] \Phi(r, \omega) = \mathbf{S}(r, \omega) \quad (6.9)$$

where

$$P_{ij} = \int_{\Omega} D_x(r) \nabla \psi_i(r) \nabla \psi_j(r) d\Omega$$

$$Q_{ij} = \int_{\Omega} \mu_a(r) \psi_i(r) \psi_j(r) d\Omega$$

$$M_{ij} = \int_{\Omega} \psi_i(r) \psi_j(r) d\Omega$$

$$B_{ij} = \frac{1}{2\gamma} \int_{\partial\Omega} \psi_i(r) \psi_j(r) d(\partial\Omega)$$

$$S_i = \int_{\partial\Omega} \psi_i(r) q_0(r, \omega) d(\partial\Omega)$$

$\psi$  is linear nodal shape function.

Equation (6.9) can be rewritten as

$$\mathbf{K}(D_x, \mu_a) \Phi(r, \omega) = \mathbf{S}(r, \omega) \quad (6.10)$$

where  $\mathbf{K}(D_x, \mu_a) = \mathbf{P}(D_x) + \mathbf{Q}(\mu_a) + \frac{i\omega}{c} \mathbf{M} + \mathbf{B}$ .

In Equation (6.10),  $\mathbf{K}(D_x, \mu_a)$  and  $\Phi(r, \omega)$  are complex matrix, we can rewrite them as  $[K] = [K_R] + i[K_I]$  and  $\{\phi\} = \{\phi_R\} + i\{\phi_I\}$ , so Equation (6.10) becomes

$$\begin{cases} [K_R]\{\phi_R\} - [K_I]\{\phi_I\} = \{S\} \\ [K_R]\{\phi_I\} + [K_I]\{\phi_R\} = 0 \end{cases} \quad (6.11)$$

where “ $R$ ” represents real part and “ $I$ ” imaginary part.

### 6.2.2 Objective Function

In diffuse optical tomography near infrared (NIR) light is applied on a biological tissue and the photon density could be *measured* on boundary. Meanwhile if optical parameters are estimated, the photon density on boundary could be *calculated* by Equation (6.10). The objective of diffuse optical tomography is to optimally find the optical parameters that minimize the difference between the measured and calculated photon density.

Denoting the measured photon density on boundary as  $\{\phi^m\}$ , and calculated photon density associate with estimated distribution of optical parameters as  $\{\phi\}$ , the diffuse optical tomography seeks optical parameters  $(\mu_a, \mu'_s)$  such that the following objective  $G(\mu_a, \mu'_s)$  is optimally minimized:

$$\begin{aligned} G(\mu_a, \mu'_s) &= G_R(\mu_a, \mu'_s) + G_I(\mu_a, \mu'_s) \\ &= (\{\phi_R\} - \{\phi_R^m\})^T [X_R] (\{\phi_R\} - \{\phi_R^m\}) + (\{\phi_I\} - \{\phi_I^m\})^T [X_I] (\{\phi_I\} - \{\phi_I^m\}) \end{aligned} \quad (6.12)$$

where matrix  $[X_R]$  and  $[X_I]$  have the same dimensions with matrix  $[K_R]$  and  $[K_I]$ , but are diagonal, and  $X_{ii}$  equals to zero when the  $i$ -th component of in  $\{\phi\}$  is *not* measured.

The DOT reconstruction follows an iterative optimization procedure, as schematically shown in Figure 6-1. The initial estimation for distribution of optical parameters  $(\mu_a, \mu'_s)$  is given. Light intensity  $\phi$  can be calculated by Equation (6.11) and objective function is obtained by comparing measured and calculated light intensities.

Then optical parameters are updated for next iteration until a satisfied objective function is obtained.

### 6.2.3 Adjoint Method

The iterative optimization procedure usually request user-supplied gradient. The previous diffuse optical tomography studies used direct or approximate finite-different method for the gradient calculation. The computation expense of these methods increases proportionally with the number of material parameters. Recently an adjoint method was introduced to compute the gradient analytically (Tardieu et al, 2000; Oberai et al., 2003; Liu et al., 2005 & 2006). Oberai et al. (2003) adopted the adjoint method and proposed a numerical scheme for reconstructing the nonuniform shear modulus field for incompressible isotropic material using one component of displacement field. Liu et al. (2006) applied this method for anisotropic materials. In Chapter 3 we apply the adjoint method for linear elasto-mammography. In Chapter 4 and 5 we develop new nonlinear adjoint method to reconstruct nonlinear elastic parameter in nonlinear elastography and elasto-mammography. In this chapter we expand the adjoint method from elastography to diffuse optical tomography to provide efficient gradient calculation for reconstruction of optical parameters.

The goal of the adjoint method is to calculate the gradient  $\partial\Phi/\partial\mu_a$  and  $\partial\Phi/\partial\mu'_s$  efficiently. We define the adjoint field  $\{w\}$  as

$$\{w\} = \{w_R\} + i\{w_I\} \quad (6.13)$$

where  $\{w\}$  has the same dimension as  $\{\phi\}$ , “*R*” represents real part and “*I*” imaginary part. The weak form of Equation (6.11)

$$\begin{cases} \{w_R\}^T ([K_R]\{\phi_R\} - [K_I]\{\phi_I\} - \{S\}) = 0 \\ -\{w_I\}^T ([K_R]\{\phi_I\} + [K_I]\{\phi_R\}) = 0 \end{cases} \quad (6.14)$$

for arbitrary choice of  $\{w\}$ . We introduce Equation (6.14) into objective function (6.12) and obtain a Lagrangian:



$$\begin{aligned}
L(\mu_a, \mu'_s, \{\phi\}, \{w\}) = & \\
& (\{\phi_R\} - \{\phi_R^m\})^T [X_R] (\{\phi_R\} - \{\phi_R^m\}) + (\{\phi_I\} - \{\phi_I^m\})^T [X_I] (\{\phi_I\} - \{\phi_I^m\}) \quad (6.15) \\
& + \{w_R\}^T ([K_R] \{\phi_R\} - [K_I] \{\phi_I\} - \{S\}) - \{w_I\}^T ([K_R] \{\phi_I\} + [K_I] \{\phi_R\})
\end{aligned}$$

It is shown that  $G(\mu_a, \mu'_s) = L(\mu_a, \mu'_s, \{\phi\}, \{w\})$  and  $\delta G = \delta L$  as Equation (6.14) is satisfied for arbitrary  $\{w\}$ . Then  $\delta L$  can be written as

$$\begin{aligned}
\delta L = & (2(\{\phi_R\} - \{\phi_R^m\})^T [X_R] + \{w_R\}^T [K_R] - \{w_I\}^T [K_I]) \{\delta\phi_R\} \\
& + (2(\{\phi_I\} - \{\phi_I^m\})^T [X_I] - \{w_R\}^T [K_I] - \{w_I\}^T [K_R]) \{\delta\phi_I\} \quad (6.16) \\
& + \{w_R\}^T ([\delta K_R] \{\phi_R\} - [\delta K_I] \{\phi_I\}) - \{w_I\}^T ([\delta K_R] \{\phi_I\} + [\delta K_I] \{\phi_R\})
\end{aligned}$$

In order to compute  $\{w\}$ , let

$$2(\{\phi_R\} - \{\phi_R^m\})^T [X_R] + \{w_R\}^T [K_R] - \{w_I\}^T [K_I] = 0 \quad (6.17)$$

and

$$2(\{\phi_I\} - \{\phi_I^m\})^T [X_I] - \{w_R\}^T [K_I] - \{w_I\}^T [K_R] = 0, \quad (6.18)$$

Equation (6.17) and (6.18) can then be rewritten as

$$[K_R] \{w_R\} - [K_I] \{w_I\} = -2[X_R] (\{\phi_R\} - \{\phi_R^m\}) \quad (6.19)$$

and

$$[K_R] \{w_I\} + [K_I] \{w_R\} = 2[X_I] (\{\phi_I\} - \{\phi_I^m\}) \quad (6.20)$$

Combining Equation (6.19) and (6.20), we can obtain

$$([K_R] + i[K_I]) (\{w_R\} + i\{w_I\}) = -2[X_R] (\{\phi_R\} - \{\phi_R^m\}) + i2[X_I] (\{\phi_I\} - \{\phi_I^m\}) \quad (6.21)$$

$$[K] \{w\} = -2[X_R] (\{\phi_R\} - \{\phi_R^m\}) + i2[X_I] (\{\phi_I\} - \{\phi_I^m\}) \quad (6.22)$$

It is noted that the matrix  $[K]$  is as the same as that in Equation (6.11). Therefore,  $\{w\}$  can be solved by Equation (6.22) with the same method. Correspondingly,

$$\delta G = \{w_R\}^T ([\delta K_R] \{\phi_R\} - [\delta K_I] \{\phi_I\}) - \{w_I\}^T ([\delta K_R] \{\phi_I\} + [\delta K_I] \{\phi_R\}) \quad (6.23)$$

Since  $K_I$  is independent with  $\mu_a$  and  $\mu'_s$ ,  $\delta K_I = 0$ ,  $\delta G$  further becomes as follows:

$$\delta G = \{w_R\}^T [\delta K_R] \{\phi_R\} - \{w_I\}^T [\delta K_R] \{\phi_I\}. \quad (6.24)$$

In this study, we have optical parameters  $\{\mu_a, \mu'_s\}$ , the gradient could be calculated by

$$\begin{cases} \frac{\partial G}{\partial \mu_a} = \{w_R\}^T \left[ \frac{\partial K_R}{\partial \mu_a} \right] \{\phi_R\} - \{w_I\}^T \left[ \frac{\partial K_R}{\partial \mu_a} \right] \{\phi_I\} \\ \frac{\partial G}{\partial \mu'_s} = \{w_R\}^T \left[ \frac{\partial K_R}{\partial \mu'_s} \right] \{\phi_R\} - \{w_I\}^T \left[ \frac{\partial K_R}{\partial \mu'_s} \right] \{\phi_I\} \end{cases} \quad (6.25)$$

where the adjoint field  $\{w\}$  could be obtained in Equation (6.22).

It is noted that  $\{\phi\}$  and  $\{w\}$  share the same Cholesky factorization (Belytschko et al., 2000) for  $[K]$ , thus the computational expense for solving  $\{w\}$  in Equation (6.22) is minimal once  $\{\phi\}$  is solved in Equation (6.11). At the same time, once adjoint field  $\{w\}$  is calculated, gradients for different parameters are calculated by Equation (6.25), which shares the same adjoint field. The feature makes the adjoint method not impacted by the number of unknown parameters significantly.

#### 6.2.4 Optimization-based Reconstruction Procedure

The reconstruction frame involved data acquisition, material modeling, and reconstruction of material parameters, shown with the flowchart in Figure 6-1. The data acquisition includes establishing finite-element model and measuring light intensities. In the study of elasto-mammography, the measured displacements are obtained by mammography projections in numerical simulation. In this DOT measured light intensity  $\phi^m$  is obtained by experiment described in next section. Material modeling includes initial estimation for distribution of optical parameter  $\{\mu_a, \mu'_s\}$ . The reconstruction procedure is optimization-based, making use of a limited-memory BFGS (L-BFGS) optimization subroutine (Liu et al., 1989), for which user-supplied gradients are required. When solving photon density  $\phi$  with finite-element method, the factorization of matrix  $K$  in Equation (6.11) is stored at each time step, and is used for the adjoint field  $w$ . Once initial guesses of distribution of optical parameters  $\{\mu_a, \mu'_s\}$  are given, light intensities are calculated in forward problem. The calculated and measured light intensity,  $\phi$  and  $\phi^m$ , are used to form objective function (6.12). Gradients are obtained by calculating adjoint

field  $w$  and optical parameters are updated. New iteration is repeated until a satisfied objective function is obtained.

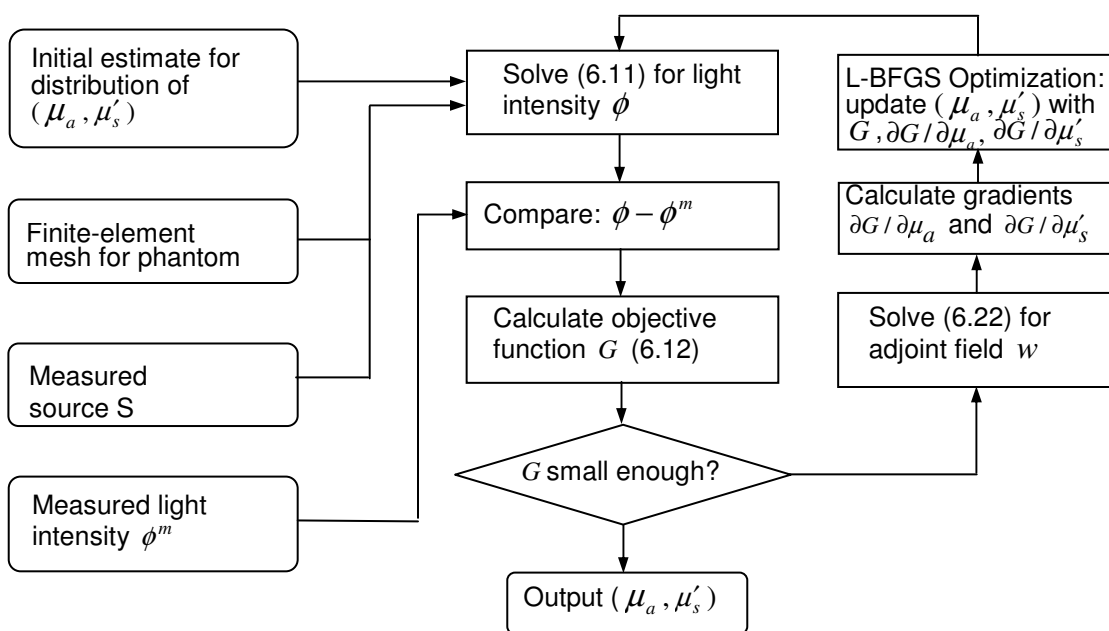


Figure 6-1 Flow chart of diffuse optical tomography reconstruction of optical coefficients  $\{\mu_a, \mu'_s\}$  in frequent domain

### 6.3 Experiment

An experiment is made to test DOT reconstruction algorithm developed in last section. The experiment is conducted with a frequency-domain DOT system by Prof. Gulsen's group in Center for Functional Onco-Imaging, UC-Irvine (Gulsen et al., 2006). They kindly shared the experimental data. Then we set up a numerical model to reconstruct the optical parameters based on the experimental data.

A 63-mm-diameter solid phantom simulating tissue optical properties was used in the experiment. The optical properties of the phantom are  $\mu_a = 0.0132 \text{ mm}^{-1}$  and  $\mu_s' = 0.86 \text{ mm}^{-1}$  at 785 nm. A 15-mm hole was drilled into the phantom to simulate different embedded objects. The hole was positioned halfway between the center and the edge and was filled with a mixture of Intralipid and Indian ink in water to simulate a higher absorbance object with  $\mu_a = 0.0264 \text{ mm}^{-1}$  and  $\mu_s' = 0.86 \text{ mm}^{-1}$ . Sixty-four amplitude and phase data at 785 nm are given and converted to the real and imaginary parts to compare with numerical results. The details of the system are given in Gulsen et al. (2006).

## 6.4 Numerical Simulation

### 6.4.1 Finite Element Model

Based on the phantom and experimental systems described in Section 6.3, we established a 2-D finite element model consisting of a 63-mm-diameter circle matrix with an embedded inclusion (Figure 6-2). The embedded inclusion is 15-mm diameter and is positioned halfway between the center and the edge, that is, the centers of matrix and inclusion are  $(0, 0)$  and  $(63/4, 0)$ . The eight solid circles represent the detectors while the eight open circles represent the light sources. The sources and detectors are placed uniformly on the external surface with  $45^\circ$  apart.

The model discretized with standard 2-D triangle elements has 1761 nodes and 3264 elements, in which 3146 elements are in matrix and 118 elements are in the inclusion. The elements close to surface are refined because intensities on surface are collected for reconstruction of the optical parameters. A constant light source is applied and the intensities on surface are detected. The difference between calculated and measured value is employed to establish the objective function (6.12).

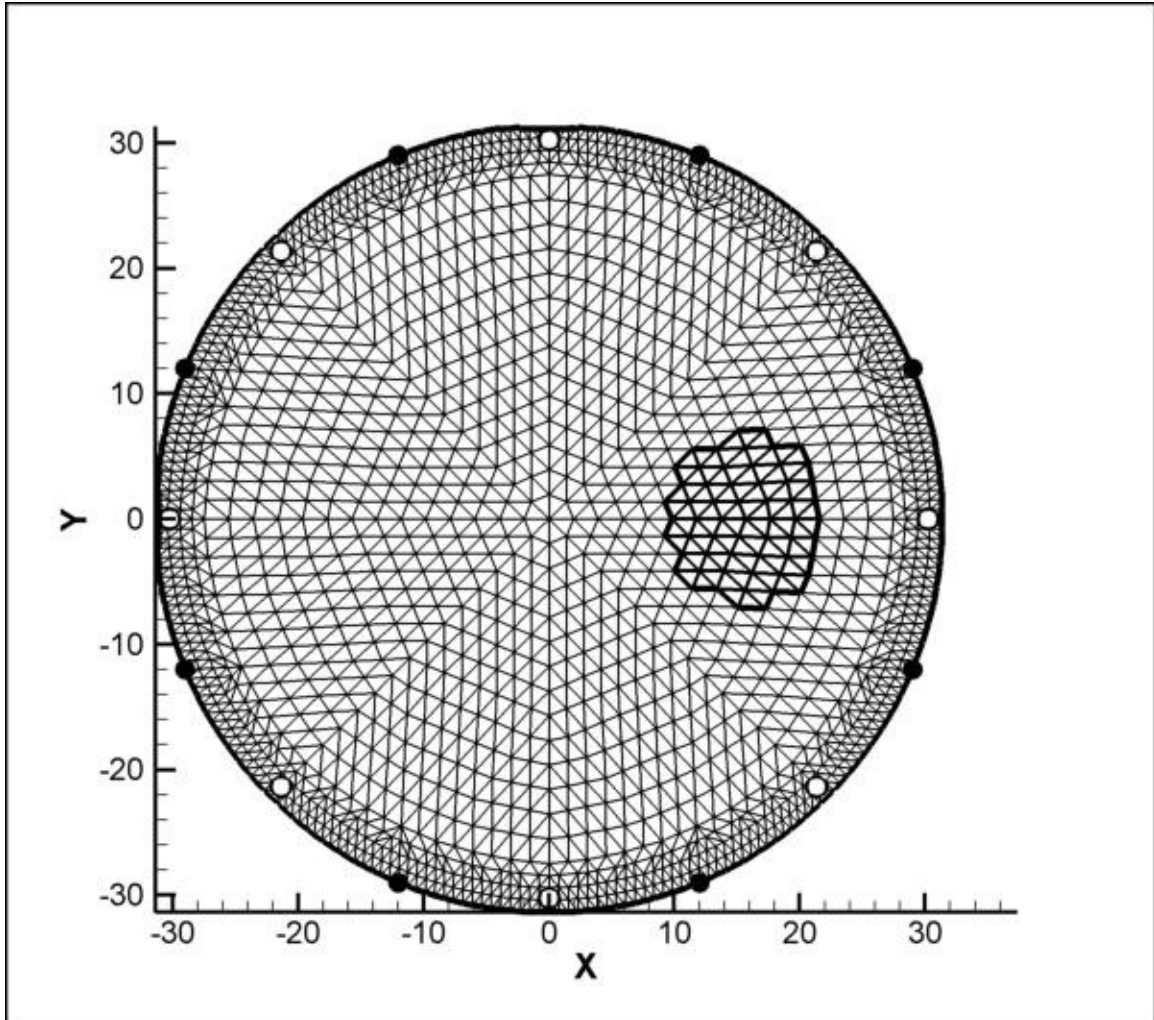


Figure 6-2 FE model with 3264 elements and 1761 nodes to simulate the phantom.

Note: Thick mesh represents inclusion, solid circles represent detectors, and open circles represent light sources.

It is noted that, although the light sources are placed on the phantom surface, the diffusion equation cannot describe the collimated source correctly. A common approach to overcome this limitation is to represent a collimated pencil beam by an isotropic point source located at a depth  $1/\mu'_s$  below the tissue surface (Arridge et al., 1995). This produces accurate results at distance from the source larger than the mean free path, but breaks down close to the source. Using this approach, the eight light sources are located at a depth  $1/\mu'_s = 1/0.86 \text{ mm} = 1.16 \text{ mm}$  below the surface.

#### 6.4.2 Inverse Problem

It is introduced in Section 6.1 that the DOT work can be divided as forward and inverse problem. Forward problem can be stated as: given a distribution of light sources on the boundary of a tissue, and a distribution of tissue optical parameters, find the resulting measurements on boundary. Inverse problem can be stated as: given distributions of light source and measurements on boundary, derive the tissue optical parameters distribution within the tissue.

In this study the experiment service as the forward problem solver. The distribution of light sources and tissue optical parameters are given, the resulting light intensities are measured at detectors, that is,  $\{\phi^m\}$  in objective function (6.12).

Based on the experimental measurement, inverse problem is solved to reconstruct the optical parameters. First the initial estimations for distributions of the optical parameters for matrix and inclusion are given. Theoretically any numbers could be selected as the initial estimations. But the initial estimations that far away from real value could increase the iteration time and may not convergent if high noise exist. Based some experimental data (i.e. Hillman, 2002) we could select initial estimations close to real value. Then light intensity on surface  $\{\phi\}$  could be calculated by Equation (6.11). The objective function (6.12) is formed by comparing measured light intensity  $\{\phi^m\}$  and calculated  $\{\phi\}$ . If the objective function is smaller than preset criteria, it means that

estimation for the optical parameters are close enough to real ones, the inverse problem stop and the estimations are output as reconstructed parameters. If the objective function is larger than preset criteria, estimated optical parameter should be updated. The adjoint field  $w$  is calculated by Equation (6.22) and gradient is obtained by Equation (6.25). Using the updated optical parameters, new iteration is repeated until the objective function is less than the preset criteria.

Our simulations always yield the same optical parameters (within the numerical processing errors), regardless of the initial estimate. The real and reconstructed optical parameters are listed in Table 6-1. It is demonstrated that parameters for the matrix are reconstructed more accurately. Reconstructed value of  $\mu_a$  for matrix is the same with real one. The error of  $\mu'_s$  for matrix is less than 1%. Comparing with matrix, the reconstruction for the inclusion has a relative coarse accuracy. The real value of  $\mu_a$  is 0.0264, while the reconstructed value is 0.024 with a 9% error. The real value of  $\mu'_s$  for inclusion is 0.8582, the same with one for matrix, while the reconstructed value is 0.72, with a 16% error.

Table 6-1 Real and reconstructed optical parameters. Stable reconstruction are generated, regardless of the initial estimation

	Matrix		Inclusion	
	$\mu_a$	$\mu'_s$	$\mu_a$	$\mu'_s$
Real values	0.0132	0.8582	0.0264	0.8582
Reconstruction	0.0132	0.8580	0.0240	0.7200

The convergent curves of DOT reconstruction for optical parameters  $\{\mu_a, \mu'_s\}$  of the matrix and inclusion are plotted in Figure 6-3. X-axial is iteration steps, Y-axial is reconstruction normalized with the exact values correspondingly. It is demonstrates that values for the  $\mu_a$  and  $\mu'_s$  of the matrix approach the measure value rapidly. After approximate 30 iterations, the relative errors are within the range of 5%. Then they exhibit some minor adjustment. In contrast, coefficients of inclusion converge slower. They begin to approach the real values after 45 iterations and reach the real values after 55 steps, with a maximum error of 16%.

## 6.5 Discussion

### 6.5.1 Regularization

In Table 6-1, it is obvious that optical parameters for the matrix are reconstructed more accurately. The error for reconstructed parameters for the matrix is less than 1%. While  $\mu'_s$  for inclusion is reconstructed with a 16% error. Moreover, in Figure 6-3, optical parameters for the matrix are reconstructed more quickly. After approximate 30 iterations, the relative errors are within the range of 5%. In contrast, coefficients of inclusion begin to approach the real values after 45 iterations and reach the real values after 55 steps.

The slower convergence and coarse accuracy of parameters for the inclusion are explained by their influence on the surface measurements. In general, parameters with the most significant influence on surface measurements are also those that are most accurately and easily identified. The influence of an optical parameter depends on size of the region it belongs to. For the present experiment and simulation, optical parameters of the tissue are dominant, while those of tumor are much less influential, due to the small size of the inclusion. The area ratio of the matrix to inclusion is about 16:1. A change of optical parameters for the inclusion will not cause big impact on the surface measurements. So it is difficult to identify the optical parameters for the inclusion.



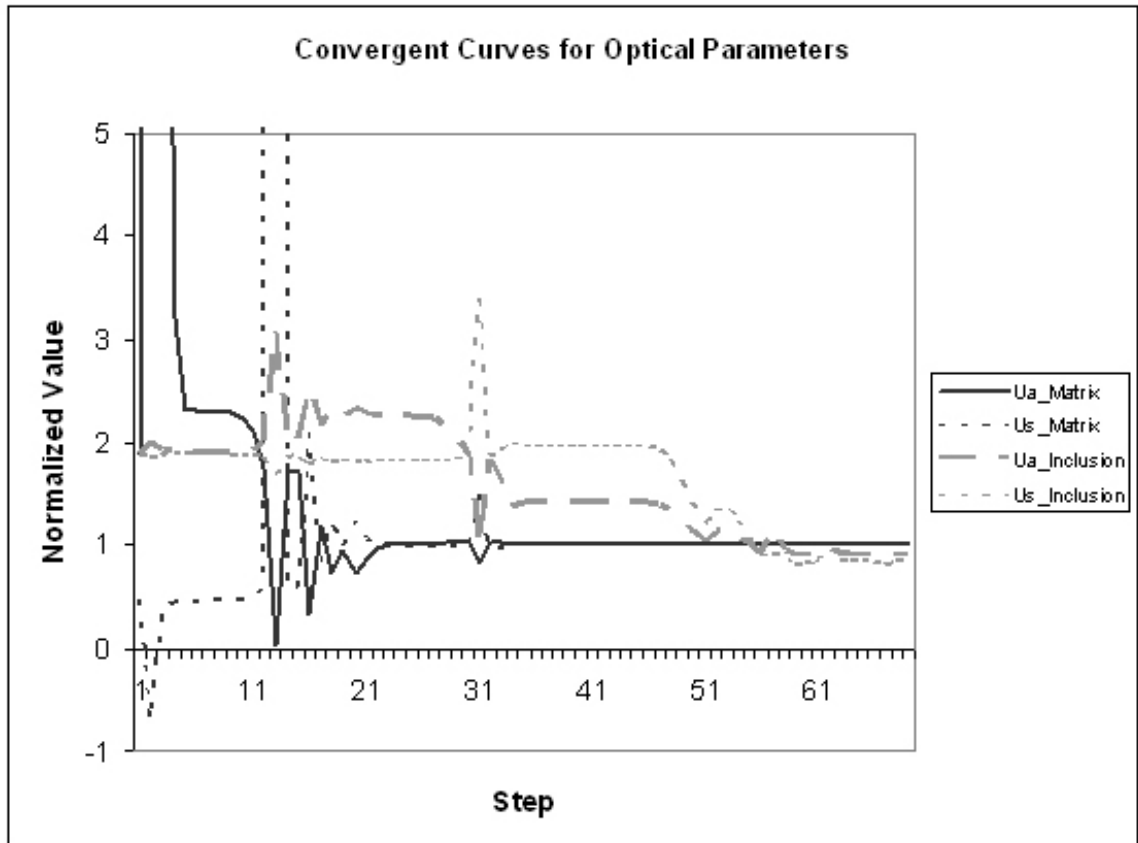


Figure 6-3 Convergent curves of DOT reconstruction for optical parameters  $\{\mu_a, \mu'_s\}$  of the matrix and inclusion.

Note: X-axial is iteration steps, Y-axial is reconstruction normalized with the exact values correspondingly.

This situation could also be explained from the point view of objective function. The DOT inverse problem is stated as the minimization of objective function related to the residual between calculated and measured light intensities on surface. The goal is to seek optical parameter distribution to obtain global minimum of the objective function. But, in practice, input data is often incomplete and corrupted by noise. A global minimum is not well defined with noise. In another words, real optical parameters may not give a global minimum of the objective function with noise. Several similar parameters around real ones may give some local minimums. For example, the reconstructed value of  $\mu'_s$  for inclusion, 0.72, may give a local minimum, while real value, 0.8582, may also give a local minimum. Because optical parameters for inclusion do not play an important role on the surface measurements, the two local minimums may be very close so that the algorithm does not push reconstructed value 0.72 to real value 0.8582.

A typical way to solve this problem is to add a penalty term which provides additional constraint on the solution space (Hielscher et al., 2001). In Section 4.4.1 we discuss how to use a penalty term to push the solution into the right area of the solution space and minimize the resulting objective. Similarly in this DOT inverse problem, a new objective function could be proposed as

$$F = G + \chi\Pi \quad (6.26)$$

where  $G$  is the original objective function Equation (6.12) which represents the difference between measured and calculated values. In addition,  $\chi$  is the regularization factor and  $\Pi$  is the penalty term which could use the prior information to push a solution to the real value.

Specific forms of penalty term have been designed for different problems (Hielscher et al., 2001; Brooksby et al., 2003). For example, an exponential form of penalty term could be applied as,

$$\Pi = \sum_{k=1}^K (1 - \exp(-(\xi_k - a_k)^2)) \quad (6.27)$$

where  $K=4$  is the total number of material parameters, and  $\xi_k$  and  $a_k$  are the reconstructed and true optical parameters, respectively. If the true optical parameters are unknown, we can estimate  $a_k$  as close as possible. This penalty term will push a reconstructed value to a real one.

### 6.5.2 Prior Knowledge

Because the inverse problem in DOT is a non-unique, ill-posed underdetermined problem, previous DOT studies frequently face the problems of unstable, time-consuming, low spatial resolution, requiring a lot of measurement data (Gibson et al., 2005). So in recent years, researchers use prior information to improve the image reconstruction. Niziachristos et al. (2000 & 2002), Schweiger et al. (2003), Brooksby et al. (2003 & 2005), Dehghani et al. (2009) used an MR image of a breast to provide the location of a tumor as a priori. Due to this approach, the spatial resolution of the optical image effectively becomes that of the MR image.

The prior information is applied in two levels: “soft priors” and “hard priors” (Brooksby, 2005). “Soft priors” are seeking to improve regularization in iteration process. In Equation (6.26)  $\chi\Pi$  is added to the objective function  $G$  as a penalty term to push reconstructed value to the real one. Soft priors could be applied to design the penalty term (Brooksby et al., 2003). For example, Li et al. (2003) use structural knowledge of the breast to define two discrete regions which they regularize differently in order to optimize NIR image contrasts.

“Hard priors” are seeking parameter reduction. Without the prior, we have to reconstruct optical parameters in each node, which makes the inverse problem in DOT is ill-posed, underdetermined since the number of unknowns is probably larger than the number of measurements. If the internal structure is as prior, the target domain could be divided into  $n$  regions and the homogeneous optical property is assumed in each region.

Due to the small number of unknowns, the inverse problem is highly over-determined and therefore computationally fast and robust to noise in the data. Pogue and Paulsen (1998) describe the use of high resolution MRI to improve simulated optical property reconstruction of a rat cranium. By accurately defining a region where heterogeneity is expected, they limited image property evolution to only those node locations.

In this study we apply hard prior, internal structure of the tissue, to divide domain to two regions: matrix and tumor. The location and size of the tumor is known. In each region optical property is assumed homogeneous. So the number of unknowns is reduced to four, that is,  $\mu_a$  and  $\mu'_s$  for matrix and tumor, respectively. The prior information could be obtained by MRI or X-ray mammography. Li et al. (2003), Zhang et al. (2005) have studied to combine optical imaging with X-ray mammography which provides anatomical information to improve spatial resolutions. In the elasto-mammography we have located the tumors by X-ray mammography projections. Similar method could applied in DOT to divide domain into normal tissue and tumor. This prior makes the ill-posed, underdetermined DOT inverse problem to be highly over-determined and therefore computationally fast and robust to noise in the data.

### 6.5.3 Adjoint Method in Complex Domain

The goal of diffuse equation tomography is to solve the inverse problem, that is, given distribution of light source and measurements on boundary, derive the tissue optical parameters distribution within the tissue.

Currently, the most used method to solve the inverse problem is nonlinear image reconstruction algorithm (Klose et al., 1999; Saquib et al., 1997; Arridge et al., 1998; Hielscher et al., 1999; Roy et al., 1999). Like in elastography, an objective function is established to compare calculated and measured light intensities. Starting with an initial guesses, the optical parameters are updated to minimize the objective functions. The challenge remains to find efficient ways of updating the initial guesses such that the

differences between calculated and measured data become smaller and the value of the objective function decreases. An increasing interest is using gradient-based iterative image reconstruction algorithm (Hielscher et al., 2000). In the gradient approach the image reconstruction problem is interpreted as a nonlinear optimization problem, in which the gradient of optical parameters is applied to minimize the objective function. However, because of the large number of measurements and the presence of noise, the commonly used gradient method is time-consuming and causes low spatial resolution. Developing a stable and efficient reconstruction algorithm is still essential in DOT (Arridge et al., 2008).

In Chapter 3-5, we have introduced the adjoint method to calculate the gradient analytically (Tardieu et al, 2000; Oberai et al., 2003; Liu et al., 2005 & 2006). In Chapter 3 we employed the adjoint method for the linear elasto-mammography, and we develop the nonlinear adjoint method to calculate gradients efficiently for proposed nonlinear elasto-mammography in Chapter 4 and 5. The results show that the adjoint method significantly enhances the numerical efficiency and stability.

Encouraged by the success of nonlinear elasto-mammography, we have expanded the adjoint method from elastography to diffuse optical tomography. The difference of developing adjoint method in between elastography and DOT is that diffuse equation is in frequency-domain, so the objective function (6.12) is in complex domain instead of real domain. Therefore the adjoint field  $\{w\}$  is divided into real part  $\{w_R\}$  and imaginary part  $\{w_I\}$ . By setting up the weak form of objective function, the adjoint field could be solved in Equation (6.22).

Favorable feature of the adjoint method is the minimum consumption for calculating the gradients. The adjoint method is to solve adjoint field  $w$  during each of iteration in Equation (6.22), instead of the whole matrix  $K$  that increases the numerical efficiency significantly. By comparing Equation (6.11) and (6.22), it can be shown that the light intensity  $\phi$  and the adjoint field  $w$  share the same matrix  $K$  and its Cholesky

factorization for the finite element computation (Press et al., 1996). Because computation for matrix  $K$  and its Cholesky factorization takes most of the time consumed in the finite element method, solving Equation (6.22) for adjoint field  $w$  and further calculating  $\delta G$  in Equation (6.24) are expected to add a small fraction of time in addition to the solution for light intensity  $\phi$ , which is anyway required in an optimization-based numerical scheme for an inverse problem.

Furthermore, it only needs to solve linear equation (6.22) regardless of the number of unknown optical parameters. In the traditional Gauss-Newton method, for each unknown optical parameters, we have to solve forward problem twice to calculate gradient. The computational cost increases proportionally with the number of unknown parameters. While in adjoint method, once the adjoint field  $w$  is solved, the gradient for optical parameter could be calculate by Equation (6.24), no matter the number of unknown parameters. More details about the comparison between adjoint method and traditional Gauss-Newton method could be found at Section 3.2.3 and 4.4.3.

#### 6.5.4 Frequent Domain and Wavelength

In this study a frequency-domain DOT system is used to provide measurements. For diffuse equation, time-domain equation (6.2) and frequency-domain equation (6.3) are equivalent. In clinical practice, frequency-domain systems are relatively inexpensive, easy to develop and to use, and can provide very temporal sampling. Time-domain system, on the other hand, tends to use photon counting detectors which are slow but highly sensitive and provide additional information about path length. Hence, frequency-domain systems are well suited to acquiring measurements quickly and at relatively high detected intensities (Gibson et al., 2005)

The choice of wavelengths is another issue in DOT. The ‘NIR window’ used for tissue optics is bounded roughly between 650 nm and 850 nm because it lets light propagate relatively deeply into the tissue before being absorbed. At lower wavelengths,

absorption by haemoglobin limits penetration in tissue, while at higher wavelengths, absorption dominates by water. In the experiment described in Section 6.3, four different wavelengths are employed: 665 nm, 785 nm, 800 nm and 830 nm. In order to test our algorithm, only data in 785 nm is employed to reconstruct the optical parameters in this study. Actually, in clinical practice, multi-wavelength measurements may be used to evaluate the hemoglobin concentration, oxygen saturation, fat, and water content. The choice of wavelengths should be considered to optimize image sensitivity and accuracy. Boas et al. (2004) have shown experimentally and theoretically that a pair of wavelengths at 660-760 nm and 830 nm provides superior separation between HHb and HbO than the more commonly used 780 nm and 830 nm.

Further some researches have been carried out to investigate the probability of a wider range of wavelength in DOT. Pifferi et al., (2003) used four wavelengths (683 nm, 785 nm, 912 nm and 975 nm) to image the breast, with the wavelengths selected empirically to optimize distinction between oxy- and deoxyhemoglobin, water and lipids.

## 6.6 Conclusions

We developed a new finite element algorithm based on adjoint method to solve the inverse problem of the frequency-domain DOT diffusion equation. The proposed adjoint method provides a new means to compute the gradients of objective function analytically. Significant computational saving is realized by utilizing the solution of adjoint equation. By comparing measurements derived from phantom experiments to numerical simulations, it is found that our algorithm is stable and robust for reconstructing the optical parameters. These results are sufficiently encouraging to warrant further development and future clinical evaluation of this adjoint method for DOT reconstruction.

## CHAPTER 7 CONCLUSIONS AND RECOMMENDATIONS

### 7.1 Conclusions

Breast cancer is one of major threats to public health in the world. Currently, X-ray mammography is the primary method for early detection and characterization of breast tumors. While it is more effective in detecting tumors as age increases and the breast becomes fatty, mammography fails to detect small cancers in dense breasts. Moreover, mammography is not quite specific in terms of tumor benignity and malignancy.

It has been recognized that mechanical and optical properties of tissues can be the indicators to identify and characterize breast tumors. To overcome the difficulties associated with mammography, the objective of this thesis is to develop new mechanical and optical modalities for qualification of the elastic and optical properties of normal and cancerous breast tissues.

#### 7.1.1 Elasto-mammography

We have developed the nonlinear elasto-mammography that utilizes the novel nonlinearly elastic breast model combined with mammography visualizations to imaging tissue elastic modulus for diagnosis of breast cancers, as tumors are stiffer than the surrounding breast tissues and malignant tumors are much stiffer than benign ones. The nonlinear elasto-mammography can quantitatively detect breast tumors in their early stage and, comparing with ultrasound elastography and magnetic resonance elastography, elasto-mammography can provide high resolution with low cost.

There are three steps to develop nonlinear elasto-mammography. First, we have developed a linear elasto-mammography method which generates the elastograms of breast tissue by combining the conventional low-dose X-ray mammography with elastography framework. The displacement information is extracted from mammography



projections before and after breast compression. Incorporating the displacement measurement, an optimization-based elastography reconstruction algorithm is specifically developed to estimate the elastic modulus of heterogeneous breast tissue. An initial guesses of distribution of elastic modulus is given and displacements are calculated in forward problem. The calculated and measured displacements are used to form objective function. Gradients of the objective function are obtained by the adjoint method and elastic parameters are updated. The iteration is repeated until a satisfied objective function is obtained. We have conducted numerical simulation with breast phantoms and investigate the effects of noise, geometry mismatch and contract ratio. It is demonstrated that the displacement measurements obtained from mammography projections is sufficient to identify the material parameters of breast tissues and tumors, and the method is stable and robust.

The second step is to develop the nonlinear elastography which extend linear material and deformation model to nonlinear cases. Most current elastography reconstruction frameworks are based on the assumption of linear elasticity theory. It is shown, however, that the deformation of most biological soft tissue is not linear elastic. Consideration of nonlinear model is essential for elastography in clinical application.

In this thesis, we have developed a new elastography model for nonlinear breast tissue and, for the first time, a nonlinear adjoint gradient method is introduced. We have introduced finite-strain deformation equation and derived the objective function by comparing calculated force and measurements. The elastic parameters are estimated by optimally minimizing the objective function. A nonlinear adjoint method is derived to calculate the gradient of the objective function. The nonlinear adjoint gradient method significantly improves the numerical efficiency and enhances the stability of nonlinear elastography reconstructions. Simulations are conducted on a three-dimensional heterogeneous breast phantom extracting from real imaging including fatty tissue, glandular tissue and tumors. We apply an exponential hyperelastic model to simulate the

deformation of breast tissue. Four loadings are applied on the breast phantom to provide more deformation information. The results demonstrate that the method is efficient and stable to detect tumors in nonlinear biological tissue by reconstruction of complex breast tissue properties. We have investigated the effect of noise and the regularization method is applied to improve the accuracy of reconstruction for tumors. We also discussed the importance of designing feasible loadings for success in clinical application of nonlinear elastography.

Encouraged by the accomplishment of linear elasto-mammography and nonlinear elastography, a nonlinear elasto-mammography method is developed to reconstruct nonlinear breast tissue properties. We utilize the novel nonlinear elastic breast model combined with mammography visualizations. As in linear elasto-mammography, the displacement information is extracted from mammography projections before and after breast compression. The elastic parameters are estimated by optimally minimizing the difference between the calculated displacements and experimental measures. The nonlinear adjoint method, developed in nonlinear elastography, is applied to calculate the gradient of the objective function. It is shown that the nonlinear elasto-mammography is stable and robust for characterization of the elastic modulus of breast tissues and tumors from the projective displacement measurement. These findings are sufficiently encouraging to warrant both further development and clinical evaluation of our proposed elasto-mammography.

### 7.1.2 Diffusion Optical Tomography

Besides elastic properties differences between normal tissues and tumors, it is known that optical properties of tissue also change related with physiological change. Diffuse Optical Tomography (DOT) emerged as a tool to identify and characterize breast tumors by imaging optical properties.

Since the inverse problem is non-unique, ill-posed underdetermined, the major challenge in DOT is to develop efficient and stable algorithm to solve the inverse problem. As we have successfully developed nonlinear adjoint method to provide gradient of the objective function in elasto-mammography, we have expanded this method to diffuse optical tomography. We have developed a finite-element-based algorithm to solve the inverse problem of frequent-domain diffusion equation. The internal structures, that is, locations and sizes of tumors, are known as a prior. We have established the objective function by comparing calculated and measured light intensity on surface. The nonlinear adjoint method is expanded to complex domains to provide gradients of the objective function. A 2-D numerical simulation is carried out and compared with phantom experiments. The results show that our adjoint-based algorithm is efficient and robust for reconstructing the optical properties.

## 7.2 Recommendations for Future Work

### 7.2.1 Multi-modalities

Because the inverse problem in diffuse optical tomography is a non-unique, ill-posed underdetermined problem, previous diffuse optical tomography studies frequently face the problems of unstable, time-consuming, low spatial resolution, requiring a lot of measurement data. So in recent years, researches have been carried to apply multi-modalities, such as combing DOT and MRI. MR image of a breast can provide the location of a tumor as a priori. Due to this approach, the spatial resolution of the optical image effectively becomes that of the MR image.

In elasto-mammography we have combined elastography and traditional X-ray to reconstruct elastic properties of breast tissues. It is natural to develop new imaging modalities by combing DOT and X-ray mammography. The internal structure of breast structure can be obtained as a prior by mammography projections. The advantage of the

multi-modalities is that the numbers of unknown parameters will be significantly decreased and imaging resolution could be improved.

Moreover, in this study we have applied a 2-D numerical model to verify our reconstruction algorithm. We may further develop a 3-D heterogeneous model to test the algorithm for clinical application.

Meanwhile new imaging technologies make it possible to combine MRI or ultrasound with our proposed elasto-mammography. In elasto-mammography the images are taken by X-ray for the whole breast, but actually the most interested area is the tumor. Recently a 3D ultrasound guided breast biopsy system has been developed to obtain more accurate imaging of breast lesions (Smith et al., 2001; Fenster et al., 2004; Abbate et al., 2009; Swinson et al., 2009). In this system, a 3D ultrasound image is acquired of the volume of breast tissue, then the interest area could be determined by users and the ultrasound transducer is moved to be directly over the target to provide real-time image of the target. To combine this new ultrasound technology may improve our proposed elasto-mammography modality.

### 7.2.2 Effect of Pressure

In optical tomography systems the human breast is usually compressed by flat glass plates or encircled by an array of fiber bundles. Pressure is applied to the exterior of the tissue, causing significant deformation in many cases. It is shown that pressure has significant impact on absorption and scattering coefficients on human tissue. The optical properties change as function of time after the pressure is applied on tissues. So the study about pressure-induced change in optical properties may provide functional information about tissue composition and elastic response that may be exploited as sensitive measures of physiology. Since we have developed new elasto-mammography modality and DOT algorithm, in the future, we may combine the elastic and optical methods to develop new-generation elasto-optical imaging modality for breast cancer imaging.

## REFERENCES

- Abbate, F., Bacigalupo, L., Latronico, A., Trentin, C., Penco, S., Menna, S., Viale, G., Cassano, E., Bellomi, M., 2009, "Ultrasound-guided vacuum breast biopsy in the assessment of C3 breast lesion by ultrasound-guided fine needle aspiration cytology: results and costs in comparison with surgery", *The Breast*, **18**, 73-77
- Alam, S.K., Richards, D.W., Parker, K.J., 1994 , "Detection of intraocular pressure change in the eye using sonoelastic Doppler ultrasound", *Ultrasound Med. Biol.*, **20**, 751-758
- American Cancer Society, 2008, "Cancer facts and figures—2008", *American Cancer Society*, Atlanta GA
- American Cancer Society, 2009, "Cancer facts and figures—2009", *American Cancer Society*, Atlanta GA
- Arridge, S.R., Cope, M., and Delpy, D.T., 1992, "The theoretical basis for the determination of optical pathlengths in tissue: temporal and frequency analysis", *Phys. Med. Biol.* **37**, 1531–59
- Arridge, S.R., Schweiger, M., 1995, "Photon measurement density functions: II. Finite element method calculations", *Appl. Opt.* **34**, 8026–37
- Arridge, S.R., Hebden, J.C., 1997, "Optical imaging in medicine: II. Modelling and reconstruction", *Phys. Med. Biol.*, **42**, 841-853
- Arridge, S.R., Schweiger, M., 1998, "A gradient-based optimization scheme for optical tomography", *Optics Express*, **2**(6), 213-226
- Arridge, S.R., 1999, "Optical tomography in medical imaging", *Inverse Problem*, **15**, R41-R93
- Arridge, S.R., Dehghani, H., Schweiger, M., Okada, E., 2000, "The finite element model for the propagation of light in scattering media: a direct method for domains with nonscattering regions", *Med. Phys.*, **27**, 252–64
- Arridge, S.R., Dorn, O., Kolehmainen, V., Schweiger, M., Zacharopoulos, A., 2008, "Parameter and structure reconstruction in optical tomography", *Journal of Physics: Conference Series*, **135**, 012001
- Barbone, P.E., Bamber, J.C., 2002, "Quantitative elasticity imaging: what can be cannot be inferred from strain images", *Physics in Medicine and Biology*, **47**(12), 2147-2164
- Barbone, P.E., Gokhale, N.H., 2004, "Elastic modulus imaging: on the uniqueness and nonuniqueness of the elastography inverse problem in two dimensions", *Inverse Problems*, **20**(1), 283-296
- Barr, R., 2006, "Clinical applications of a real elastography technique in breast imaging", *Proc. 5<sup>th</sup> Int. Conf. Ultrasonic Measurement and Imaging of Tissue Elasticity*, P112
- Belytschko, T., Liu, W.K., Moran, B., 2000, "Nonlinear finite elements for continua and structures", John Wiley & Sons, New York, NY, USA

- Bercoff, J., Chaffai, S., Tanter, M., Sandrin, L., Catheline, S., Fink, M., Gennisson, L.J., Meunier, M., 2003, "In vivo breast tumor detection using transient elastography", *Ultrasound in Medicine & Biology*, **29** (10), 1387-1396
- Bhatti, M.A., 2005, "Fundamental Finite Element Analysis and Applications: with Mathematica and Matlab Computations", John Wiley & Sons, Inc
- Bishop, J., Leitch, M., Poole, G., Plewes, D., 1998, "Magnetic resonance imaging of shear wave propagation in excised tissue", *J. Magn. Reson. Imaging*, **8**, 1257-65
- Bishop, J., Plewes, D., 1998, "An alternate method for calculating elastic properties of breast tissue", *Proc. ISMRM 6<sup>th</sup> Meeting (Sydney)*, 2102
- Boas, D.A., O'Leary, M.A., Chance, B., Yodh, A.G., 1994, "Scattering of diffuse photon density waves by spherical inhomogeneities within turbid media: analytic solution and applications", *Proc. Natl Acad. Sci. USA*, **91**, 4887-91
- Boas, D.A., 1996, "Diffuse photon probes of structural and dynamical properties of turbid media: theory and biomedical applications", Ph.D. thesis, University of Pennsylvania, Department of Physics & Astronomy, Pennsylvania.
- Boas, D.A., Brooks, D.H., Miller, E.L., DiMarzio, C.A., Gaudette, R.J., Guan, Zhang, 2001, "Imaging the body with diffuse optical tomography", *IEEE Signal Processing Magazine*, **18**(6), 57-75
- Boas, D.A., Culver, J.P., Stott, J.J., Dunn, A.K., 2002, "Three dimensional Monte Carlo code for photon migration through complex heterogeneous media including the adult human head", *Opt. Express*, **10**, 159-69
- Boas D.A., Dale A.M., Franceschini M.A., 2004, "Diffuse optical imaging of brain activation: approaches to optimizing image sensitivity, resolution, and accuracy", *NeuroImage*, **23**, 275-288
- Bone, B., Pentek, Z., Perbeck, L., Veress, B., 1997, "Diagnostic accuracy of mammography and contrast-enhanced MR imaging in 238 histologically verified breast lesions", *Acta Radiologica*, **38**, 489-496
- Boverman G., Fang Q., Carp S.A., Miller E.L., Brooks D.H., Selb J., Moore R.H., Kopans D.B., Boas D.A., 2007, "Spatio-temporal imaging of the hemoglobin in the compressed breast with diffuse optical tomography", *Phys. Med. Biol.*, **52**, 3619-3641
- Brooksby, B., Dehghani, H., Pogue, B.W., Paulsen, K.D., 2003, "Near infrared (NIR) tomography breast image reconstruction with a priori structural information from MRI: algorithm development for reconstructing heterogeneities", *IEEE J. Quantum Electron.* **9**, 199-209
- Brooksby B., 2005, "Combining near infrared tomography and magnetic resonance imaging to improve breast tissue chromophore and scattering assessment", Ph.D. Thesis, Dartmouth College, Hanover, New Hampshire
- Brooksby, B., Jiang, S., Pogue, B.W., Paulsen, K.D., Weaver, J., Kogel, C., Poplack, S.P., 2005, "Combining near-infrared tomography and magnetic resonance imaging to study *in vivo* breast tissue: implementation of a Laplacian-type regularization to incorporate magnetic resonance structure", *Journal of Biomedical Optics*, **10**(5), 051504

Burhardt, J.H., Shsyhe, J.H., 1999, "Core-needle and surgical breast biopsy: comparison of three methods of assessing cost", *Radiology*, **22**, 181-188

Chan, E.R., Sorg, B., Protsenko, D., O'Neil, M., Motamedi, M., Welch, A.J., 1996, "Effects of compression on soft tissue optical properties", *IEEE Journal of Selected Topics in Quantum Electronics*, **2**(4), 943-950

Chandrasekhar, R., "Radiation Transfer", *Clarendon*, Oxford, 1950

Chang, J., Graber, H.L., Barbour, R.L., 1995, "Image reconstruction of dense scattering media from CW sources using constrained CGD and a matrix rescaling technique", *Proc. SPIE*, **2389**, 682-91

Carp, S.A., Kauffman, T., Fang, Q., Rafferty, E., Moore, R., Kopans, D., Boas, D., 2006, "Compression-induced changes in the physiological state of the breast as observed through frequency domain photon migration measurements", *Journal of Biomedical Optics*, **11**(6), 064016

Carp, S.A., Selb, J., Fang, Q., Moore, R., Kopans, D.B., Rafferty, E., Boas, D.A., 2008, "Dynamic functional and mechanical response of breast tissue to compression", *Optics Express*, **16**(20), 16064-160678

Cheng, X., Xu, X., 2003, "Study of the pressure effect in near infrared spectroscopy", *Proc. SPIE*, **4955**, 397-406

Chernomordik, V., Hattery, D.W., Gandjbakhche, A.H., Pifferi, A., Taroni, P., Torricelli, A., Valentini, G., Cubeddu, R., 2000, "Quantification by random walk of the optical parameters of nonlocalized abnormalities embedded within tissuelike phantoms", *Opt. Lett.*, **25**, 951-3

Chernomordik, V., Hattery, D.W., Gannot, I., Zaccanti, G., and Gandjbakhche, A.H., 2002a, "Analytical calculation of the mean time spent by photons inside an absorptive inclusion embedded in a highly scattering medium", *J. Biomed. Opt.*, **7**, 486-92

Chernomordik, V., Hattery, D.W., Grosenick, D., Wabnitz, H., Rinneberg, H., Moesta, K.T., Schlag, P.M., and Gandjbakhche, A.H., 2002b, "Quantification of optical properties of a breast tumor using random walk theory", *J. Biomed. Opt.*, **7**, 80-7

Dehghani, H., Pogue, B.W., Poplack, S.P., Paulsen, K.D., 2003, "Multiwavelength three-dimensional near-infrared tomography of the breast: initial simulation, phantom and clinical results", *Appl. Opt.*, **42**, 135-145

Dehghani, H., Doyley, M.M., Pogue, B.W., Jiang, S., Geng, J., Paulsen, K.D., 2004, "Breast deformation modeling for image reconstruction in near infrared optical tomography", *Phys. Med. Biol.*, **49**, 1131-1145

Dehghani H, Srinivasan S, Pogue BW, Gibson A., 2009, "Numerical modelling and image reconstruction in diffuse optical tomography", *Philos Transact A Math Phys Eng Sci.*, **367**(1900), 3073-93

Dierkes, T., Grosenick, D., Moesta, K.T., Moller, M., Schlag, P.M., Rinneberg, H., Arridge, S., 2005, "Reconstruction of optical properties of phantom and breast lesion in vivo from paraxial scanning data", *Phys. Med. Biol.*, **50**, 2519-2542

Doyley, M.M., Meaney, P.M., Bamber, J.C., 2000, "Evaluation of an iterative reconstruction method for quantitative elastography", *Phys. Med. Biol.*, **45**, 1521-1540

Doyley, M.M., Bamber, J.C., Fuechsel, F., Bush, N.L., 2001, "A freehand elastographic imaging for clinical breast imaging: system development and performance evaluation", *Ultrasound Med. Biol.*, **27**, 1347-1357

Erkama, R.Q., Skovoroda, A.R., Emelianov, S.Y., O'Donnell, M., 2004, "Measuring the non-linear elastic properties of tissue like phantoms", *IEEE Trans. Ultrason. Ferroelectr. Freq. Control*, **51**, 410-419

Eshelby, J.D., 1957, "The determination of the elastic field of an ellipsoidal inclusion, and related problems", *Proceedings of the Royal Society of London, Series A*, **241** (1226), 375-396

Fang, Q., Carp, S.A., Selb, J., Boverman, G., Zhang, Q., Kopans, D.B., Moore, R.H., Miller, E.L., Brooks, D.H., Boas, D.A., 2009, "Combined optical imaging and mammography of the healthy breast: optical contrast derived from breast structure and compression", *IEEE Transactions on Medical Imaging*, **28**(1), 30-42

Fatemi, M., Greenleaf, J.F., 1998, "Ultrasound stimulated vibro-acoustic spectroscopy", *Science*, **280**, 82-85

Fatemi, M., Wold, L.E., Alizad, A., Greenleaf, J.F., 2002, "Vibro-acoustic tissue mammography", *IEEE Trans. Med. Imaging*, **21**, 1-8

Feng, S.C., Zeng, F., Chance, B., 1995, "Photon migration in the presence of a single defect: a perturbation analysis", *Appl. Opt.* **34** (19), 3826-3837

Fenster, A., Surry, K.J.M., Mills, G.R., Downey, D.B., 2004, "3D ultrasound guided breast biopsy system", *Ultrasound*, **42**, 769-774

Firbank M., Oda M., Delpy D.T., 1995, "An improved design for a stable and reproducible phantom material use in near infrared spectroscopy and imaging", *Phys. Med., Biol.*, **40**, 955-961

Fletcher S.W., Elmore J.G., 2003, "Mammographic screening for breast cancer", *New Engl. J. Med.*, **348**, 1672-1680

Fung, Y.C., 1993, "Biomechanics-mechanical properties of living tissues", Springer

Gao, L., Parker, K.L., Lerner, R.M., Levinson, S.F., 1996, "Imaging of the elastic properties of tissue-a review", *Ultrasound in Med. & Biol.*, **22**(8), 959-977

Gao, L., Parker, K.J., Alam, S.K., Rubens, D., Lerner, R.M., 1997, "Theory and application of sonoelastictiy imaging", *Int. J. Imaging Syst. Tech.*, **8**, 104-109

Garra, B.S., Cespedes, E.E., Ophir, J., Spratt, S.R., Zurbier, R.A., Magnant, C.M., 1997, "Elastography of breast lesions: initial clinical results", *Radiology*, **202**, 79-86

Gaudette, R.J., Brooks, D.H., DiMarzio, C.A., Miller, E.L., Gaudette, T., Boas, D.A., 2000, "A comparison study of linear reconstruction techniques for diffuse optical tomographic imaging of absorption coefficient", *Phys. Med. Biol.*, **45**, 1051-1070



Gibson, A.P., Hebden, J.C., Arridge, S.R., 2005, "Recent advances in diffuse optical imaging", *Phys. Med. Biol.* **50**, R1-R43

Giger, M.L., Huo, Z., Vyborny, C.J., 2000, "Computer-aided diagnosis in mammography", *Handbook of Medical Imaging*, Ed: M. Sonka, SPIE Press, **2**, 915-1004

Gokhale, N.H., Barbone, P.E., Oberai, A., 2008, "Solution of nonlinear elasticity imaging inverse problem: the compressible case", *Inverse Problem*, **24**, 045010

Gulsen, G., Birgul, O., Xiong, B., Nalcioglu, O., 2006, "Design and implementation of a multi-frequency diffuse optical tomography system", *Journal of Biomedical Optics*, **11**(1): 14020-14030

Gurtin, M.E., "An Introduction to Continuum Mechanics", 1981, New York, Academic

Hajnal, J.V., Hill, D.L.G., Hawkes, D.J., 2001, "Medical Image Registration", CRC PPress, Boca Raton, Fla, USA

Han, G.J., Chandran, K.B., Gotteiner, N.L., 1993, "Application of finite-element analysis with optimization to assess the in vivo non-linear myocardial material properties using echocardiographic imaging", *Medical and Biological Engineering and Computing*, **31** (5), 459-467

Hansen, P., 1998, "Rank-deficient and Discrete Ill-posed Problems", *SIAM*, Philadelphia

Hayashi, T., Kashio, Y., Okada, E., 2003, "Hybrid Monte Carlo-diffusion method for light propagation in tissue with a low-scattering region", *Appl. Opt.* **42**, 2888-96

Hielscher, A.H., Klose, A.D., Hanson, K.M., 1999, "Gradient-based iterative image reconstruction scheme for time-resolved optical tomography", *IEEE Transactions on Medical Imaging*, **18**, 262-271

Hielscher, A.H., Klose, A.D., Beuthan, J., 2000, "Evolution strategies for optical tomographic characterization of homogeneous media", *Optics Express*, **7**(13), 507-518

Hielscher, A.H., Bartel, S., 2001, "Use of penalty terms in gradient-based iterative reconstruction schemes for optical tomography", *Journal of Biomedical Optics*, **6**(2), 183-192

Hillman, E. M.C., 2002, "Experimental and theoretical investigations of near infrared tomographic imaging methods and clinical applications", Ph.D. thesis, University College London

Hiltawsky, K.M., Kruger, M., Starke, C., Heuser, L., Ermert, H., Jensen, A., 2001, "Freehand ultrasound elastography of breast lesions: clinical results", *Ultrasound Med. Biol.*, **27**, 1461-1469

Ishimaru, A., 1978, "Single scattering and transport theory (Wave propagation and scattering in random media I)", *Academic*, New York

Itoh, A., Ueno, E., Tohno, E., 2006 "Breast disease: clinical application of US elastography for diagnosis", *Radiology*, **239**, 341-350

Leff, D.R., Warren, O., Enfield, L.C., Gibson, A.P., Athanasiou, T., Pattern, D.K., Hebden, J.C., Yang, G.Z., Darzi, A., 2007, "Diffuse optical imaging of the healthy and diseased breast: a systematic review", *Breast Cancer Res. Treat.*, **108**, 9–22

Jiang, H., Paulsen, K.D., Osterberg, U.L., 1996, "Optical image reconstruction using frequency-domain data: simulations and experiments", *Optical Society of America*. **13** (2), 253-266

Jiang, H., Paulsen, K.D., Osterberg, O.L., Patterson, M.S., 1998, "Improved continuous light diffusion imaging in single- and multi-target-like phantoms", *Phys.Med. Biol.* **43**, 675-693

Jiang, S.D., Pogue, B.W., Paulsen, K.D., 2003, "In vivo near-infrared spectral detection of pressure-induced changes in breast tissue", *Optics Letters*, **28** (14), 1212-1214

Kallel, F., Bertrand, M., 1996, "Tissue elasticity reconstruction using linear perturbation method", *IEEE Trans. Med. Imaging*, **15**, 299–313

Kardestuncer, H., Norrie, D.H., 1987, *Finite Element Handbook*, New York: McGraw-Hill Publ

Kauer, M., 2004, "Inverse finite element characterization of soft tissue with aspiration experiments", Ph.D. dissertation, Swiss Federal Institute of Technology, Switzerland

Khaled, W.A.M., 2007, "Displacement estimation analyses for reconstructive ultrasound elastography using finite-amplitude deformations", Ph.D. dissertation, Ruhr-University Bochum, Bochum, Germany

Klibanov, M.V., Lucas, T.R., Frank, R.M., 1997, "A fast and accurate imaging algorithm in optical diffusion tomography", *Inverse Problem*, **13**, 1341-1361

Klose, A.D., Hielscher, A.H., 1999, "Iterative reconstruction scheme for optical tomography based on the equation of radiative transfer", *Medical Physics*, **26**(8), 1698-1707

Kolehmainen, V., Arridge, S.R., Vauhkonen, B., Kaipio, J.P., 2000, "Simultaneous reconstruction of internal tissue region boundaries and coefficients in optical diffusion tomography", *Phys. Med. Biol.* **45**, 3267-3283

Knogagou, E.E., et al., 2000, "Shear strain estimation and lesion mobility assessment in elastography", *Ultrasonic*, **38**, 400-404

Kolipaka, A., McGee, K.P., Manduca, A., Romano, A.J., Glaser, K.J., Araoz, P.A., Ehman, R.L., 2009, "Magnetic resonance elastography: Inversions in bounded media", *Magn. Reson. Med.*, **62**, 000

Kornguth, P.J., Bentley, R.C., 2001, "Mammography-pathologic correlation: Part I. Benign breast lesions", *Journal of women's imaging*, **3**(1), 29-37

Kopans, D.B., 1998, "Breast Imaging," 2<sup>nd</sup> Edition, *Lippincott – Raven Publishers*

Krouskop, T.A., Wheeler, T.M., Kallel, F., Garra, B.S., Hall, T., 1998, "The elastic moduli of breast and prostate tissues under compression", *Ultrasonic Imaging*, **20**, 151-159

- Kwon, O.I., Park, C., Nam, H.S., Woo, E.J., Seo, J.K., Glaser, K.J., Manduca, A., Ehman, R.L., 2009, "Shear modulus decomposition algorithm in magnetic resonance elastography", *IEEE Trans Med Imaging*, **28**(10), 1526-33
- Li, A., Miller, E.L., Kilmer, M.E., Brukilacchio, T.J., Chaves, T., Stott, J., Zhang, Q., Wu, T., Chorlton, M., Moore, R.H., Kopans, D.B., Boas, D.A., 2003, "Tomographic optical breast imaging guided by three-dimensional mammography" *Appl. Opt.* **42**, 5181–90
- Lindop, J.E., Treece, G.M., Gee, A.H., Prage, R.W., 2006, "3D elastography using freehand ultrasound", *Ultrasound Med. Biol.*, **37**, 529-545
- Liu, D.C., and Nocedal, J., 1989, "On the limited memory BFGS method for large scale optimization", *Mathematical Programming*, **45** (1-3), 503-528
- Liu, Y., Sun, L.Z., Wang, G., 2005, "Tomography-based 3-D anisotropic elastography using boundary measurements", *IEEE Transaction on Medical Imaging*, **24** (10), 1323-1333
- Liu, Y., Wang, G., Sun, L.Z., 2006, "Anisotropic elastography for local passive properties and active contractility of myocardium from dynamic heart imaging sequence", *International Journal of Biomedical Imaging*, Article ID 45957, 15 pages
- McKnight, A. L., Ehman, R.L., 2002, "MR elastography of breast cancer: preliminary results", *Amer. J. Roentgenology (AJR)*, **178**, 1411-1417
- Manduca, A., Muthupillai, R., Rossman, P., Greenlead, J., Ehman, R., 1996, "Image processing for Magnetic resonance elastography", *Proc. SPIE*, **2710**, 616–23
- Manduca, A., Oliphant, T.E., Dresner, M.A., Mahowald, J.L., Kruse, S.A., Amromin, E., Felmlee, J.P., Greenleaf, J.F., Ehman, R.L., 2001, "Magnetic resonance elastography: Non-invasive mapping of tissue elasticity", *Medical Image Analysis*, **5**, 237-254
- McBride, T.O., 2001, "Spectroscopic reconstructed near infrared tomographic imaging for breast cancer diagnosis", Ph.D. thesis, Dartmouth College.
- Muller, S., 1999, "Full-field digital mammography designed as complete system", *European Journal of Radiology*, **3**(1), 25-34
- Muthupillai, R., Lomas, D., Rossman, P., Greenleaf, J., Manduca, A., Ehman, R., 1995, "Magnetic resonance elastography by direct visualization of propagating acoustic strain waves", *Science*, **269**, 1854–7
- Nass, S.J., Henderson, I.C., Lashof, J.C., 2001, "Mammography and Beyond: Developing Technologies for the Early Detection of Breast Cancer", *National Academy Press*
- Ntziachristos, V., Yodh, A.G., Schnall, M., Chance, B., 2000, "Concurrent MRI and diffuse optical tomography of breast after indocyanine green enhancement", *Proc. Natl Acad. Sci. USA*, **97**, 2767–72
- Ntziachristos, V., Yodh, A.G., Schnall, M., Chance, B., 2002, "MRI-guided diffuse optical spectroscopy of malignant and benign breast lesions", *Neoplasia*, **4**, 347–54

NIH-NCI, 2004, <http://www3.cancer.gov/admin/fmb/2001sigitems/breast.html>, “Breast cancer”, National Institutes of Health, National Cancer Institute Report

Oberai, A.A., Gokhale, N.H., Feijoo, G.R., 2003, “Solution of inverse problems in elasticity imaging using the adjoint method”, *Inverse Problems*, **19**(2), 297-313

Oberai, A.A., Gokhale, N.H., Doyley, M.M., Bamver, J.C., 2004, “Evaluation of the adjoint equation based algorithm for elasticity imaging”, *Physics in Medicine and Biology*, **49**(13), 2955-2974

Oden, J.T., 1972, “Finite elements of nonlinear continua”, McGraw-Hill Book Company

Okada, E., Delpy, D.T., 2003, “Near-infrared light propagation in an adult head model: I. Modeling of low-level scattering in the cerebrospinal fluid layer”, *Appl. Opt.* **42** 2906–14

O’Hagan, J.J., Samani, A., 2008, “Measurement of the hyperelastic properties of tissue slices with tumour inclusion”, *Phys. Med. Biol.*, **53**, 7087-7106

O’Leary, M.A., Boas, D.A., Chance, B., Yodh, A.G., 1995, “Experimental images of heterogenous turbid media by frequency-domain diffusing-photon tomography”, *Opt. Lett.*, **20**, 426–8

Ophir, J., Cespedes, I., Ponnekanti, H., Yazdi, Y., Li, X., 1991, “Elastography: A quantitative method for imaging the elasticity of biological tissues”, *Ultrasonic Imaging*, **13**, 111-134

Ophir, J., Alam, S.K., Garra, B., Kallel, F., Konogagou, E., Krouskop, I., Varghese, I., 1999, “Elastography: Ultrasonic estimation and imaging of the elastic properties of tissues”, *Proc. Instn. Mech. Engr. Part H*, **213**, 203-233

Ophir, J., Alam, S.K., Garra, B.S., Kallel, F., Konofagou, E., Krouskop, T., Merritt, C.R.B., Righetti, R., Souchon, R., Srinivasan, S., Varghese, T., 2002, “Elastography: imaging the elastic properties of soft tissues with ultrasoun”, *J. Med Ultrasonics*, **29**, 155-171

Page, D., Koschan, A., Voisin, S., Ali, N., Abidi, M., 2005, “3D CAD model generation of mechanical parts using coded-pattern projection and laser triangulation systems,” *Assembly Automation*, **25**, 230–238

Pathmanathan, P., Gavaghan, D., Whiteley, J., Brady, M., Nash, M., Nielsen, P., Rajagopal, V., 2004, “Predicting tumour location by simulating large deformations of the breast using a 3D finite element model and nonlinear elasticity,” in *Medical Image Computing and Computer-Assisted Intervention*, C. Barillot, D. R. Haynor, and P. Hellier, Eds., vol. 3217 of *Lecture Notes in Computer Science*, pp. 217–224, Springer, Berlin, Germany

Pathmanathan, P., 2007, “Predicting tumour location by simulating the deformation of the breast using nonlinear elasticity and finite element method”, Ph.D. dissertation, University of Oxford

Pifferi, A., Taroni, P., Torricelli, A., Messina, F., Cubeddu, R., 2003, “Four-eavelength time-resolved optical mammography in the 680-980 nm range”, *Opt. Lett.*, **28**, 1138-1140

- Plewes, D.B., Bishop, J., Samani, A., Sciarrenta, J., 2000, "Visualization and quantification of breast cancer biomechanical properties with magnetic resonance elastography", *Phys. Med. Biol.*, **45**, 1591-1610
- Pogus, B.W., Paulsen, K.D., 1998, "High-resolution near-infrared tomographic imaging simulations of the rat cranium by use of a priori magnetic resonance imaging structural information", *Optics Letters*, **23**, 1716
- Ponnekanti, H., Ophir, J., Huang, Y., Cespedes, I., 1995, "Fundamental mechanical limitation on the visualization of elasticity contrast in elastography", *Ultrasound Med. Biol.*, **21**, 533-43
- Press, W.H., Teukolsky, S.A., Vetterling, W.T., Flannery, B.P., 1996, "Numerical Recipes in Fortran 77: The Art of Scientific Computing", (2<sup>nd</sup> Edition), New York, Cambridge University Press
- Regner, D.M., Hesley, G.K., Hangiandreou, N.J., Morton, M.J., Nordland, M.R., Meixner, D.D., Hall, T.J., Farrell, M.A., Mandrekar, J.N., Harmsen, W.S., Charboneau, J.W., 2006, "Breast lesions: evaluation with US strain imaging--clinical experience of multiple observers", *Radiology*, **238**(2), 425-437
- Richards, M.S., Barbone, P.E., Oberai, A.A., 2009, "Quantitative three-dimensional elasticity imaging from quasi-static deformation: a phantom study", *Physics in Medicine and Biology*, **54**, 757-779
- Righetti, R., Ophir, J., Ktonas, P., 2002, "Axial resolution in elastography", *Ultrasound Med. Biol.*, **28**, 101-113
- Roy, R., Sevick-Muraca, E.M., 1999, "Truncated Newton's optimization scheme for absorption and fluorescence optical tomography: Part I Theory and formulation", *Opt. Express*, **4**(10), 353-371
- Samani, A., Bishop, J., Plewes, D.B., 2001, "A constrained modulus reconstruction technique for breast cancer assessment", *IEEE Transaction on Medical Imaging*, **20**(9), 877-885
- Samani, A., Plewes, D., 2004, "A method to measure the hyperelastic parameters of ex vivo breast tissue samples", *Physics in Medicine and Biology*, **49**(18), 4395-4405
- Samani, A., Plewes, D., 2007, "An inverse problem solution for measuring the elastic modulus of intact ex vivo breast tissue tumours", *Phys. Med. Biol.*, **52**, 1247-1260
- Saquib, S.S., Hanson, K.M., Cunningham, G.S., 1997, "Model-based image reconstruction from time-resolved diffusion data", *Medical Imaging: Image Processing*, Proc. of the SPIE, **3034**, 369-380
- Sarvazyan, A.P., Skovoroda, A.R., Emelianov, S.Y., *et al.*, 1995, "Biophysical based of elasticity imaging," *Acoustical Imaging*, **21**, 223-240
- Schweiger, M., Arridge, S.R., Delpy, D.T., 1993, "Application of the finite element method for the forward and inverse problem in optical tomography", *Journal of Mathematical Imaging and Vision*, **3**(3), 263-283

Schweiger, M., Arridge, S.R., Firbank, M., Delpy, D.T., 1995, "The finite element method for the propagation of light in scattering media: boundary and source conditions", *Med. Phys.* **22** (11), 1779-1792

Schweiger, M., Gibson, A., Arridge, A.R., 2003, "Computational aspects of diffuse optical tomography", *Computing in Science & Engineering*, **5**(6), 33-41

Schweiger, M., Arridge S.R., Nissila I., 2005, "Gauss-Newton method for image reconstruction in diffuse optical tomography", *Phys. Med. Biol.*, **50**, 2365-2386

Selb, J., Dale, A.M., Boas, D.A., 2007, "Linear 3D reconstruction of time-domain diffuse optical imaging differential data: improved depth localization and lateral resolution", *Optics Express*, **15** (25), 16400-16412

Shanggnuan, H., Prahl, S., Jacques, S., Casperson, L., Gregory, K., 1998, "Pressure effects on soft tissues monitored by changes in tissue optical properties", *Proc. SPIE*, **3254**, 366-371

Sinkus, R., Lorenzen, J., Schrader, D., Lorenzen, M., Dargatz, M., Holz, D., 1999, "MR-Elastography applied to in vivo MR-mammography", *Proc. ISMRM, 7th Meeting Philadelphia, PA, (Berkeley, CA: ISMRM)*, 259

Sinkus, R., Lorenzen, J., Schrader, D., Lorenze, M., Dargatz, M., Holz, D., 2000, "High-resolution tensor MR elastography for breast tumor detection", *Phys. Med. Biol.*, **45**, 1649-1664

Skovoroda, A.R., Emelianov, S., Lubinski, M., Sarvazyan, A.P., O'Donnell, M., 1994, "Theoretical analysis and verification of ultrasound displacement and strain imaging", *IEEE Trans. Ultrason. Ferroelectr. Freq. Control*, **41**, 302-13

Skovoroda, A.R., Klishko, A.N., Guaskian D.A., Maevskii, E.I., Ermilova, V.D., Oranskaia, G.A., Sarvazian, A.P., 1995, "Quantitative analysis of the mechanical characteristics of pathologically altered soft biological tissues," *Biofizika*, **40**, 1335-1340

Skovoroda, A.R., Emelianov, S., and O'Donnell, M., 1995, "Tissue elasticity reconstruction based on ultrasonic displacement and strain images" *IEEE Trans. Ultrason. Ferroelectr. Freq. Control*, **42**, 747-65.

Skovoroda, A.R., Lubinski, M.A., Emelianov, S.Y., O'Donnell, M., 1999, "Reconstructive elasticity imaging for large deformations", *IEEE Trans. Ultrason. Ferroelectr. Freq. Control*, **46**, 523-535

Smith, W.L., Sury, K.J.M., Mills, G.R., Downey, D. B., Fenster, A., 2001, "Three-dimensional ultrasound-guided core needle breast biopsy", *Ultrasound in Med. & Biol.*, **27**(8), 1025-1034

Swinson, C., Ravichandran, D., Nayagam, M., Allen, S., 2009, "Ultrasound and fine needle aspiration cytology of the axilla in the pre-operative identification of axillary nodal involvement in breast cancer", *European Journal of Surgical Oncology*, **35**, 1152-1157

Tabár, L., and Dean, P.B., 2003, "Mammography and breast cancer: the new era", *International Journal of Gynecology & Obstetrics*, **82** (3), 319-326

- Tardieu, N., Constantinescu, A., 2000, "On the determination of elastic coefficients from indentation experiments," *Inverse Problem*, **16** (3), 577-588
- Taroni, P., Danesini, G., Torricelli, A., Pifferi, A., Cubeddu, R., 2004, "Clinical trial of time-resolved scanning optical mammography at 4 wavelengths between 683 and 975 nm", *Journal of Biomedical Optics*, **9**(3), 464-473
- Thitaikumar, A., Mobbs, L.M., Kraemer-Chant, C.M., Garra, B.S., Ophir, J., 2008 "Breast tumor classification using axial strain elastography: a feasibility study", *Phys. Med. Biol.*, **53**, 4809-4823
- Treece, G.M., Lindop, J.E., Gee, A.H., Prager, R.W., 2008, "Freehand ultrasound elastography with a 3-D probe", *Ultrasound Med. Biol.*, **34**, 463-474
- Unlu, M.B., Birgul, O., Shafiiha, R., Gulsen, G., Nalcioglu, O., 2006, "Diffuse optical tomographic reconstruction using multi-frequency data", *J Biomed Optics*, **11**(5): 054008
- Van Houten, E.W., Paulsen, K.D., Miga, M.I., Kennedy, F.E., Weaver, J.B., 1999, "An overlapping sub zone technique for MR based elastic property reconstruction", *Magn. Reson. Med.*, **42**, 779-786
- Van Houten, E.W., Miga, M.I., Weaver, J.B., Kennedy, F.E., Paulsen, K.D., 2001, "Three-dimensional subzone-based reconstruction algorithm for MR elastography", *Magn. Reson. Med.*, **45**, 827-837
- Van Houten, E.E.W., Doyley, M.M., Kennedy, F.E., Weaver, J.B., Paulsen, K.D., 2003, "Initial in vivo experience with steady-state subzone-based MR elastography of the human breast", *J.Magn. Reson. Imaging*, **17**, 72-85
- Varghese, T., Ophir, J., Krouskop, T.A., 2000, "Nonlinear stress-strain relationships in tissue and their effect on the contrast-to-noise ratio in elastograms", *Ultrasound in Med. & Biol.*, **26**(5), 839-851
- Wang, B., Povoski, S.P., Cao, X., Sun S., Xu, R.X., 2008, "Dynamic scheme for near infrared detection of pressure-induced changes in solid tumors", *Applied Optics*, **47**(16), 3053-3063)
- Wang, L., Jacques, S.L., Zhao, X., 1995, "Continuous-wave ultrasonic modulation of scattered laser light to image objects in turbid media", *Opt. Lett.*, **20**, 629-631
- Wang, Z.G., Liu, Y., Sun, L.Z., Wang, G., Fajardo, L.L., 2006, "Elasto-mammography: theory, algorithm, and phantom study", *International Journal of Biomedical Imaging*, 1-11
- Wang, Z.G., Liu, Y., Wang, G., Sun, L.Z., 2009, "Elastography method for reconstruction of nonlinear breast tissue properties", *International Journal of Biomedical Imaging*, Article ID 406854
- Weaver, J., Van Houten, E., Miga, M., Kennedy, F., Hartov, A., Poplack, S., Nagy, H., Paulsen, K., 1999, "Measurement of harmonic motion for MR elastography", *Proc. ISMRM, 7th Meeting (Philadelphia, PA)* (Berkeley, CA: ISMRM), 1617
- Weiss, G.H., Porr`a, J.M., Masoliver, J., 1998, "The continuous-time random walk description of photon migration on an isotropic medium", *Opt. Commun.*, **146**, 268-76

- Wellman, P., 1999, "Tactile imaging", Ph.D. dissertation, Harvard University, Cambridge, Mass, USA
- Wellman, P., Howe, R., Dalton, E., Kern, K.A., 1999, "Breast tissue stiffness in compression is correlated to histological diagnosis," *Harvard BioRobotics Laboratory Technical Report*
- Xu, M., Wang, L.V., 2006, "Photoacoustic imaging in biomedicine", *Rev. Sci. Instrum.*, **77**, 041101
- Taylor, R.L., 2000, "The Finite Element Method for Solid and Structural Mechanics", Elsevier
- Zhang, Q., 2005, "Co-registered tomographic X-ray and optical breast imaging: initial results", *J. Biomed. Opt.*, **10**, 024033
- Zhu, Q.L., Jiang, Y.X., Liu, J.B., Liu, H., Sun, Q., Dai Q., Chen, X., 2008, "Real-time ultrasound elastography: its potential role in assessment of breast lesions", *Ultrasound in Med. & Biol.*, **34**(8), 1232-1238
- Zulliger, M.A., Fridez, P., Hayashi, K., Stergiopoulos, N., 2004, "A strain energy function for arteries accounting for wall composition and structure", *Journal of Biomechanics*, **37**(7), 989-1000